

Entropic Segregation of Polymers under Confinement

Von der Fakultät Mathematik und Physik und dem Stuttgart
Research Centre for Simulation Technology (SRC Sim Tech) der
Universität Stuttgart zur Erlangung der Würde eines Doktors der
Naturwissenschaften (Dr. rer. nat.) genehmigte Abhandlung

Vorgelegt von

Elena Minina

aus Swerdlowsk Region, Russland

Hauptberichter: Prof. Dr. Christian Holm

Mitberichter: Prof. Dr. Udo Seifert

Mitberichter: Prof. Dr. Christos N. Likos

Tag der mündlichen Prüfung: 15.03.2016

Institut für Computerphysik der Universität Stuttgart

2016

Erklärung

Hiermit versichere ich, die vorliegende Arbeit selbstständig verfasst und keine anderen als die angegebenen Quellen und Hilfsmittel benutzt, sowie die Zitate deutlich kenntlich gemacht zu haben.

Stuttgart, den 8. Januar 2016

Elena Minina

Contents

Zusammenfassung	4
1 Introduction	8
2 State of the art	12
2.1 Experiments on confined polymers	12
2.2 Entropy and basics of statistical physics	22
2.3 Polymer theory	24
2.3.1 Conformations of ideal polymers	24
2.3.2 Conformations of self-avoiding polymers	29
2.3.3 Polymer under tension. The de Gennes blob model	32
2.3.4 Polymers under compression. Cylindrical confinement	34
2.3.5 Polymers between two parallel plates	37
2.4 Molecular dynamics simulations	39
2.4.1 Force calculation	39
2.4.2 Numerical integrator	39
2.4.3 Thermostat	40
2.4.4 Optimization	40
2.5 Coarse-grained simulation model of polymers	41
2.6 Reaction-rate theory or Kramers' theory	42
2.7 Free energy calculations	46
2.7.1 Potential of mean force	47
2.7.2 Forward Flux Sampling	48
2.7.3 Widom's insertion method	52
2.8 Entropic segregation of polymers	55
2.8.1 Polymer segregation in cylindrical confinement. Segregation speed and time scale	55
2.8.2 Ring polymers in cylindrical confinement	59
2.8.3 Spatial polymer organization in closed cylindrical confinement and segregation dynamics	63

CONTENTS

3	Segregation of linear polymers under cylindrical confinement	68
3.1	Force calculation of segregating linear polymers.	69
3.2	Induction phase	72
3.2.1	Theoretical calculation of induction time	74
3.2.2	Simulation details	77
3.2.3	Results	78
3.3	Modeling replication process	83
3.4	Conclusion	85
4	Segregation of ring polymers under cylindrical confinement	88
4.1	Segregating ring polymers	88
4.1.1	Theoretical details	88
4.1.2	Simulation details	90
4.1.3	Results	91
4.2	Induction phase of ring polymers	94
4.2.1	Theoretical details	94
4.2.2	Simulation details	96
4.2.3	Results	97
4.3	Conclusion	100
5	Compression of polymers under cylindrical confinement	102
5.1	Conventional Brute Force Simulations	102
5.2	Forward Flux Sampling Simulations	106
5.3	Free energy of polymers	107
5.4	Free energy barrier	108
5.5	Conclusion	112
6	Effective potential of linear polymers confined in a slit	114
6.1	Simulation model	114
6.2	Results	116
6.3	Conclusion	118
7	Summary and outlook	120
	Acknowledgments	125
	Bibliography	126

Zusammenfassung

Überlappende Polymere, die in einem Zylinder eingeschlossen sind, stoßen einander ab, was zu ihrer Trennung führt. Dies ist für die Trennung von Chromosomen in länglichen einzelligen Organismen, wie etwa *Escherichia coli* von Bedeutung, da sich auf diese Weise Chromosomen grundsätzlich allein durch entropische Kräfte voneinander trennen können – ohne Unterstützung durch einen aktiven Mechanismus. In dieser Doktorarbeit wurde daher die entropische Segregation von Polymeren in unendlichen langen Zylindern untersucht, wobei der Durchmesser der Zylinder kleiner als der Gyrationradius des freien Polymers ist.

Es wurden Molekulardynamik-Simulationen mit dem Softwarepaket ESPResSo durchgeführt. Die Polymere wurden dabei als Feder-Kugel-Systeme modelliert. Darüber hinaus wurde ein theoretisches Modell zur Berechnung der freien Energie der Polymer abhängig vom Grad ihrer Trennung entwickelt. Es basiert auf einer Aufteilung des Untersuchungsgebiets in Regionen, in denen sich die Monomere überlappen und solche, in denen das nicht der Fall ist. Durch eine Anwendung der renormalisierten Flory-Methode konnten gezeigt werden, dass die repulsive Kraft zwischen den Polymeren während des Segregationsprozesses nicht konstant ist. Dies steht im Gegensatz zu Vorhersagen bisheriger theoretischer Modelle für die Segregation linearer Polymere. Im Unterschied zu früheren Modellen berücksichtigt unser Zugang, dass die Polymere durch den Überlapp gestreckt werden. Dies erlaubt uns eine genauere Berechnung der freien Energie, bei der sich eine nicht konstante Kraft ergibt. Wir zeigten, dass die Kraft stets antiproportional zum Durchmesser des Zylinders ist, unabhängig davon, ob wir die Streckung der Polymere berücksichtigen, oder nicht. Die Streckung der Polymere verändert also die wichtigsten Skalierungsgesetze nicht: die Geschwindigkeit der Trennung $V \sim 1/ND$ und der Zeit bis zur vollständigen Segregation $t_{seg} \sim N^2 D^{2-1/\nu}$ zeigen weiterhin die gleiche Abhängigkeit von der Länge der Polymere N und dem Durchmesser des Zylinders D , wie auch schon im früheren, einfachen Modell.

In Simulationen haben wir beobachtet, dass ein wichtiger Aspekt der Trennung von Polymeren in unendlichen Zylindern die Induktionsphase ist. Diese findet statt, bevor sich die Polymere voneinander trennen. In dieser Phase wird die zu Anfang bestehende vollständige Symmetrie der Konfiguration der Polymere gebrochen. Erst

wenn dies geschehen ist, beginnt der eigentliche Trennungsprozess.

Ein Teil dieser Doktorarbeit ist dem Mechanismus der Symmetriebrechung und den Zeitskalen dieser sogenannten Induktionsphase gewidmet. Dieser Aspekt wurde bisher nicht untersucht. Während der Induktionsphase kann es dazu kommen, dass eines der beiden Polymere zwischen den Enden des anderen gefangen wird. Die Trennung der Polymere beginnt jedoch erst, wenn von beiden Polymeren jeweils ein Ende aus der Überlappregion herausragt. Um diese Konfiguration der Enden zu erreichen, müssen die Polymere eine freie Energiebarriere überwinden. Mittels unseres Ansatzes der Gebietsaufteilung konnten wir zeigen, dass die Höhe der Barriere linear mit der Länge der Polymere skaliert. Folglich ist das Erreichen der richtigen Konfiguration ein seltenes Ereignis. Mit Hilfe der Kramers Theorie konnten wir zeigen, dass die Induktionszeit exponentiell mit der Höhe der Energiebarriere und der Polymerlänge zusammenhängt. Dieses theoretisch hergeleitete Skalierungsverhalten der Induktionsphase konnten wir durch Computersimulationen bestätigen. Damit ist klar, dass die Induktionsphase bei langen Polymeren in einem unendlich ausgedehnten Zylinder sehr viel länger dauert als die eigentliche Trennung der Polymere, die lediglich quadratisch mit der Polymerlänge skaliert. Bei langen Polymeren dominiert also die Induktionsphase den Teilungsprozess.

Da die entropische Trennung von Polymeren für die Chromosomentrennung in Bakterien von Bedeutung ist, haben wir uns mit einem der wichtigen biologischen Detailspekte näher beschäftigt, nämlich der Replikation. Wir haben untersucht, ob die Replikation der Chromosomen die Induktionsphase beeinflussen kann.

Wir untersuchten dazu das Verhalten zweier anfangs überlappender Polymere mit einer endlichen Replikationsrate. Die Induktionsphase ist deutlich sichtbar, unabhängig von der Replikationsrate. Bei einer hohen Replikationsrate ändert sich die Verteilung der Induktionszeiten weder qualitativ noch quantitativ. Bei einer langsamen Replikation kann die Trennung schon während der Replikation beginnen, häufig sind jedoch die Enden des einen Polymers zwischen denen des anderen gefangen. Dann kommt also wieder die oben besprochene Frage der Konfiguration der Polymerenden ins Spiel. Neben der Induktionsphase lässt die Replikation auch den Segregationsprozess und ihre Zeitskalen unberührt.

Die Chromosomen in länglichen Bakterien sind Ringmoleküle. In dieser Arbeit haben wir dies berücksichtigt, und untersucht, wie die Ringstruktur die Induktionsphase und den Trennungsprozess beeinflusst. Hierfür haben wir den Flory-Ansatz für die Berechnung der freien Energie bei Ringpolymeren verallgemeinert. Dabei haben wir erneut den Ansatz der Gebietsaufteilung verwendet. Zusätzlich benutzen wir die Tatsache, dass sich Ringpolymere in einem Zylinder durch zwei lineare Polymere, die in zwei gedachten Zylindern mit reduziertem Durchmesser eingeschlossen sind, darstellen lassen. Mit Hilfe von Simulationen haben wir bewiesen, dass das theoretische Modell die freie Energie bei der Trennung von Ringen korrekt wiedergibt und auch auf die Berechnung der freien Energie bei vielen einander überlappenden Ket-

ten anwendbar ist. Die Ringtopologie erleichtert also nicht nur die Trennung. Wir konnten auch zeigen, dass sie diese im Vergleich zu linearen Polymeren der gleichen Länge stets um einen Faktor von $2^{3/2}$ beschleunigt ist. Die Induktionsphase ist bei Ringpolymeren ebenfalls kürzer als bei linearen Polymeren, was jedoch nichts an der exponentiellen Abhängigkeit von der Kettenlänge ändert. Auch dies haben wir durch Computersimulationen bestätigt. Unabhängig von der Topologie der Polymere dominiert also die Induktionsphase über die Segregationsphase.

Der Einschluss zweier Polymere in einem endlichen Zylinder kann in Abhängigkeit von der Form des Zylinders zu einer Änderung ihrer räumlichen Struktur führen. Insbesondere kann dies die Mischbarkeit der Polymere beeinflussen. Wir haben den Zusammenhang zwischen der räumlichen Organisation und der Mischbarkeit bei einem recht niedrigen Volumenanteil für die Monomere von $\phi = 0.076$ untersucht. Wir haben dabei das Aspektverhältnis des Zylinders variiert, um alle möglichen Formen zu untersuchen, von sehr lang und dünn bis hin zu scheibenförmig. Wir zeigten, dass sich die Polymere in einem langen, dünnen Zylinder so stark abstossen, dass sie sich nicht mischen lassen. Trotz der Einschränkung durch die endliche Länge des Zylinders belegt also jedes der Polymere jeweils eine Hälfte des Zylinders.

Bei einem scheibenförmigen System mischen sich die Polymere entlang der Längsrichtung. Aufgrund des ausgeschlossenen Volumens trennen sie sich jedoch in radialer Richtung. Dies passt zu dem Mischbarkeitsdiagramm, welches den Überlapp der Polymere für verschiedene Zylindergeometrien darstellt. Bei langen, dünnen Zylindern wird die Mischung der Polymere durch eine hohe freie Energiebarriere verhindert. Diese haben wir durch direkte Molekulardynamik-Simulationen mit Hilfe von ESPResSo sowie durch Forward-Flux-Sampling mit Hilfe von FRESHS für verschiedene Aspektverhältnisse bestimmt. Die Höhe der Barriere nimmt mit der Länge des Zylinders zu, so dass die höchste Barriere für die längsten und dünnsten Zylinder erreicht wird. Die Energiebarriere geht gegen null, wenn das Aspektverhältnis gegen eins geht. Unsere analytischen Berechnungen auf Basis des renormalisierten Flory-Ansatzes bestätigen die Ergebnisse aus den Simulationen.

Die Abhängigkeit der Höhe der freien Energiebarriere von der Zylindergeometrie sind für das biologische System wichtig. Je länglicher ein einzelliges Bakterium ist, desto höher ist die freie Energie, die für den Überlapp der Chromosomen aufgewendet werden muss. Das führt zu einer stärkeren Abstossung während des Teilungsprozesses. Längliche Geometrien vereinfachen also die Trennung. Dabei muss die Trennung nicht unbedingt schnell ablaufen, sollte aber effizient sein, um andere laufende Prozesse der Zellteilung nicht zu stören. Es ist denkbar, dass die Natur die Form prokaryotischer Bakterien unter diesem Aspekt optimiert hat, da diese sehr häufig anzutreffen sind.

Was zukünftige Erweiterungen der Untersuchungen betrifft, so könnten zum Beispiel endliche Zylinder mit höheren und niedrigeren Volumenanteile der Monomere betrachtet werden. Die Mischbarkeitsdiagramme könnten um freie Energien erwei-

tert werden, so dass sie nicht nur die räumliche Organisation der Polymere, sondern auch den dafür nötigen Energieaufwand zeigen.

Polymere trennen sich nicht nur in Zylindern allein auf Grund der Entropie. Auch in Schlitzporen kann man dies beobachten. Im Rahmen dieser Doktorarbeit haben wir die Untersuchung der Segregation in dieser Geometrie begonnen und uns der Frage gewidmet, wie stark sich die Polymere voneinander abstossen. Mit Hilfe der “Widom Insertion” Methode haben wir die freie Energie zweier Polymere zwischen parallelen Platten berechnet. Der Abstand der beiden Platten ist dabei deutlich kleiner als der Gyrationradius des freien Polymers. Die freie Energie wird in Abhängigkeit vom Abstand der Massenschwerpunkte der Polymere gezeigt. Für geringe Abstände findet man dabei ein Plateau. Bei grösseren Abständen fällt die freie Energie zu null hin ab. Der Nullpunkt wird bei einem Abstand von etwa drei Gyrationradien eines freien Polymers erreicht. Das Plateau rührt von der Tatsache her, dass die Anzahl der überlappenden Monomere, die das effektive Potenzial bestimmt, zu Beginn der Trennung nicht vom Abstand der Massenschwerpunkte abhängt. Solch ein Plateau wurde auch in Zylindergeometrien beobachtet. Die entsprechende Region ist dort aber viel kleiner und nur von der Grössenordnung eines Zylinderdurchmessers. Die Abhängigkeit der Länge des Plateaus von der Länge der Polymere und dem Plattenabstand bleibt eine offene Frage für zukünftigen Studien. Bisher ist auch noch nicht bekannt, wie das effektive Potenzial für den Überlapp in Schlitzporen analytisch bestimmt werden kann. Eine entsprechende Theorie wurde noch nicht gefunden. Solch eine Theorie müsste eine genaue Schätzung der Anzahl der überlappenden Blobs liefern. Das ist in Schlitzgeometrien schwierig, weil in diesem Fall die lineare Ordnung, wie sie in Zylindern angetroffen wird, nicht vorhanden ist. Grundsätzlich könnte wiederum die Flory-Theorie als Basis dienen, es muss aber eine passende Renormierung entwickelt werden.

Chapter 1

Introduction

Polymers are ubiquitous in today's world. The cup that contains your morning coffee "to go" bought in the closest bakery, plastic food wraps for keeping food fresh, and different kinds of adhesives and rubbers are some of many examples of polymeric materials, without which one can not imagine modern life. All the benefits that polymeric materials bring to mankind have become possible due to scientists who have synthesized polymers and investigated their properties at the early stage of polymer science. The most significant amongst them are: Hermann Staudinger, who in the 1920s identified a polymer as a long chain of repeated units; Giulio Natta and Karl Ziegler, who in the early 1950s discovered a process for synthesizing many plastics such as polyethylene and polypropylene; and Paul J. Flory and Pierre-Gilles de Gennes, who developed the core of polymer theory.

Since the time when these breakthroughs in polymer science were made, many other striking findings have been discovered and new polymeric materials have been synthesized. For example, polymer nanocomposites, which are composed of nano-sized particles dispersed in a polymer matrix, are currently used in a wide range of applications, from the automobile industry to high-tech electronics and solar cells. Depending on the type of nanoparticles and the polymer matrix, nanocomposites possess different properties required by a specific application. Modern medicine also relies heavily on polymeric materials: dental fillings, contact lenses, and artificial joints are also examples of polymeric materials. Another area that attracts interest from both scientists and pharmaceutical companies is drug-delivery. Here, hydrogels and polymer-based carriers play an important role, since a drug is usually suspended in a polymer matrix in order to safely reach its target.

In addition to man-made polymers, polymers also occur in nature. Examples of naturally occurring polymers are silk, wool, DNA, cellulose, and proteins. Probably the most fascinating natural polymer is DNA, which contains the genetic code and instructions for the functioning and reproduction of all kinds of living organisms. Most of the biological processes that involve DNA take place in a confined

environment. It has long been known that polymers in confined geometries behave very differently from unconfined polymers. Their static and dynamic properties play an important role in, for example, DNA translocation through nanopores and chromosome organization. Nowadays the advances in micro- and nano-fabrication technology allows one to study properties of confined polymers experimentally and make a fundamental analysis of individual DNA molecules. Moreover, nano- and micro-fluidic devices are irreplaceable in sorting DNA molecules by length, growing populations of bacteria for analyzing cell division, and manipulating bacterial chromosomes in *vitro* for studying macromechanical properties of chromosomes. In all these applications the entropic effect of polymers induced by confinement plays a crucial role.

Arguably, the most striking feature of confinement is the tendency of polymer chains to segregate for purely entropic reasons. An overlap of two polymers under confinement significantly reduces the conformational entropy, which drives the polymers towards segregation. This means that in elongated cells such as the bacteria *Escherichia coli*, two overlapping DNA molecules will move spontaneously to opposite ends of the cell even in the absence of active mechanisms. Although real bacteria are full of proteins that also participate in chromosome segregation, the purely entropic effect is an essential part of the process. However, the interplay between the active biological and passive entropic mechanisms of segregation remains unexplored.

In order to distinguish the inevitable entropic segregation from possible active mechanisms, one needs to investigate all the possible details of entropic segregation including its time scales. This requires understanding how the confined polymers interact with each other, which is a classical polymer problem in confined spaces. This thesis addresses the aforementioned problem in order to give a more detailed picture of entropic segregation of confined polymers.

Entropic segregation has only recently attracted attention because of its relevance to chromosome segregation in bacteria. First of all, entropic segregation has been investigated by computer simulations for different confining geometries such as a sphere, a two-dimensional box, and open and closed cylinders [1, 2, 3, 4, 5, 6]. There are also studies on the effects of polymer stiffness, crowding, or different polymer topologies [7, 8, 9]. All these studies show that the more confined the polymers are, the stronger the segregation forces become, causing the polymers to segregate at least partially [3, 5, 6]. The current state of the art concerning entropic segregation accompanied by the necessary theoretical background is summarized in Chapter 2.

Despite strong segregation forces, which push away the polymers confined in a cylinder, fully overlapping polymers do not necessarily segregate immediately [2, 9]. The reason for this is the induction phase, in which the initial system symmetry is broken by spontaneous fluctuations. Segregation starts if the polymers centers of mass get shifted with respect to each other. In Chapter 3 we investigate the origin

of the induction phase by modeling the segregation of linear polymers trapped in a cylinder of infinite length, which mimics a growing, idealized simple bacterium of elongated shape. We demonstrate that the main mechanism of induction is not diffusion of the entire chains as previously proposed [2], but rather the arrangement of the polymer ends. During the induction phase it can happen that one polymer gets trapped within the other's coil such that the polymers cannot segregate. Between this trapped configuration and a configuration that is required for initiation of the entropic segregation, a considerable free energy barrier has to be overcome. We estimate the height of this barrier showing that it scales exponentially with polymer length. Finally, we determine the time scale of induction, which allows us to conclude that for long polymers the induction takes much more time than the actual segregation. Another important aspect that we consider in this chapter is how much such an important biological detail as replication can influence the induction phase. Considering different rates of replication we found that replication does not bring any benefits to polymer segregation in an infinitely long cylinder, in particular, it does not help to reduce the induction phase.

Compared with linear polymers, confined rings repel each other more strongly due to larger entropic reduction. Therefore, the ring topology enhances the entropic segregation. In Chapter 4, we study the effect of the polymer topology on the segregation and induction phase. To this end, we introduce a generalization of the renormalized Flory approach [6], which we call the territorial renormalized Flory approach. Using this approach we estimate the free energy of many overlapping chains, which mimic overlapping rings, in cylindrical confinement. This allows us to find the time scales of the entropic segregation of rings in open cylindrical confinement. Comparisons of the time scales obtained for rings with linear polymers demonstrates that both segregation and induction take significantly less time for rings than for linear chains, which we confirm with computer simulations.

In cylinders of finite length, the degree of polymer segregation depends on the asymmetry of the confining cylinder. Tuning the shape of the cylinder, one can make it so that two self-avoiding polymers start mixing along the longitudinal axis of the cylinder at least partially. The interplay between the polymer miscibility and the spatial organization of polymers confined in a cylinder has recently been studied and summarized in miscibility diagrams, which shows the degree of polymer overlap depending on the shape of the confining cylinder [3, 5]. This diagram confirms that the more elongated the cylinders are, the more polymers resist mixing despite the longitudinal compression exerted by confinement. This resistance is induced by the free energy cost of polymer overlap. In Chapter 5, we study the effect of the longitudinal compression on the free energy of linear polymers confined in a cylinder of finite length at fixed volume fraction of monomers comprising the polymers. Using computer simulations and the Forward Flux Sampling method, we estimate the free energy barrier that two polymers have to overcome in order to mix at different

aspect ratios of the cylindrical axes. We demonstrate that the free energy barrier decays with an increase of the longitudinal compression that is consistent with the miscibility diagrams.

In Chapter 6 of the thesis, we change the confining geometry from a cylinder to a slit in order to understand how strongly the polymers interact with each other depending on the degree of polymer separation. To this end, we compute the effective potential of two polymers confined in a slit using the method of Widom insertion. We show that the interpolymer interactions in slits is significantly weaker compared with cylinders and that the effective potentials obtained for different polymer length and widths of the slit have more pronounced plateau-like region at the beginning of the polymer separation from the fully overlapping state. The latter may lead to a change in spatial dynamics of segregating polymers in a slit and slow down segregation.

Finally, in Chapter 7, we summarize all the results obtained within this thesis and give an outlook for further possible investigations of entropic segregation of confined polymers.

Prior Publications of the Author

Parts of this thesis have been previously published in peer-reviewed journals. The content from the following publications co-authored with A. Arnold is included in this thesis.

- Elena Minina and Axel Arnold – Induction of entropic segregation: the first step is the hardest. *Soft Matter*, **10** (31), 5836-5841, 2014.
- Elena Minina and Axel Arnold – Entropic segregation of ring polymers in cylindrical confinement. *Macromolecules*, **48** (14), 4998-5005, 2015.

Chapter 2

State of the art

This chapter is dedicated to providing the necessary background for understanding this thesis. We start with a section describing experimental findings on confined polymers and demonstrating the relevance of the entropic segregation to biological systems. The next two sections present the necessary theoretical background starting from the statistical mechanics with the main focus on the physics of polymers. Then, we introduce principles of the classical molecular dynamics simulations while drawing attention to the specific details which have to be taken into account for studying the physics of polymers under confinement. Namely, a description of the course-graining model commonly used to describe a self-avoiding polymer is presented. Thereafter, we continue with a discussion of the reaction-rate or Kramers' theory and the principles of the advance sampling techniques which have been used in this thesis for free energy barrier computations. Finally, the last section of this chapter gives an overview of recent findings in entropic segregation of polymers under confinement.

2.1 Experiments on confined polymers

Understanding of static and dynamic properties of confined polymers is not only one of the key questions in polymer physics, but also serves as the basis for the development of new techniques for investigating many biological processes. Recently developed micro- and nanofluidic devices provide a powerful tool to probe biology on length scales ranging from nano- to micrometers, which are typical of biological processes [11, 12, 13]. Many of these devices are specially designed for single DNA analysis and manipulation [11, 14, 15]. The fundamental building block of these devices is a channel of cylindrical, rectangular or slit-like shape (for example, see Fig. 2.1). A DNA confined in a sufficiently long channel whose width is less than the DNA's unconfined radius of gyration expands naturally along the channel to its equilibrium configuration without the need of any external forces, thus providing the

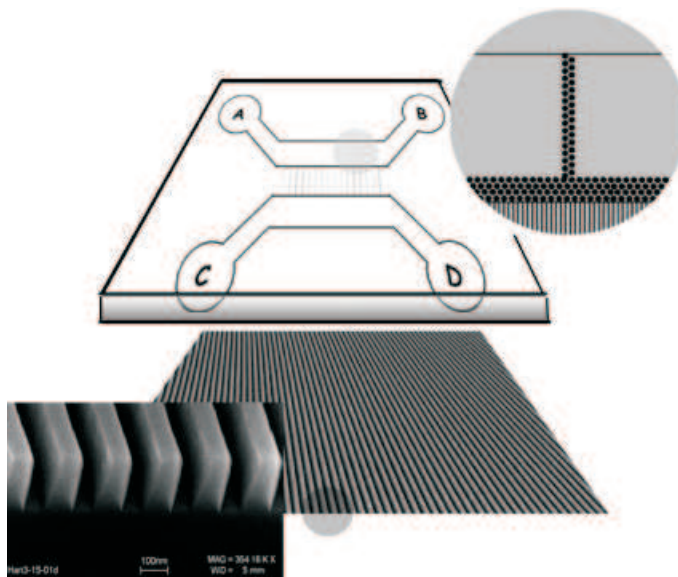


Figure 2.1: Microfluidic device used for measuring DNA elongation along the nanosized channels in Ref. [10]. DNA moves along the path from well A to well B. Driving voltage is used to transfer DNA into well C and D through the array of nanochannels. Posts A, B, C and D are $1 \mu\text{m}$ in diameter and separated by $2 \mu\text{m}$. The width of the nanochannels is 100 nm . This Figure is taken from Ref. [10]. Copyright (2004) National Academy of Sciences, USA.

possibility for continuous measurements of its length in the equilibrium state [10, 16, 17]. This is a decisive advantage of nano- and microfluidics for DNA analysis over other experimental techniques aimed at stretching DNA, such as optical or magnetic tweezers [18, 19, 20] and stretching of tethered polymers in uniform flow [21]. DNA extension along a channel has been measured directly for a wide range of channel widths from 30 up to 400 nm [10, 16, 17]. An example of the experimental setup is shown in Fig. 2.1. These measurements confirm previously obtained theoretical linear scaling of the polymer elongation along a cylinder with its contour length in both de Gennes and Odijk regimes. In the de Gennes regime, when the width of the channel is much smaller than the radius of gyration of an unconfined polymer, but larger than the persistence length of DNA (roughly 50 nm [22]), the effect of excluded volume plays a crucial role on the polymer's conformation. Decreasing of the width of the confinement leads to a change in scaling of the length from the de Gennes regime to the Odijk one. In the Odijk regime, where the width of the channel is comparable with the persistence length of the polymer, the stretching along the channel is dominated by the interplay of confinement and intrinsic DNA elasticity. The width of the channel not only changes the polymer's conformation, but also influences the relaxation dynamics of the polymer. Changes in the scaling

of the relaxation times of DNA confined in channels of different width showed that the crossover between these two regimes occurs when the width of the channel is equal to twice the persistence length of DNA [16].

However, it is impossible to trap a single DNA from a free polymer solution in a nanochannel without the help of any external mechanism, since DNA resists entry into the channel due to the loss of entropy inside the channel. Typically, a DNA strand is forced to move from a micron-sized reservoir into a channel under the action of an external electric field [11, 14, 17, 23, 24, 25, 26, 27, 28, 29] or pressure driven flow [11, 14, 30]. Driven by an external field, the polymer can enter the channel with one folded front end [23] as shown in Fig. 2.2 (a)-(b). When the field is turned off the polymer tries to unfold (compare Fig. 2.2 (c)-(d)). The dynamics of the unfolding has been experimentally observed using fluorescence microscopy and studied in rectangular channels with dimensions $215 \times 155 \text{ nm}^2$ and $150 \times 135 \text{ nm}^2$ (width by depth) [23]. Measurements of polymer elongation along the channel in folded and unfolded configuration show that the extension factor of the DNA segments in the overlapping region is larger than the one in the nonoverlapping region. This is the result of increased excluded volume interactions in the overlapping region, which are also the origin of the entropic force driving the polymer unfolding. The unfolding force measured in these experiments is 16 fN in the $215 \times 155 \text{ nm}^2$ channel and 22 fN in the $150 \times 135 \text{ nm}^2$ channel. These measurements are consistent with the entropic force driving segregation of two overlapping self-avoiding polymers computed in simulations and reported in Ref. [2]. When the polymer has relaxed along the channel after unfolding to its equilibrium length, one can switch on the field again to move the polymer towards the entrance of the channel and observe recoiling of the polymer. Polymer recoiling is a process of polymer movement from the low entropy region inside the channel to the high entropy region outside the channel where the polymer forms a coil [25, 28, 29, 31]. This is one example where the entropic forces induced by a confining channel drive the process, in this case, by pulling the polymer out of the confinement.

An external field can be used for studying relaxation dynamics of compressed DNA [26]. In these experiments, DNA driven by an electric field has been initially trapped inside a channel and then compressed due to a constriction of the channel, which blocks the polymer motion along the channel. After turning off the field, DNA quickly moves away from the constriction due to entropic repulsion of the conical shape of the constriction. The measured decompression time and the extension length show that the polymer elongation along the cylinder grows inverse exponentially according to the theoretical predictions obtained from the de Gennes model.

One of the examples of confined polymers, which can be observed *in vivo*, is the prokaryotic bacterium *Escherichia coli* (*E. coli*). Being a prokaryote, *E. coli* is a single-celled organism without a nucleus and has a rod-like shape. The typical

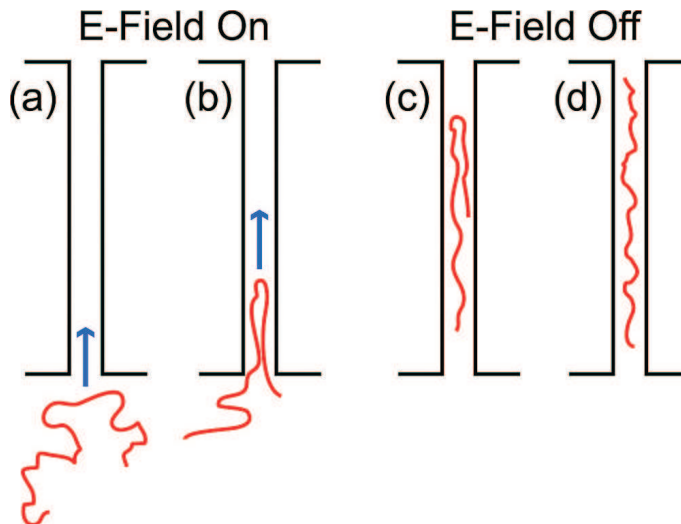


Figure 2.2: Overview of experimental procedure taken from Ref. [23]. (a) A long DNA molecule sits in a microchannel, adjacent to the entrance of a nanochannel. (b) The electric field (blue arrow) pulls the DNA into the nanochannel. Because the molecules entrance was initiated at some point along the backbone distinct from either of the ends, it enters the channel in a folded conformation. (c) Once the electric field is turned off, the DNA strand relaxes inside the nanochannel in a high energy folded state. It gradually unfolds, thereby reducing its conformational free energy. (d) The molecule has completely unfolded within the channel, extending to its equilibrium conformation. Reprinted with permission from S. L. Levy, J. T. Mannion, J. Cheng, C. H. Reccius and H. G. Craighead, *Nano Lett.*, 2008, 8 (11), pp 3839-3844. Copyright (2008) American Chemical Society.

size of its cellular shell is approximately $0.5 - 1 \mu m$ in diameter and $2 - 2.5 \mu m$ in length. The bacterium contains a single circular chromosome whose length is one order of magnitude larger than the cell length, thus the chromosome is tightly wrapped inside the cell. During cell division, all the information about the cell hidden in the chromosome has to be copied and distributed correctly to the emerging daughter cells. In bacteria, one can distinguish two main processes, which the chromosome undergoes while a bacterium is dividing, namely, chromosome replication and segregation of replicated strands. During replication, the double-stranded DNA molecule of the mother cell is split into two single strands, which are complemented by new base pairs to form two identical, double-stranded DNA molecules. The splitting and complementing happen concurrently, so that two daughter strands effectively grow from the original mother DNA [32]. The replicated strands move towards opposite sides of the growing cell until they are completely separated. The latter process is called segregation. When the segregation is completed, the cell division is terminated by the construction of the wall that splits two newborn cells, which are then ready to go through this cycle again. Note that the described above

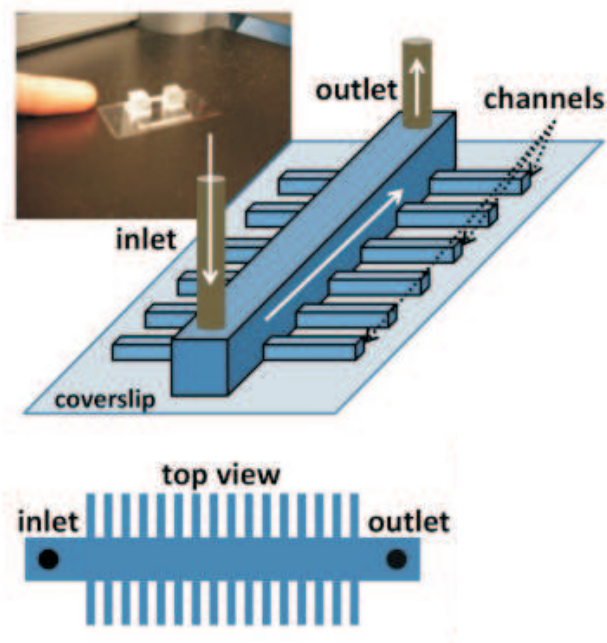


Figure 2.3: Schematic illustration of the microfluidic device used for growing *E. coli* in Ref. [33]. The device consists of channels for growing bacteria. The channels are adjacent to the trench where newborn bacteria flow off the channels. Reprinted from Current Biology, 20 /12, P. Wang, L. Robert, J. Pelletier, W. L. Dang, F. Taddei, A. Wright, S. Jun, Robust Growth of *Escherichia coli*, p1099-1103, Copyright (2010), with permission from Elsevier.

cycle reflects the main principles of prokaryotic cell division and its details depends on the specific type of bacteria.

With the development of microfluidic devices, it is possible to grow a synchronous population of single-cell bacteria in experiments, which can be used for analysis of replication and segregation processes [32, 33, 34, 35, 36]. Designed for this purpose microfluidic devices are highly controllable fluid flow systems using micron-scale valves and pressure gradients that can isolate cells without stress. Typically they are comprised of an array of microsized columns whose diameter is comparable to the diameter of a bacterium (see Fig. 2.3). For growing the next generation of bacteria, first of all, mother cells have to be immobilized at the closed bottom of the columns. For example, the immobilization can be achieved by attaching the bacterial flagella to a glass bead, which is then placed into the column [32, 34]. After the cell division of mother cells, the newborn cells flow off the columns from the open ends and they can be collected for further analysis. These devices allow one to change the natural conditions of cell growth and manipulate this process on a single cell level [36].

The common experimental technique used for analysis of cell division is flow cytometry, where forward light scattering in combination with DNA fluorescence allows one to investigate DNA replication. Specific places on the chromosome are labeled by different kinds of fluorescent markers. Then, tracing the position of markers, one can observe the progress of the chromosome division using Fluorescence In Situ Hybridization (FISH). In this way, many processes in bacteria can be visualized by snapshot, time-lapse or 3D microscopy.

Chromosome replication starts at a specific locus on the chromosome called *ori* (origin) and terminates at the locus *ter* (terminus), which is located at the opposite clock position of the *ori* on the chromosome. In experiments on *E. coli* one distinguishes two bacterial growth rates, namely, slow and fast rates. Slowly growing bacteria are characterized by the presence of one *ori* and one *ter*, meaning that the chromosome replicates only once during one cycle of cell division. Under fast growth conditions, replication is continuous and the chromosome of a newborn cell is already partially replicated. In this case, one can see the presence of two *oris* and a single *ter* on the chromosome. A schematic illustration of chromosome division of slow and fast growing bacteria is depicted in Fig. 2.4.

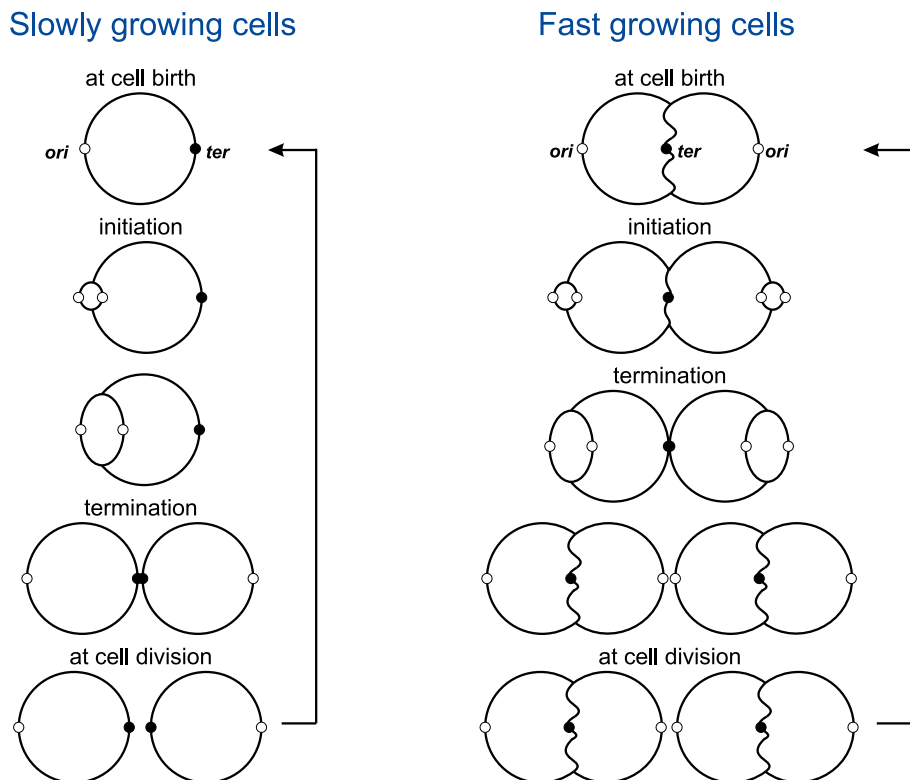


Figure 2.4: Schematic illustration of chromosome division of slow and fast growing bacteria. Adapted from Ref. [37].

One cycle of *E. coli* division under slow growth conditions takes around 120 minutes [32, 35, 38]. The entire chromosome replication takes one third of the whole cell cycle lasting 46 minutes. The beginning of this process was detected at $t = 17$ minutes after the initiation of the cell division by an increase in the cell concentration. Interestingly, the appearance of two *oris*, which have to be divided first, is detected only at $t = 31$ minutes. During the elapsed 14 minutes the replicated *oris* may have still been linked and therefore remain colocalized. With the loss of the linkage the *oris* can start segregation, thus, the loss of the linkage “triggers global chromosome movement which in turn mediates sister chromosome segregation” [32]. The appearance of two replicated *ters* is observed at $t = 82$ minutes, before the beginning of the construction of the cell wall (septation) separating the two newborn cells. The colocalization of *ters* was not observed. Septation is the last phase of the cell division which starts at $t = 98$ minutes and takes about 25 minutes.

Tracing the trajectories of *oris* and *ters* during the cell division, the authors of Ref. [32] constructed the spatial dynamics of these points on the chromosome, which is shown in Fig. 2.5 taken from Ref. [32]. At the beginning of the division process, the *ori* and *ter* are equidistant from the middle of the cell and separated by a distance equal to the half of the cell length. These positions are typically called the 1/4 and 3/4 positions. Prior to the replication the *ori* moves to the middle of the cell, whereas the position of the *ter* remains unchanged. During replication, when the *ori* has already replicated into two *oris* and the linkage between them has been lost, the *oris* segregate towards the opposite poles of the cell occupying the 1/4 and 3/4 positions. At the same time, *ter* moves to the middle of the cell, so that after its replication two *ters* segregate into the different regions from the middle of the cell, ensuring that each newborn cell will possess one entire chromosome. This spatial dynamics has been confirmed by later works, for example, in Ref. [35, 39].

A similar picture of the spatial dynamics of the chromosomes has been observed in computer simulations [1]. Simulating a replicating ring polymer trapped inside a cylinder of a finite size which grows during replication, two scenarios have been reproduced. The first scenario mimics the presence of the replication factory, which keeps just replicated *oris* colocalized, whereas this biological detail has been ignored in the second scenario. In both cases, the polymers have been entropically forced toward segregation without the action of any external forces. The spatial positions of replicated *oris* and *ter* observed during simulations differ depending on the scenario. Although the replicated *oris* seek to move to the opposite poles of the cylinder and the *ter* drifts toward the center of the cylinder in both scenarios, confirming that the segregation of chromosomes in bacteria is at least partially entropically driven, in the second scenario both events occur significantly later. Thus, the colocalization of replicated *oris* at the first stage of replication can facilitate chromosome segregation. However, the discussions about what kind of mechanisms apart of entropy are responsible for chromosome segregation in elongated bacteria

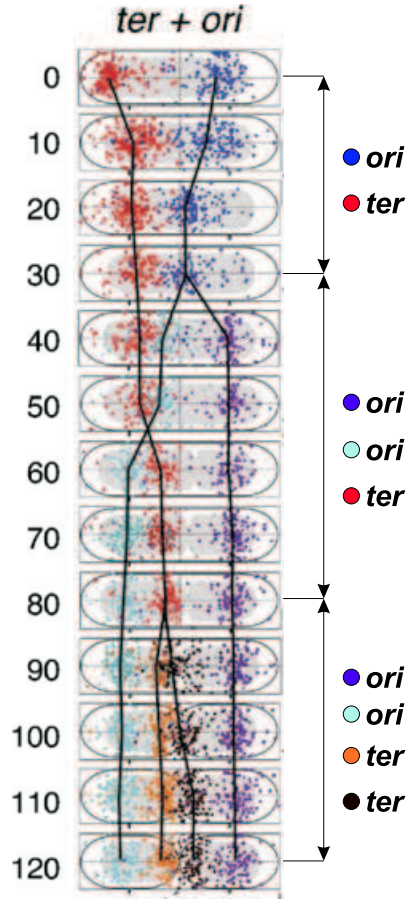


Figure 2.5: Schematic illustration of the spatial dynamics of *E. coli* chromosome during cell division under slow growth conditions. Figure is taken from Ref. [32]. Reprinted from Cell, 121 /6, D. Bates, N. Kleckner, Chromosome and Replisome Dynamics in *E. coli*: Loss of Sister Cohesion Triggers Global Chromosome Movement and Mediates Chromosome Segregation, p899-911, Copyright (2005), with permission from Elsevier.

are still ongoing [32, 35, 37, 38, 39].

Under fast growth conditions (see Fig. 2.4), the cycle of cell division is approximately twice as fast as that of slowly growing bacteria. Continuous replication of the chromosome affects its spatial organization [37]. In the beginning of the cell division the chromosome already possesses two arms, which are partially replicated. Each arm extends toward one of the cell poles and contains the *ori* to start the next round of replication. At the same time, the *ter*, located on the unreplicated part of the chromosome, moves from one of the cell poles toward the cell center, making the configuration of arms totally symmetric. This swapping of the *ori*'s and *ter*'s positions can be energetically driven. The chromosome near the *ter* region can be stretched when the cell was born, thus, the swapping is the compromise

which requires less free energy. While the replication of the unreplicated part of the chromosome occurs, a new round of the replication sets in, so that the chromosome starts duplicating from *oris* in the vicinity of the 1/4 and 3/4 positions in the cell. During this round, the two growing arms tend to avoid each other, which initiate segregation. Since the segregation is bidirectional, the arms form four copies, each of them occupying an eighth of the cell. The division is terminated with replication of *ter* and the following construction of the cell wall. Thus, since the next round of replication has been started before *ter* splitting, each daughter cell possesses a chromosome, which is partially replicated. The spatial chromosome organization along the longitudinal axis of the cell is summarized in distribution histograms shown in Fig. 2 of Ref. [37].

The same segregation tendency is observed along the radial axis of the cell. The distribution of the arm locations in the cell cross-section reveals that each arm occupies half of the cell and they do not change their location during the cell cycle regardless of the ongoing replication [37]. The *oris* are balanced by the arms, therefore, they are located at the center of the cell cross-section, whereas the *ter* is found at the periphery in the beginning of the cell cycle and then close to the center. Such a strict separation of the chromosome arms along the radial axis is consistent with the ring polymer model [6], according to which a ring polymer is represented as two parallel chains trapped inside imaginary tubes which are placed side by side. Computer simulations of nonreplicating ring polymers also show a single- and double-peak radial distribution for *ori* and arms, correspondingly, that is in agreement with the distributions obtained in the experiments [37]. In this simulations, the number of structural units and their size were chosen to be consistent with the number and size of structural units predicted for real *E. coli* [15]. The structural units can be considered as blobs [40], and the size of the blob is determined by the diameter of the confining cylinder for a single polymer. The cell width of the fast growing *E. coli* is around 800 – 900 nm, thus two arms, each composed of 440 nm structural units [15], can fit along the radial cell axis making the ring model suitable for modeling chromosomes under fast growth conditions. The slowly growing bacteria are slightly narrower (the cell width 600 – 700 nm). Only one arm of size of 440 nm can fit in this case, suggesting that the global conformation of the chromosome in slowly growing bacteria can be described by a linear polymer [37].

Using microfluidic devices one can experimentally study the micromechanical properties of *E. coli* chromosomes *in vitro* [15]. In these experiments the microfluidic device is comprised of thousands of 25 μm long microchannels whose width is comparable to the width of the cell (see Fig. 2.6 A). One end of each microchannel is closed, whereas the other end is connected to a reservoir filled with a chemical environment suitable for chromosomes. *E. coli* are loaded from the reservoir into the microchannels via diffusion. Centrifugation pushes the cells to the closed ends of the microchannels. Adding lysozymes to the surrounding media breaks the top of the

2.1. EXPERIMENTS ON CONFINED POLYMERS

cell membrane. This process is called lysis. After lysis the lysozymes are washed out and replaced with fluorescent proteins to visualize morphological changes occurring in the *E. coli*. After lysis the chromosome is released from its shell and expands like a spring along the microchannel. Measurements of the chromosome length with time show that the chromosome expands up to half its equilibrium length during the first 10 seconds and then continues in a slow mode until the chromosome reaches its equilibrium length within 10^3 seconds as shown in Fig. 2.6 B. The subsequent compression of the chromosome back to its size in *in vivo* is done using a micropiston which couples optical tweezers and the microchannels (see Fig. 2.6 C).

The force-compression curve measured during the experiments repeats the theoretical predictions based on an entropic spring model of polymers [41] qualitatively (see Fig. 3 in Ref. [15] and section 2.8.3 for theoretical details). Fitting the ex-

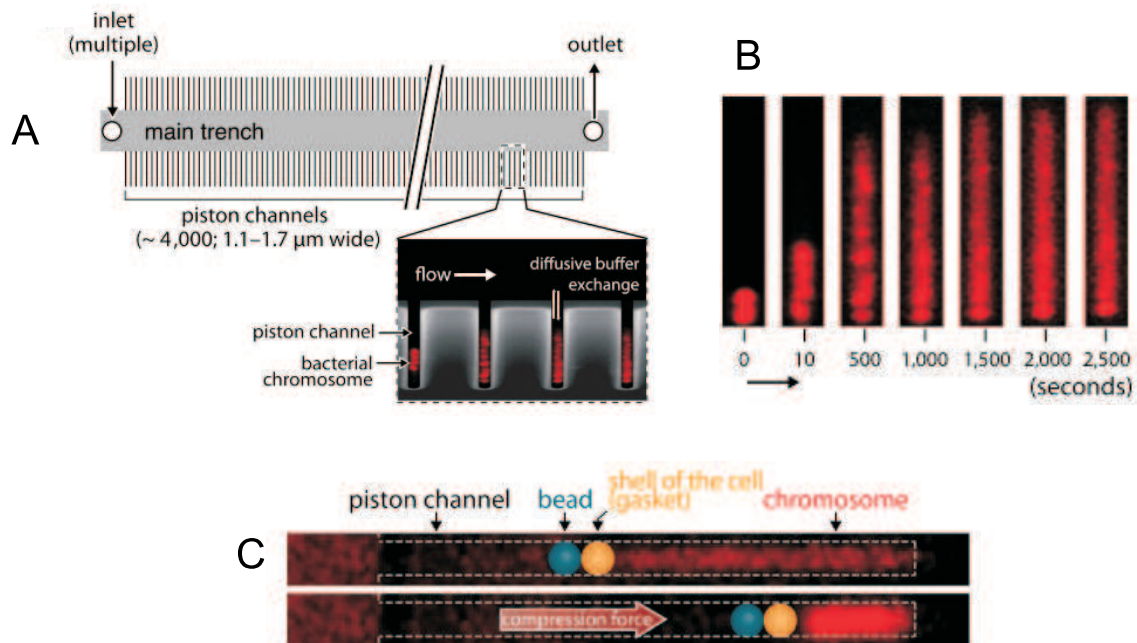


Figure 2.6: (A) Illustration of the microfluidic device: A main trench connects multiple inlets to one outlet, with thousands of protruding microchannels. Cells were loaded into microchannels (typically one per channel) and lysed, causing rapid expansion of chromosomes. (B) Time-lapse pictures showing expansion and morphological relaxation of the chromosome after lysis. (C) Mechanical compression of chromosomes. A polystyrene microbead held by optical tweezers was used to compress the chromosome against the closed channel end. The residual membrane of the cell after lysis was used as a gasket to prevent leakage of the chromosome. Figures are taken from Ref. [15]. Copyright (2012) National Academy of Sciences, USA.

perimental and theoretical results, it was found that 100 pN force and $10^5 k_B T$ of energy are required to compress the *E. coli* chromosome to its size *in vivo*, which is roughly 1/10 of the equilibrium length. Moreover, the agreement between the experimental measurements and theory makes the bead-spring model reasonable for modeling *E. coli* chromosomes as a linear or ring-like string of beads. Using the scaling of the equilibrium length of the chromosome, it was found that the size of these beads is in the range from 130 up to 440 nm [15], that is consistent with the size of the structural units previously measured using fluorescence correlation spectroscopy [42].

2.2 Entropy and basics of statistical physics

In this section, we introduce the key quantities of the statistical mechanics for understanding main concepts of polymer physics and computer simulations which are discussed later on. The brief overview presented here is based on the classical text books [43, 44, 45, 46].

The main focus in the thesis is entropy, since entropic effects play an important role in polymer physics and are crucial for the systems under investigation in this thesis. To define entropy, we consider a general system composed of a large number N of identical particles isolated in volume V . Such system can be described by the particle coordinates $\{\mathbf{r}^N\} = \mathbf{r}_1, \dots, \mathbf{r}_N$ and particle momenta $\{\mathbf{p}^N\} = \mathbf{p}_1, \dots, \mathbf{p}_N$. The combination of particle coordinates and momenta is a phase point in the phase space and corresponds to a microscopic state of the system. In thermal equilibrium, changes of the particle coordinates and momenta do not alter the macroscopic state of the system and macroscopic observables, such as energy, remain constant. Suppose that the energy in the equilibrium state is fixed at the value E and only some fluctuations δE around this value are possible. These fluctuations are small, so that they do not affect the properties of the macroscopic system, however, within the range δE there exists a great number of quantum states that are eigenvectors of the Hamiltonian \mathcal{H} of the system. Denote the number of eigenstates with energy E by $\Omega(N, V, E)$. The statistical meaning of this quantity is the number of ways that the particles can rearrange in equilibrium. Then, following the main assumption of statistical mechanics, that the system is equally likely to be found in any of its eigenstates, the entropy S of the system is defined as the logarithm of the number of eigenstates according to Boltzmann's relation

$$S(N, V, E) = k_B \ln \Omega(N, V, E), \quad (2.2.1)$$

where k_B is the Boltzmann constant. Note that the aforementioned assumption is not only valid for systems in equilibrium, but also for any other macroscopic states which have the same N , V and E .

2.2. ENTROPY AND BASICS OF STATISTICAL PHYSICS

Using the thermodynamic definition of temperature as the derivative of entropy, with respect to energy, the thermodynamic quantity beta is defined as

$$\beta = \frac{1}{k_B} \left(\frac{\partial S}{\partial E} \right)_{N,V} = \frac{1}{k_B T}, \quad (2.2.2)$$

where T is the absolute temperature of the system.

In statistical mechanics, the Hamiltonian \mathcal{H} of the system has the following general form:

$$\mathcal{H} = \sum_{i=1}^N \frac{\mathbf{p}_i^2}{2m} + V(\mathbf{r}_1, \dots, \mathbf{r}_N), \quad (2.2.3)$$

where the first term expresses the kinetic energy and $V(\mathbf{r}_1, \dots, \mathbf{r}_N)$ is the potential energy of the system. Here m denotes the mass of one particle. Using the Hamiltonian, one can determine the phase trajectory of the phase point in the phase space by solving the following equation of motion

$$\dot{\mathbf{r}}_i = \frac{\partial \mathcal{H}}{\partial \mathbf{p}_i}, \quad \dot{\mathbf{p}}_i = -\frac{\partial \mathcal{H}}{\partial \mathbf{r}_i}. \quad (2.2.4)$$

The quantity that describes the statistics of the phase trajectory is the phase space probability density $f(\mathbf{r}^N, \mathbf{p}^N, t)$, which is a probability of finding the system at time t at the phase point $(\mathbf{r}^N, \mathbf{p}^N)$. This probability has to be normalized so that

$$\int \int d\mathbf{r}^N d\mathbf{p}^N f(\mathbf{r}^N, \mathbf{p}^N, t) = 1. \quad (2.2.5)$$

If the system is in thermodynamic equilibrium, the probability density becomes independent of time t . In the canonical ensemble, where the number of particles N , accessible volume V and the temperature T of the system are fixed, the probability density can be written as

$$f(\mathbf{r}^N, \mathbf{p}^N) = \frac{\exp(-\beta \mathcal{H})}{Z}, \quad (2.2.6)$$

where Z is the canonical partition function determined via the Hamiltonian of the system as

$$Z = \int \int d\mathbf{r}^N d\mathbf{p}^N \exp(-\beta \mathcal{H}). \quad (2.2.7)$$

The thermodynamic potential in the canonical ensemble is the Helmholtz free energy $\mathcal{F} = U - TS$, where U is the internal energy and S denotes the entropy. In statistical mechanics, the free energy is determined via the partition function Z as follows

$$\mathcal{F} = -k_B T \ln Z. \quad (2.2.8)$$

This relation between the thermodynamic potential \mathcal{F} and the partition function Z establishes the link between statistical mechanics and thermodynamics.

2.3 Polymer theory

Polymer physics is a relatively young branch of physics, which only originated at the beginning of the 20th century. Although mankind was always surrounded by natural polymers like silk or natural rubber and has been using them for many centuries, people did not identify them as macromolecules. Even in the middle of the 19-th century, when chemists were already able to synthesize polymers these macromolecules were considered as large colloids composed of small molecules with mysterious bonds holding them together. Only in 1920 Staudinger was the first who proposed a hypothesis that these molecules, which were named as polymers or macromolecules, consists of many repeating elementary units called monomers and this units are linked by covalent bonds. This was the starting point for polymer science and developing the main theoretical concepts of polymer physics, which are discussed in this section. To make a consistent overview we begin with a description of an ideal chain conformation, then continue with a conformation of a self-avoiding chain and conclude with conformations of a self-avoiding chain in a tube. The content of this section is based on well-known books on polymer physics [22, 47, 48, 49, 50].

2.3.1 Conformations of ideal polymers

Let us consider a polymer chain composed of $n \gg 1$ monomers connected by bonds (see Fig. 2.7). Such a chain is called ideal if any pair of monomers i and j separated by a sufficient number of bonds along the chain ($|i-j| \gg 1$) do not interact with each other at any distances. An ideal polymer, as any other polymer, has many potential conformations. A conformation is the spatial structure of a polymer determined by the relative positions of its monomers. The conformations that a polymer can create depend on its flexibility. There are several models of an ideal polymer chain where the control of its flexibility is based on assumptions restricting the range of allowed bond and torsion angles. The most common examples of these models are the freely joined chain model, freely rotating chain model and worm-like chain model. To demonstrate the difference between ideal and real chains, it is sufficient to take the simplest model which is a freely joined chain model. According to this model all bond angles are equally likely and independent of each other. All bonds are of equal length $l = |\mathbf{r}_i|$, where \mathbf{r}_i is a bond vector between monomers i and $i-1$.

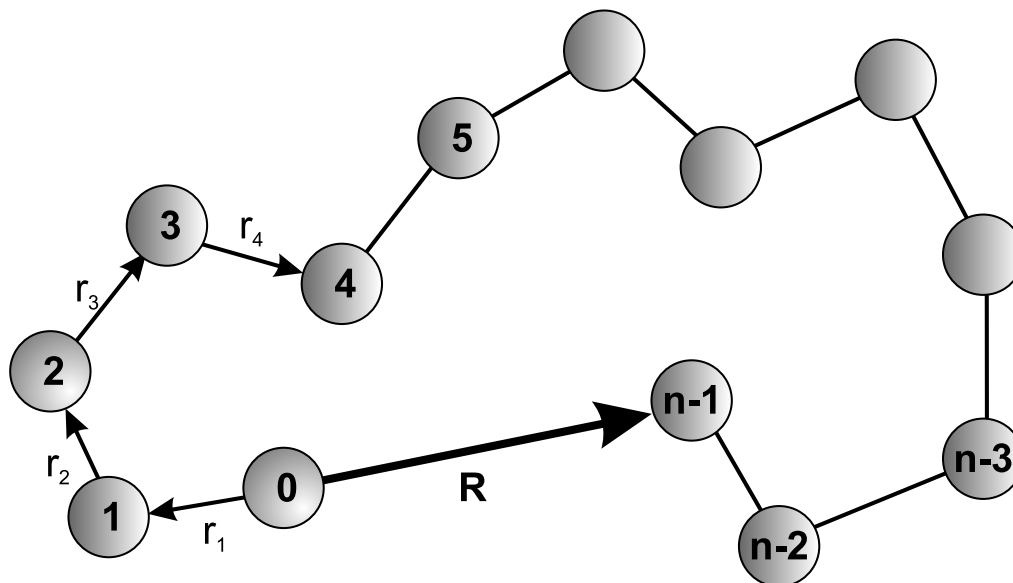


Figure 2.7: Conformation of an ideal chain composed of n monomers, which are linked by bonds. For a freely-jointed chain all bond vector \mathbf{r}_i are of the equal length l .

The simplest quantity to characterize the size of the ideal chain is the end-to-end vector. It is determined as the sum of all bond vectors

$$\mathbf{R} = \sum_{i=1}^n \mathbf{r}_i. \quad (2.3.1)$$

However, the end-to-end vector averaged over all possible states of the polymer is zero $\langle \mathbf{R} \rangle = 0$, because the configurations with end-to-end vector \mathbf{R} and $-\mathbf{R}$ are equally probable. For this reason the mean-square end-to-end distance is used instead:

$$\langle R^2 \rangle = \langle \mathbf{R} \cdot \mathbf{R} \rangle = \sum_{i=1}^n \sum_{j=1}^n \langle \mathbf{r}_i \cdot \mathbf{r}_j \rangle. \quad (2.3.2)$$

Here, $\langle \cdot \rangle$ denotes the ensemble average. By definition the scalar product of bond vectors can be written as $\mathbf{r}_i \cdot \mathbf{r}_j = l^2 \cos \theta_{ij}$, where θ_{ij} is a bond angle between bond vectors \mathbf{r}_i and \mathbf{r}_j . Since directions of bonds of an ideal polymer are not correlated, the angle θ_{ij} can vary in the range from 0 to 2π with equal probability for $i \neq j$. Therefore the scalar product of bond vectors averaged over all monomer positions is $\langle \mathbf{r}_i \cdot \mathbf{r}_j \rangle = l^2 \langle \cos \theta_{ij} \rangle = 0$ if $i \neq j$ and the only contributions to the mean-square end-to-end distance give the scalar products of equal bond vectors. Thus, the mean-square end-to-end distance is written as

$$\langle R^2 \rangle = \sum_{i=1}^n \langle \mathbf{r}_i \cdot \mathbf{r}_i \rangle = nl^2. \quad (2.3.3)$$

The mean-square end-to-end distance allows us to estimate the size of the polymer as $R = \langle R^2 \rangle^{1/2} = n^{1/2}l$. Obviously, R is significantly less than the polymer contour length $L = nl$. This means that polymers very rarely form stick-like configurations, but they are rather entangled to a coil due to polymer flexibility. The flexibility is an essential property of polymers. The mechanism of the flexibility, however, can differ depending on polymer type and its chemical details. In order to construct a universal model independent of the flexibility mechanism one needs to introduce a quantitative parameter, which is a measure of the polymer flexibility. The Kuhn length is such a parameter which is associated with the size of an actual polymer and defines a length scale beyond which correlations between polymer segments do not play a role. Indeed, in a typical polymer there are correlations between neighboring bonds and only distant bonds are uncorrelated, implying that $\langle \cos \theta_{ij} \rangle = 0$ holds only when $|i-j| \rightarrow \infty$ and the sum over all bond vectors converges to a finite value denoted by $C'_i = \sum_{j=1}^n \langle \cos \theta_{ij} \rangle$. Then, the mean-square end-to-end distance given by eq. (2.3.3) converts to

$$\langle R^2 \rangle = l^2 \sum_{i=0}^n C'_i = nl^2 C_n, \quad (2.3.4)$$

where $C_n = \sum_{i=1}^n C'_i/n$ is the Flory characteristic ratio defined as the average of the values C'_i over all polymer bonds. Due to the absence of correlations between the distant bonds, C_n converges to a finite value C_∞ for a infinitely long polymers ($n \rightarrow \infty$). Thus, the approximation of the mean-square end-to-end distance for a long polymer can be expressed in the following form

$$\langle R^2 \rangle \approx nl^2 C_\infty. \quad (2.3.5)$$

Note that the mean-square end-to-end vector remains proportional to the number of bonds along the polymer and the square of the bond length, however, now the correlations of neighboring bonds are also taken into account. This allows us to introduce the concept of a polymer Kuhn segment by treating a polymer as a sequence of N freely joined segments of Kuhn length a . The Kuhn length is determined by the relation $\langle R^2 \rangle = La$, where $L = Na = nl$ is the contour length of the actual polymer. Each of the segments contains a number of polymer bonds, beyond which the bond correlations are neglected. Thus, the number of Kuhn segments N is equal to $N = La/C_\infty nl^2$. This model is a universal model describing all ideal polymers independent of the local chemical polymer structure. Throughout this thesis we will

use this model for ideal chains and denote the number of monomers by N and a as the monomer size. Then, the size of an ideal polymer chain is expressed as follows

$$R = aN^{1/2}. \quad (2.3.6)$$

Another quantity that can characterize the size of a polymer is the radius of gyration. The square radius of gyration is the mean distance between monomers and the polymer's center of mass and given by

$$R_g^2 = \frac{1}{N} \sum_{i=0}^{N-1} (\mathbf{R}_i - \mathbf{R}_{cm})^2, \quad (2.3.7)$$

where the vector \mathbf{R}_i is the position vector of the i -th monomer and \mathbf{R}_{cm} is the position vector of the polymer's center of mass:

$$\mathbf{R}_{cm} = \frac{\sum_{i=0}^{N-1} m_i \mathbf{R}_i}{\sum_{i=0}^{N-1} m_i} = \frac{\sum_{i=0}^{N-1} \mathbf{R}_i}{N}. \quad (2.3.8)$$

Note that this assumes that all monomers have the same mass which is a reasonable assumption for most polymers. In comparison with the end-to-end distance, which can be easily calculated for linear polymers, the radius of gyration allows one to estimate the size of polymers of any architecture, such as branched or ring polymers, where the end-to-end distance is not well defined.

The configurations of an ideal chain composed of N monomers can be described by a three-dimensional random walk of monomers since all interactions of distant monomers are neglected and there are no correlations between bond directions. Assume that each step of the random walk is of length a and independent of previous steps. The latter means that the walk can come back to a site which has already been visited.

If the origin of a random walk is linked with one of the polymer ends, the probability distribution function to find the polymer with the end-to-end vector $\mathbf{R} = (R_x, R_y, R_z)$ is equal to the probability distribution function that the random walk finishes at the point \mathbf{R} after N steps. Then the probability of this walk ending within a volume $dR_x dR_y dR_z$ of the point with displacement vector \mathbf{R} is $P(\mathbf{R}, N) dR_x dR_y dR_z$. Since all three components of the three-dimensional random walk are independent of each other, each of them can be represented as a one-dimensional random walk and the probability distribution in three dimensions can be written as:

$$P_{3d}(\mathbf{R}, N) = P_{1d}(R_x, N) dR_x P_{1d}(R_y, N) dR_y P_{1d}(R_z, N) dR_z. \quad (2.3.9)$$

It is known that a one-dimensional random walk along, for example, the x axis obeys a Gaussian distribution with zero mean value $\mu = 0$ and mean-squared displacement $\sigma^2 = \langle R_x^2 \rangle$ and the probability distribution function in this case is given by the following equation:

$$P_{1d}(\mathbf{R}, N) = P(R_x, N)dR_x = \frac{1}{\sqrt{2\pi\langle R_x^2 \rangle}} \exp\left(-\frac{R_x^2}{2\langle R_x^2 \rangle}\right). \quad (2.3.10)$$

However, in three dimensions the mean-square displacement $\langle \mathbf{R}^2 \rangle$ given by eq. (2.3.6) is composed of three equivalent components of independent one-dimensional walks:

$$\langle \mathbf{R}^2 \rangle = \langle R_x^2 \rangle + \langle R_y^2 \rangle + \langle R_z^2 \rangle = Na^2. \quad (2.3.11)$$

Therefore the mean-square displacement of each one-dimensional walk is simply one third of the total mean-square displacement $\langle \mathbf{R}^2 \rangle$. This leads to the following final probability distribution function of three-dimensional walk which ends at the point \mathbf{R} :

$$P_{3d}(\mathbf{R}, N) = \left(\frac{3}{2\pi Na^2}\right)^{3/2} \exp\left(-\frac{3\mathbf{R}^2}{2Na^2}\right). \quad (2.3.12)$$

Using the equivalence between a random walk and the ideal chain, eq. (2.3.12) is nothing else but the probability distribution function of all polymer conformations with the end-to-end vector \mathbf{R} :

$$P_{3d}(\mathbf{R}, N) = \frac{\Omega(\mathbf{R}, N)}{\int \Omega(\mathbf{R}, N)d\mathbf{R}}, \quad (2.3.13)$$

where $\Omega(\mathbf{R}, N)$ denotes the number of conformations of a polymer composed of N monomers with the end-to-end distance \mathbf{R} . Knowing the probability distribution function, one can calculate the entropy of an ideal chain as follows

$$\begin{aligned} S(N, \mathbf{R}) &= k_B \ln \Omega(N, \mathbf{R}) = k_B \ln P_{3d}(\mathbf{R}, N) + k_B \ln \left[\int \Omega(\mathbf{R}, N)d\mathbf{R} \right] = \\ &= -\frac{3}{2}k_B \frac{\mathbf{R}^2}{Na^2} + \frac{3}{2}k_B \ln \left[\frac{3}{2\pi Na^2} \right] + k_B \ln \left[\int \Omega(\mathbf{R}, N)d\mathbf{R} \right], \end{aligned} \quad (2.3.14)$$

Obviously, only the first term in eq. (2.3.14) depends on the end-to-end vector \mathbf{R} , therefore the sum of the remaining two terms can be written as the entropy of an ideal chain with zero end-to-end distance $S(N, 0)$. The interactional energy $U(N, \mathbf{R})$ also does not depend on the end-to-end distance due to the absence of interactions between distant monomers and can be replaced by the interactional energy of a

polymer with zero end-to-end distance $U(N, \mathbf{R}) = U(N, 0)$. Then, the Helmholtz free energy of an ideal chain $\mathcal{F}(N, \mathbf{R}) = U(N, \mathbf{R}) - TS(N, \mathbf{R})$ is expressed as follows

$$\mathcal{F}(N, \mathbf{R}) = \frac{3}{2}k_B T \frac{\mathbf{R}^2}{Na^2} + \mathcal{F}(N, 0), \quad (2.3.15)$$

where $\mathcal{F}(N, 0) = U(N, 0) - TS(N, 0)$ is the free energy of an ideal polymer with zero end-to-end distance. Thus, the free energy of an ideal chain is given by the entropic term. The larger the end-to-end distance of the ideal polymer is, the fewer conformations a polymer can create leading to an entropy decrease, and as a result the free energy increases quadratically with the polymer end-to-end distance. This implies that the deformation of an ideal polymer due to, e.g. stretching, has a free energy cost which is purely entropic in nature. Moreover, polymer elasticity satisfies a Hooke's law, since the separation of polymer ends by a distance R requires a force f which can be found as follows

$$f = \frac{\partial \mathcal{F}(N, \mathbf{R})}{\partial \mathbf{R}} = \frac{3k_B T}{Na^2} \mathbf{R}, \quad (2.3.16)$$

This force f scales linearly with R like the force of an elastic spring with an entropic spring constant $3k_B T/Na^2$. The proportionality of the elastic spring constant to the temperature T is a signature of entropic elasticity which distinguishes polymers from other materials. Polymers can be more easily stretched at lower temperatures in contrast to e.g. solids which become softer at high temperatures.

2.3.2 Conformations of self-avoiding polymers

Polymer conformations change dramatically if we include the effect of monomer-monomer interactions which were neglected in the previous section. To show this, we consider a polymer consisting of N monomers of size a , but this time each of the monomers has an excluded volume v . Such polymers are called self-avoiding polymers. Due to the excluded volume, monomers of a self-avoiding polymer effectively repel each other on small length scales, leading to an increase of polymer size compared to an ideal polymer, and as a consequence a reduction in the entropy of the polymer. In order to find the size of a self-avoiding polymer one needs to determine a balance between the effective repulsion energy of monomers which swells the polymer and the entropy loss due to such deformation from the ideal state. One of the most successful theories estimating this balance is the Flory theory which is a mean-field theory. Following Flory's idea, let us assume that the self-avoiding polymer is swollen to the size R which is larger than the size of an ideal polymer chain $R_0 = aN^{1/2}$. Then the volume occupied by the polymer scales like R^3 . Within this volume we assume that monomers are uniformly distributed and the correlations between them are ignored. The probability of a monomer to be found within the

excluded volume of another monomer is a product of the excluded volume v and the monomer number density $N/V \sim N/R^3$. The energetic cost of such an overlap is of order of $k_B T$ per monomer. Then the free energy of excluded volume interactions for all N monomer is found to be

$$\mathcal{F}_{int} \approx k_B T v \frac{N^2}{R^3}. \quad (2.3.17)$$

The entropic contribution to the free energy is the free energy required to stretch the ideal polymer to the end-to-end distance R (see eq. (2.3.15)):

$$\mathcal{F}_{ent} \approx k_B T \frac{R^2}{a^2 N}. \quad (2.3.18)$$

Summing up these two contributions we obtain the free energy of a self-avoiding polymer depending on its size:

$$\mathcal{F} \approx k_B T \left(v \frac{N^2}{R^3} + \frac{R^2}{a^2 N} \right). \quad (2.3.19)$$

Minimization of the free energy gives the size of the self-avoiding polymer R_F in the equilibrium state:

$$R_F \approx v^{1/5} a^{2/5} N^{3/5}. \quad (2.3.20)$$

The obtained equation shows that the size of the self-avoiding polymer still scales with number of monomers, but with the different power law than the ideal polymer. The ratio of the sizes of a self-avoiding and an ideal polymers composed of an equal number of monomers, $R_F/R_{id} \approx (vN^{1/2}/a^3)^{1/5}$, shows that the size of a self-avoiding polymer is indeed significantly larger than that of an ideal chain.

The Flory estimation of the free energy can also be written in a general form for an arbitrary dimension d :

$$\mathcal{F} \approx k_B T \left(v \frac{N^2}{R^d} + \frac{R^2}{a^2 N} \right). \quad (2.3.21)$$

Here only the free energy of excluded volume interactions depends on the dimensionality, since the entropic term is the entropy of an ideal polymer which is independent of d . Minimization of the generalized form of the free energy leads to a universal power law for the scaling of the polymer size with the number of monomers:

$$R_F \sim N^\nu. \quad (2.3.22)$$

The exponent ν in eq. (2.3.22) is called the Flory exponent and depends on the dimension d as follows

$$\nu = \frac{3}{d+2}. \quad (2.3.23)$$

Therefore $\nu = 3/5$ in three-dimensions as demonstrated above, $\nu = 3/4$ in two-dimensions and $\nu = 1$ in one-dimension. The derivation of the linear scaling of polymer size with N in one-dimension will be shown below for a polymer confined in a tube.

It is important to note that both contributions to the free energy (2.3.19) obtained using Flory approach are large overestimations. First of all, the energy of excluded volume interactions is computed omitting monomer correlations, while the calculation of the entropic term is based on the statistics of ideal chains. Nevertheless, these two errors mostly cancel each other giving an accurate prediction of the polymer size. More sophisticated theories based on the renormalization group technique give the exact value of the Flory exponent $\nu = 0.588$ [51, 52, 53, 54] which is very close to the one obtained by the relatively simple Flory approach. Experimental measurements of the size of different polymers in good solvent confirm the scaling (2.3.22) with $\nu \approx 0.59$ [55, 56].

The problem of estimating of the effective interaction potential between two identical self-avoiding polymers arises in many fields of polymer physics. Our particular interest here is to find the free energy cost of two overlapping polymers in 3D. Let us consider two identical self-avoiding polymers in 3D, each composed of the same number of monomers N . Knowing that the size of each polymer R scales according to eq. (2.3.22), we can estimate the overlap volume for two strongly overlapping polymers $V \sim R^3 \sim N^{3\nu}$, and the average monomer concentration within this volume is then $\rho \sim N/V \sim N^{1-3\nu}$. The free energy of the interaction between two polymers scales with the number of monomer contacts N_{cont} in the overlap region between the monomers belonging to different polymers:

$$\mathcal{F}_{ov} \sim k_B T N_{cont}. \quad (2.3.24)$$

If we assume that the monomers are independently distributed within the overlap volume V , N_{cont} is equal to the product of the number of monomers N and the contact probability for each of these monomers p_{cont} which is $\rho = N/V$. This leads to the following

$$N_{cont} \sim N p_{cont} \sim N \rho \sim N^{2-3\nu} \sim N^{1/5}. \quad (2.3.25)$$

Thus, the free energy of two overlapping polymers scales like $\mathcal{F}_{ov} \sim k_B T N^{1/5} \gg k_B T$. With this, one could conclude that the overlap of polymers with excluded volume interaction is energetically unfavorable, therefore the polymer coils strongly repel each other and are practically impenetrable. However, the obtained scaling has the same error as eq. (2.3.17) predicted by Flory since both scalings are based on the same assumption of ignoring monomer correlations.

The monomers are not independently distributed within the volume occupied by a polymer, but they are connected along the backbone. Therefore, if two monomers belonging to different polymers are in contact, both polymers feel this monomer contact due to polymer connectivity. This leads to an additional repulsion of the overlapping polymers and thus the contact probability has to be calculated in a different manner. To obtain the correct contact probability let us take one monomer of one polymer and look at the local concentration of monomers $\rho(r)$ belonging to the second polymer with respect to the chosen monomer. Obviously, this concentration, which depends on the distance r , is the number of monomers n within the volume $\sim r^3$ divided by this volume. On the other hand, the number of monomers within the volume $\sim r^3$ corresponds to the number of monomers which compose a polymer of size $r \sim n^\nu$ due to polymer connectivity. Therefore the local monomer concentration can be written in the following form

$$\rho(r) \sim \frac{r^{1/\nu}}{r^3} \sim r^{(1-3\nu)/\nu}. \quad (2.3.26)$$

Using this equation, which was obtained by Edwards [57, 58], we can express the number of monomers n within a volume r^3 as $n \sim r^{1/\nu} \sim \rho(r)^{1/(1-3\nu)}$. Therefore, the probability of the chosen monomer to have a contact with monomers of the second polymer is $p_{cont} = 1/n \sim \rho(r)^{1/(3\nu-1)}$. The contact probability calculated in such a way is distance dependent and decays with the local monomer concentration, since the larger the distance from the chosen monomer is, the more monomers surround it. Using this contact probability, Grosberg showed that the free energy of interactions of two polymers in overlap is of order of $k_B T$ [59]. The correct estimation of the overlap free energy is

$$\mathcal{F}_{ov} \sim k_B T N p_{cont}(r = N^\nu) \sim k_B T N (N^{1-3\nu})^{1/(3\nu-1)} \sim k_B T. \quad (2.3.27)$$

From eq. (2.3.27) one can conclude that polymers in 3D overlap rather frequently due to a relatively low free energy cost in contrast to the aforementioned Flory predictions [59]. This also demonstrates the importance of monomer correlations which have to be taken into account while calculating polymer properties such as, e.g., the osmotic pressure of polymer solutions [58]. In addition, attention has to be drawn to the fact that the free energy of the overlap of two polymers in 3D is independent of the number of monomers they comprise. This universal scaling is important for the blob model which will be introduced and discussed in the next section.

2.3.3 Polymer under tension. The de Gennes blob model

One of the most important models in polymer physics is de Gennes' blob model which was proposed by de Gennes in the 1970s. This model is extremely useful and robust in predicting various static and dynamic properties. To introduce the

concept of the blob model it is convenient to consider a self-avoiding polymer under tension. Let a polymer consisting of N monomers of size a be stretched up to the end-to-end distance R_t . The stretching force is constant and applied to both ends of the polymer in opposite directions as shown in Fig. 2.8. Here, the key idea lies in understanding that the conformational entropy of such a deformed polymer arises from the freedom of polymer sections at small lengths. Let us denote this length as ξ . Then we can split the polymer into a sequence of spherical sections of size ξ , each containing an equal number of monomers. Such sections are called blobs and are also represented in Fig. 2.8. A blob is characterized as a section of polymer such that on a length scale smaller than one blob the polymer does not feel an external perturbation (tension in this case) and behaves like a free self-avoiding polymer inside each blob. Assuming that each blob consists of g monomers, the size ξ according to eq. (2.3.20) is

$$\xi \approx ag^\nu, \quad (2.3.28)$$

where $\nu = 3/5$. Then, the end-to-end distance of the stretched polymer is expressed as the product of one blob size and number of such blobs:

$$R_t \approx \xi \frac{N}{g} \approx \frac{Na^{1/\nu}}{\xi^{(1-\nu)/\nu}} \approx \frac{R_F^{1/\nu}}{\xi^{(1-\nu)/\nu}}. \quad (2.3.29)$$

Solving this equation for the blob size ξ we obtain that $\xi = (R_F/R_t)^\nu$. Excluded volume interactions make the overlap of blobs energetically unfavorable with the free energy cost $k_B T$ per blob as demonstrated in the previous section. Therefore, the free energy of the stretched polymer $\mathcal{F}(N, R_t)$ can be written as

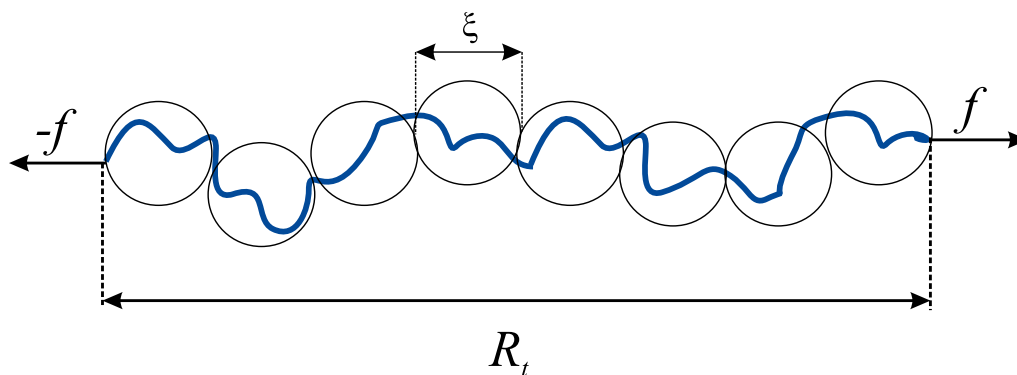


Figure 2.8: A self-avoiding polymer under tension. The polymer is stretched bidirectionally up to an end-to-end distance R_t under the action of a force f . The de Gennes blob model is applied to the polymer: the polymer is divided into a sequence of blobs of size ξ . Each blob contains an equal number of monomers.

$$\mathcal{F}(N, R_t) \approx k_B T \frac{N}{g} \approx k_B T \frac{R_t}{\xi} \approx k_B T \left(\frac{R_t}{R_F} \right)^{1/(1-\nu)}. \quad (2.3.30)$$

The stretching force f is the derivative of the free energy $\mathcal{F}(N, R_t)$ with respect to the end-to-end distance R_t :

$$f = \frac{\partial \mathcal{F}(N, R_t)}{\partial R_t} \approx \frac{k_B T}{R_F} \left(\frac{R_t}{R_F} \right)^{\nu/(1-\nu)}. \quad (2.3.31)$$

The stretching force f for self-avoiding polymers does not depend linearly on the polymer elongation unlike ideal chains. Furthermore, stretching an ideal chain to the end-to-end distance R_t requires more force than stretching a self-avoiding polymer to the same end-to-end distance. The nonlinear dependence of the tension force with polymer elongation was derived by Pincus [60] and, therefore, the blobs under tension are often called Pincus blobs.

2.3.4 Polymers under compression. Cylindrical confinement

For a confined polymer, excluded volume effects become more pronounced due to the additional confinement compression, which leads to an increase of the polymer's free energy as well as the polymer's size. To elucidate this effect, we consider a self-avoiding polymer composed of N monomers trapped inside a cylindrical tube of infinite length (see Fig. 2.9). The diameter of the tube D defines a natural size for the compression blobs. Therefore, the polymer can be considered as a sequence of blobs of size D . Inside each blob, the polymer does not feel the presence of the confinement and obeys the statistics of a free polymer. Then, using eq. (2.3.28) we can write

$$D \approx a g^\nu, \quad (2.3.32)$$

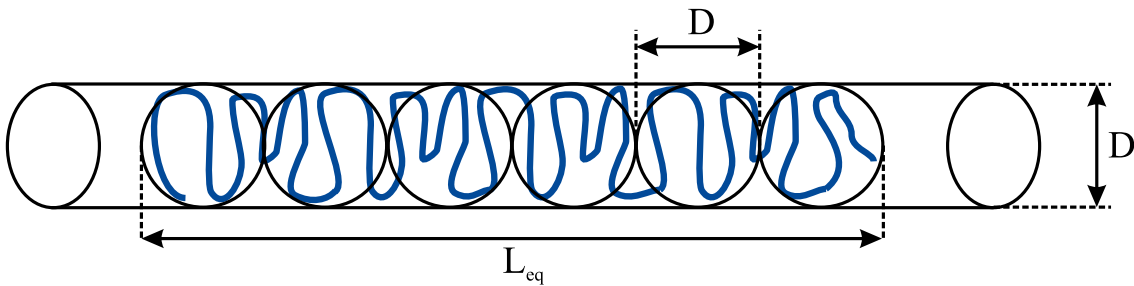


Figure 2.9: A self-avoiding polymer trapped inside a cylindrical tube of diameter D . The length of the tube is infinite. The polymer is split into a sequence of blobs of size D .

$$D \approx ag^{1/2}. \quad (2.3.36)$$

Therefore, the corresponding number of monomers per blob is $g \approx (D/a)^2$. The elongation of the ideal polymer along the cylinder can be estimated as a random walk of N/g blobs of size D along the tube. Applying eq. (2.3.6) for blobs, we obtain that the elongation of the ideal chain is the same as the size of the corresponding unconfined ideal chain:

$$R_{||} \approx D \left(\frac{N}{g} \right)^{1/2} \approx aN^{1/2} \approx R_{id}. \quad (2.3.37)$$

From the obtained scaling for elongation of an ideal polymer along the tube, we can conclude that the presence of confinement does not change the size of ideal polymers. This is in contrast to self-avoiding polymers where confinement leads to polymer stretching. This behavior of ideal polymers is rather expected, since the random walk statistics which describes conformations of ideal polymers requires coordinate independence at each step of the walk. Therefore, the deformation of the walk in one direction along the confining tube does not affect the walk in another direction. Comparing the elongation of ideal and self-avoiding polymers trapped in equivalent cylinders, one sees that the self-avoiding polymer occupies more space along the cylinder than the corresponding ideal polymer, because blobs of an ideal polymer are mutually permeable due to the absence of excluded volume interactions, whereas blobs of a self-avoiding chain are strongly repulsive.

Now we apply the Flory approach to a self-avoiding polymer composed of N monomers of size a confined in a tube of diameter D . The entropic term of the free energy in eq. (2.3.19) remains unchanged, since confinement does not affect the size of an ideal chain along the cylinder. However, the presence of confinement influences the energy of the excluded volume interactions, since monomers are restricted by the cylinder. The volume that monomers can occupy depends on the end-to-end distance R of the polymer as RD^2 . Following the discussion in section 2.3.2, the probability of one monomer to be excluded from the volume occupied by another monomer is $a^3N/(RD^2)$, where $N/(RD^2)$ is the number density of monomers in the cylinder. This probability times $k_B T$ gives the energetic cost per monomer exclusion. The energy of the excluded volume interactions of the whole chain is N times larger and written as $a^3N^2/(RD^2)$. Summing up the entropic contribution and the energy of the excluded volume we obtain the free energy of the self-avoiding polymer confined in a cylinder in the following form:

$$\beta\mathcal{F}(R, N, D) \sim \frac{R^2}{a^2N} + \frac{a^3N^2}{D^2R}, \quad (2.3.38)$$

where $\beta = 1/k_B T$. The minimization of the free energy with respect to the end-to-end distance R gives equilibrium length of the polymer $L_{eq} = Na^{1/\nu}D^{(1-1/\nu)}$ (with

the Flory exponent $\nu = 3/5$) which is consistent with equilibrium length (2.3.34) obtained using the de Gennes blob model. However, the Flory approach does not predict the equilibrium free energy correctly. Substitution of the equilibrium length into eq. (2.3.38) gives the free energy in equilibrium $\beta\mathcal{F} \sim N(a/D)^{4/3}$, that contradicts the correct scaling obtained by de Gennes using the concept of blobs $\beta\mathcal{F} \sim N(a/D)^{5/3}$.

Recently Jun and coworkers have reconsidered the Flory approach for cylindrical confinement and renormalized it in such a way that it gives not only correct scaling for the polymer size, but it is also valid for free energy calculation of a polymer near its equilibrium length [41, 61]. The basic idea is to merge the de Gennes blob model and the Flory approach. According to the de Gennes blob model a polymer confined in a cylinder of diameter D is represented as a linear sequence of blobs of size D . The linear structure of blobs is dictated by self-avoidance which makes the overlap of blobs energetically unfavorable. This allows us to introduce a new length-scale of polymer self-avoidance which is related to the diameter of the cylinder D , and consider a polymer as a structure of self-avoiding blobs. This argument provides the basis of the renormalization of the Flory approach, where the size of a self-avoiding unit a in eq.(2.3.38) has to be replaced by D and, therefore, N rescales as number of blobs $n_{bl} = N/g$ with $g = (D/a)^{1/\nu}$ monomers per blob. After the renormalization eq. (2.3.38) transforms to

$$\beta\mathcal{F}(R, N, D) \sim \frac{R^2}{n_{bl}D^2} + \frac{Dn_{bl}^2}{R}. \quad (2.3.39)$$

The renormalized free energy of the polymer under cylindrical confinement produces the correct equilibrium length as well as free energy at equilibrium which scales as the number of blobs $\beta\mathcal{F}(L_{eq}, N, D) \sim N(a/D)^{5/3} \sim N/g$. The force of polymer compression and stretching in a cylinder derived from the “renormalized” free energy also scales properly that has been confirmed by computer simulations [41, 61]. Moreover, the work [41] suggests that eq. (2.3.39) is applicable for free energy calculation not only in equilibrium, but also for rather stretched and compressed polymers, where the polymer extension R along the cylinder is in the range $0.5 < R/L_{eq} < 1.2$ [5].

2.3.5 Polymers between two parallel plates

In section 2.3.2 we mentioned that the size of a self-avoiding polymer trapped a narrow infinitely long slit scales like $N^{3/4}$, where N is the number of monomers composing the polymer (see eq. (2.3.22) for two-dimensional case). However, the size of such a polymer also depends on the width H of the slit. To find the scaling of the polymer size with H we revisit the Flory approach for two dimensional case.

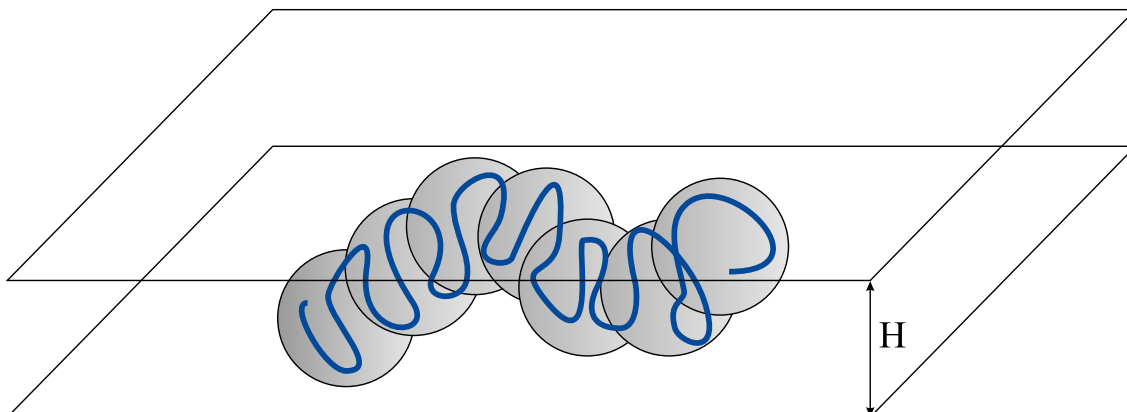


Figure 2.11: A self-avoiding polymer trapped in a slit of width H . The polymer is split into a sequence of blobs of size H .

Let us assume that the slit is so narrow that $H \ll R_g$, where R_g is the radius of gyration of an unconfined polymer, and the polymer confined in the slit expands to the size R_{\parallel} . Then the width H determines the size of the compression blobs (see Fig. 2.11) with the excluded area H^2 , and the polymer splits into a sequence of N/g blobs, where $g = (H/a)^{5/3}$ is the number of monomers of size a per blob according to eq. (2.3.28). The probability of one blob to be excluded from the area occupied by another blob is $H^2(N/g)/R_{\parallel}^2$, where R_{\parallel}^2 is the area occupied by the polymer. Then the free energy of excluded volume interactions of a polymer composed of N/g compression blobs can be written as $k_B T H^2 (N/g)^2 / R_{\parallel}^2$. The free energy spent to extend an ideal chain composed of $n_{bl} = N/g$ blobs to the length R_{\parallel} is $k_B T R_{\parallel}^2 / (N/g) H^2$. The sum of these two contributions gives the Flory free energy of a polymer confined in a slit of width H :

$$\beta \mathcal{F}(N, H) \sim H^2 \frac{(N/g)^2}{R_{\parallel}^2} + \frac{R_{\parallel}^2}{(N/g) H^2}, \quad (2.3.40)$$

where $\beta = 1/k_B T$. Minimizing the free energy with respect to R_{\parallel} we obtain the size of the polymer in equilibrium:

$$R_{\parallel} \sim H \left(\frac{N}{g} \right)^{3/4} \sim N^{3/4} a^{5/4} H^{-1/4}, \quad (2.3.41)$$

which is in good agreement with the size of polymers computed in simulations [62]. Note, although the Flory approach gives the correct scaling of the polymer size in a slit, the free energy of the polymer estimated using this approach is $\beta \mathcal{F} \sim \sqrt{n_{bl}}$ that contradicts to the de Gennes model, where the free energy scales linearly with the number of blobs.

2.4 Molecular dynamics simulations

To answer the questions posed in the Introduction (Chapter 1) we perform Molecular Dynamics simulations (MD). Molecular dynamics simulations have become a popular and powerful technique to study different systems on the coarse-grained level. They enable us to understand equilibrium properties of a system and its dynamics on scales where the motion of particles can be tracked. The main idea of MD is to solve Newton's equations of motion to observe the evolution of the system with time. Data obtained from MD simulations allow us to confirm theoretical predictions and make new predictions where theory is restricted by its initial assumptions or the range of its validity. In this section, we discuss the general principles of MD simulations which are summarized from text books by D. Frenkel and B. Smit [43] and M. P. Allen and D. J. Tildesley [63].

2.4.1 Force calculation

For a system composed of N particles interacting via potential U one can obtain trajectories for the particles over time by calculating the force as follows. First of all one needs to initialize a system giving each particle its position \mathbf{x}_i and velocity \mathbf{v}_i , $i = 0, \dots, N$. Next, using potentials calculate a force \mathbf{f}_i acting on the i -th particle:

$$\mathbf{f}_i = - \sum_{j \neq i} \nabla U(r_{ij}), \quad (2.4.1)$$

where $r_{ij} = |\mathbf{r}_i - \mathbf{r}_j|$ is the distance between particles i and j . If an additional external force is applied then it should be added to the interparticle force given by eq. (2.4.1) separately. Force calculations are the most time consuming step in MD simulations, since we must calculate $N(N - 1)/2$ distances between particles and the corresponding potentials. However, Verlet lists [64] and cell lists, which will be discussed later in the section, are usually used to optimize the force computations.

2.4.2 Numerical integrator

After the force calculation, we update particle positions and velocities at time $t + \delta t$ by integrating Newton's equations of motion $m\ddot{\mathbf{x}}_i = \mathbf{f}_i$ numerically, where m is the mass of a particle. Many numerical schemes exist for solving this task, among them the Euler algorithm, the Leap-Frog, Verlet-like scheme. However, an algorithm has to provide good accuracy for large time steps δt , conserve energy and be time reversible to trace back particle trajectories. One of the frequently used algorithms satisfying all three requirements is the so-called velocity Verlet algorithm [43]. The scheme of this algorithm is represented as follows:

$$x(t + \delta t) = x(t) + v(t)\delta t + \frac{f(t)}{2m}\delta t^2, \quad (2.4.2)$$

$$v(t + \delta t) = v(t) + \frac{f(t + \delta t) + f(t)}{2m}\delta t. \quad (2.4.3)$$

According to this scheme, one first computes the new particle positions. Then, using the updated particle positions, one computes new forces and new velocities.

2.4.3 Thermostat

To carry out MD simulations in the canonical ensemble we employ a thermostat which allows us to keep the temperature T constant. By mean of the thermostat we ensure that the temperature of the system fluctuates around a desired value. The most common thermostat used in coarse-grained MD simulations is the Langevin thermostat. Here, particles in the system are assumed to be embedded in a bath of fictional particles of smaller size. In this case, the dynamics of the particles is described by Langevin equations of motion:

$$m\ddot{x} = -m\gamma\dot{x} + f + \xi(t). \quad (2.4.4)$$

The first term in this equation is the friction force created by the bath with friction coefficient γ . The force f is a force induced by particle interactions and an external forces if it is applied to the system. The last term in eq. (2.4.4) is the Gaussian random force with the first two moments $\langle \xi(t) \rangle = 0$ and $\langle \xi(t)\xi(t') \rangle = 2\gamma k_B T \delta(t-t')$. The latter represents the thermal fluctuations from the heat bath. The first and last terms are coupled by the fluctuation-dissipation theorem [65] and allow one to recover the canonical ensemble.

2.4.4 Optimization

Most of the time in computer simulations is spent for computing forces acting on the particles, since it requires to consider all possible pairs of particles, evaluate the distance between them and calculate corresponding potentials. For a system composed of N particles interacting via an additive two-body potential, the number of all possible pairs of particles is $N(N-1)/2$. Thus, the time of the force calculation scales like N^2 . Moreover, if the particle interactions are short-range, then most of the pairs do not contribute to the force, but we still compute their interactions, waisting the computational time. Verlet developed a technique called the Verlet list [64] which allows us to avoid this inefficiency. In this technique, for each particle of the system one creates a list of its neighbors in its vicinity. The vicinity is determined by the radius r_v which should be larger than the cutoff radius r_c of the

short-range interactions. Thus, the list of particle i contains all the particles whose interactions with the reference particle are non-zero and contribute to the force. The computation of interactions between the reference particle and the particles from the list reduces the computational time which becomes of order N . The difference between the radiuses $r_v - r_c$ is the distance which the particles from the list can move without a need to update the lists. Once a particle from the list moves out more than this distance, the Verlet lists have to be updated.

However, the update of the Verlet lists is still of order N^2 . This can be circumvented using the cell list or linked-cell method. This method divides the simulation box into cells whose size is equal or larger than r_v . Then, the particles with nonzero interactions are located within one cell or in the neighboring cells. The construction of the Verlet lists using only these particles decreases the computational time which in this case scales linearly with N .

2.5 Coarse-grained simulation model of polymers

Polymers are large macromolecules composed of many repeated units, which are linked by covalent chemical bonds. Polymer structure displays universal behavior of polymers on the length scale larger than one Kuhn length a , where local chemical structures of polymers are no longer important. Therefore, a polymer can be considered as a sequence of monomers of size a . This allows us to construct a simplified coarse-grained model for studying polymers. In this thesis, we use a bead-spring model [66], since this model covers two main features of a self-avoiding polymer, namely connectivity of monomers by bonded interactions and excluded-volume between monomers.

The excluded volume of spherical monomers of diameter σ is usually modeled by a potential which is strongly repulsive at short distances between the monomers. The typical choice of the potential for Monte-Carlo simulations is the hard-sphere potential [46]

$$U_{HS}(r) = k_B T \begin{cases} \infty & r < a \\ 0 & r \geq a \end{cases} \quad (2.5.1)$$

due to its simplicity. Here, r is the distance between the centers of two monomers. In this thesis, we use the Weeks-Chandler-Andersen (WCA) potential [67]

$$U_{WCA}(r) = k_B T \begin{cases} \left(\frac{a}{r}\right)^{12} - \left(\frac{a}{r}\right)^6 + \frac{1}{4} & r < \sqrt[6]{2}a \\ 0 & r \geq \sqrt[6]{2}a, \end{cases} \quad (2.5.2)$$

which is the Lennard-Jones potential [46], but shifted up by the depth of its well and truncated at $r = \sqrt[6]{2}a$. This makes the WCA potential purely repulsive, but the repulsion is slightly softer than the one between two hard spheres.

To create a polymer chain we link monomers by springs inserting finitely extensible nonlinear elastic (FENE) bonds between consecutive monomers. The FENE potential [66] is used to this aim:

$$U_{FENE}(r) = -\frac{kr_F^2}{2} \ln \left[1 - \left(\frac{r}{r_F} \right)^2 \right], \quad (2.5.3)$$

where r_F is the maximal stretch of the bonds and k is the spring constant. The FENE potential guarantees that bonds can not be infinitely stretched. This determines the advantage of the FENE potential over the standard harmonic potential.

We perform molecular dynamics simulations of polymers under cylindrical confinement using the simulation package ESPResSo [68] which has been developed for investigating Soft-Matter systems on the coarse-grained level. The cylinder is modeled using the feature `constraint cylinder`. The constraint is identified like a particle via non-bonded interaction, where the distance between two particles is replaced by the distance between a monomer center and the surface of the cylinder. Polymers should not penetrate the cylinder, therefore the cylindrical surface has to be repulsive. In this case, it is convenient to use the same WCA potential (2.5.2) to describe interactions between the monomers of the polymer and the cylinder.

2.6 Reaction-rate theory or Kramers' theory

The reaction-rate theory plays an important role for understanding many physical, chemical and biological processes with different metastable states. The common problem which arises during studying such systems is the problem related to the escape from a metastable state, since the escape occurs rarely on a time scale which is significantly longer than the time scales of the local stability.

The first successful attempt to estimate the rate of escape or reaction rate was done by Arrhenius in his fundamental work from 1889 [69]. Arrhenius proposed the central idea of the transition state theory for chemical reactions, which states that a transition state exists and is intermediate between a reactant and product. The activation energy of a chemical process is linked to the free energy barrier which has to be overcome by the reactant in order for the reaction to occur. With this postulate he developed a law for the rate of escape k which exponentially depends on temperature. This law was later named after him and has the following form

$$k = \nu \exp(-\beta E_b), \quad (2.6.1)$$

where E_b denotes the activation energy and ν is a prefactor. Later it was shown that the activation energy is the height of the free energy barrier in the potential of the mean force of the reacting system. Although the transition state theory is

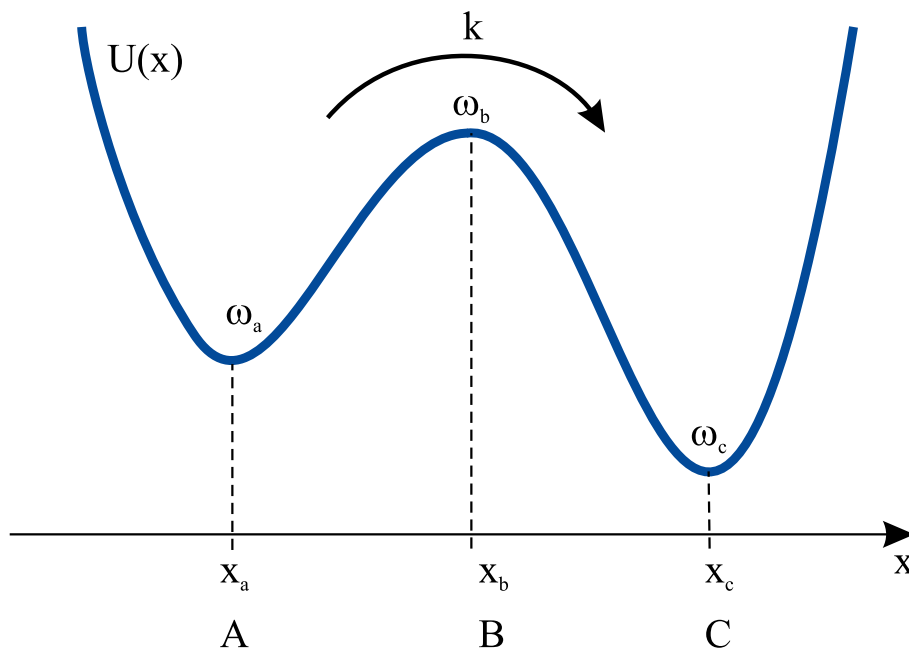


Figure 2.12: Double-well potential $U(x)$ with two metastable states A and C . Escape from the state A to the state B occurs with the rate k . The system has to overcome the free energy barrier E_b at the state B .

consistent with the thermodynamical theory, it does not consider the dynamics of the process, therefore, the transition state theory is unable to predict the quantity ν . This gap was filled by Kramers, who in 1940 elucidated the mechanism of the escape process. He derived the reaction rate precisely, suggesting that the escape process is governed by the dynamics of Brownian motion driven by thermal forces [70]. Below we provide a brief overview of Kramers' theory which is based on his work [70] and the review of the reaction-rate theory [71].

Let us consider the double-well potential $U(x)$ shown in Fig. 2.12 which has two minima at x_a and x_c . These minima correspond to the metastable states A and C and are separated by an energetic barrier at x_b called transition state B . If a particle of mass $m = 1$ moving along the reaction coordinate x with the potential $U(x)$ at the constant temperature T , its motion is described by Langevin dynamics

$$\ddot{x} = -U'(x) - \gamma\dot{x} + \xi(t), \quad (2.6.2)$$

where the first term is the force acting on the particle and determined as a derivative of the potential $U(x)$ with respect to the time t , the second term is the friction force with friction constant γ . The fluctuating force $\xi(t)$ is Gaussian noise which obeys the fluctuation dissipation theorem:

$$\langle \xi(t) \rangle = 0 \quad (2.6.3)$$

$$\langle \xi(t)\xi(t') \rangle = 2\gamma k_B T \delta(t - t'). \quad (2.6.4)$$

The stochastic dynamics of a brownian particle along the reaction coordinate x is determined by the time evolution of the probability density $p(x, v, t)$ of the particle in phase space, where $v = \dot{x}$ is the particle velocity. Therefore, one can employ the Fokker-Planck equation to describe the evolution of $p(x, v, t)$ in the phase space. The Fokker-Planck equation for Langevin dynamics has the following form

$$\frac{\partial p(x, v, t)}{\partial t} = \left[-\frac{\partial}{\partial x} v + \frac{\partial}{\partial v} (U'(x) + \gamma v) + \gamma k_B T \frac{\partial^2}{\partial v^2} \right] p(x, v, t). \quad (2.6.5)$$

Here, the first two terms are the drift of the particle in phase space and the third one is called the diffusion term. Eq. (2.6.5) provides a complete description of the process defined by eq. (2.6.2)-(2.6.4) and has the following stationary solution

$$p(x, v) = Z^{-1} \exp \left[- \left(\frac{v^2}{2k_B T} + \frac{U(x)}{k_B T} \right) \right], \quad (2.6.6)$$

where Z is the partition function.

The state A can be identified with the source which supplies the system with particles whose energies are less than the energy at the barrier top. These particles has to be thermalized before they can eventually leave the state A in order to cross the barrier B . Assume that beyond the barrier the particles are removed by a sink, so that they will never return to the state A . Then the rate of escape from the state A to the state C is determined by the probability to cross the barrier B , which is equal to the particle flux j passing the barrier over the particle population n_a at the state A

$$k = \frac{j}{n_a}, \quad (2.6.7)$$

where the current and the population are defined via the probability density $p(x, v)$ as follows

$$j = \int_{-\infty}^{+\infty} v p(x, v) dv \quad (2.6.8)$$

and

$$n_a = \int_{\text{near } A} p(x, v) dx dv. \quad (2.6.9)$$

The probability density $p(x, v)$ can be found from the Fokker-Planck equation (2.6.5), which for the stationary state at the top of the barrier is

$$\left[-\frac{\partial}{\partial x} v - \frac{\partial}{\partial v} [\omega_b^2(x - x_b) - \gamma v] + \gamma k_B T \frac{\partial^2}{\partial v^2} \right] p(x, v) = 0, \quad x \approx x_b. \quad (2.6.10)$$

Here, due to the parabolic form of the potential $U(x)$ near the state B we assume that the potential $U(x)$ can be expressed as an oscillatory harmonic potential

$$U(x) = U(x_b) - \frac{1}{2} \omega_b^2 (x - x_b)^2, \quad x \approx x_b, \quad (2.6.11)$$

where $\omega_b = -U(x)''$ is the angular frequency at the top of the barrier.

Under this assumption Kramers solved eq. (2.6.10) and found the stationary probability density $p(x, v)$. This allowed him to estimate the flux of particles passing the barrier B :

$$j = Z^{-1} \exp(-\beta U(x_b)) \sqrt{\frac{2\pi\gamma k_B T}{a}}, \quad (2.6.12)$$

where a is the parameter which depends on the friction γ and angular frequency ω_b as follows

$$a = \frac{\gamma}{2} + \sqrt{\frac{\gamma^2}{4} + \omega_b^2}. \quad (2.6.13)$$

The population of particles n_a at the state A was obtained in the same manner as the flux j . The oscillatory harmonic potential in the vicinity of x_a changes to the potential $U(x) = U(x_a) + \omega_a^2(x - x_a)^2/2$ with the equilibrium point at $x = x_a$ and angular frequency ω_a . Then, the integration of the stationary probability density according eq. (2.6.9) leads to the following form of the population of particles n_a :

$$n_a = Z^{-1} \frac{k_B T}{\omega_a} \exp(-\beta U(x_a)) \sqrt{\frac{2\pi\gamma k_B T}{a - \gamma}}. \quad (2.6.14)$$

Combining equations (2.6.12), (2.6.14) and (2.6.7) we obtain Kramers' fundamental result for the reaction rate of escape k from the state A to the state C over the free energy barrier $U(x_b) - U(x_a)$:

$$k = \frac{\omega_a}{2\pi\omega_b} \left(\sqrt{\frac{\gamma^2}{4} + \omega_b^2} - \frac{\gamma}{2} \right) \exp[-\beta(U(x_b) - U(x_a))]. \quad (2.6.15)$$

It is worth mentioning, this expression for the reaction rate k is valid for systems with moderate or strong friction γ , where the reaction process is governed by spatial diffusion. In the limit of strong friction the reaction rate can be immediately obtained from eq. (2.6.15) assuming that $\gamma \gg \omega_b$:

$$k = \frac{\omega_a \omega_b}{2\pi\gamma} \exp[-\beta(U(x_b) - U(x_a))]. \quad (2.6.16)$$

Knowing the reaction rate, one can also determine the mean first passage time t_{MFPT} when the reaction process occurs. For every stochastic process in the state space the mean first passage time is defined as the average time spent for waiting when the process starting from a specific point leaves the spatial domain for the first time. In this case, the starting point is x_a and the boundary of the spatial domain is the position of the sink which is placed in between the barrier top and the product state C at x_c . Since transition from the reactant to the product is characterized by the reaction rate k , the mean first passage time is expressed via this rate as follows

$$t_{MFPT} = k^{-1}. \quad (2.6.17)$$

Kramers' theory made invaluable contribution to solving various problems related to polymers. For example, investigating polymer translocation into a confined region, which is ubiquitous in biology and nanotechnology, the translocation time of polymers can be determined by means of the mean first passage time [72]. Furthermore, equation (2.6.17) gives a straightforward estimate of the time which a semiflexible polymer needs to form a loop [73]. Understanding loop formation dynamics is extremely important in biology for protein folding and it also may trigger the initiation DNA replication process [74]. As will be shown in Chapter 3 and 4, Kramers' theory has been successfully applied to compute the induction time of polymers trapped in a cylinder.

Note that in order to find the mean first passage time of a reaction not only the free energy barrier has to be known, but also the angular frequencies at the top and bottom of the barrier, which are determined by the curvatures of the free energy landscape at these points. In the next section, we discuss methods to calculate the free energy for cases where the free energy barrier is significantly larger than $k_B T$.

2.7 Free energy calculations

Studying the behavior of polymers under cylindrical confinement we encounter several problems related to free energy barriers which have to be overcome. There exists many methods which allow us to estimate free energy barriers. In particular, Umbrella Sampling [75], Forward Flux Sampling [76], Method of Widom Insertions [77] and Metadynamics [78]. In this section, we discuss three methods which are used in this thesis for computing free energy barriers.

2.7.1 Potential of mean force

The simplest method to compute the free energy difference is to run conventional molecular dynamics simulations for a sufficiently long time. If the free energy barrier is not very high, the system visits all points in the phase space overcoming the free energy barriers frequently enough to provide good statistics for every state of the system. Then, we can find difference in the free energy for different states of the system by measuring how frequently the system visits them. According to classical statistical mechanics the free energy of a system \mathcal{F} in the canonical ensemble, where temperature T , number of particles N and volume of the system V are constant, is expressed via the partition function Z as follows

$$\mathcal{F} = -k_B T \ln Z. \quad (2.7.1)$$

The partition function contains all the information about macroscopic states of the system, and for two polymers composed of equal number of monomers N and can be written as

$$Z = \int \int \exp(-\beta\mathcal{H}) d\mathbf{r}^{2N} d\mathbf{p}^{2N}, \quad (2.7.2)$$

where $\{\mathbf{r}^{2N}\}$ and $\{\mathbf{p}^{2N}\}$ are the phase coordinates and momenta of all monomers of the two polymers respectively. One can split the Hamiltonian of the system \mathcal{H} into three contributions

$$\mathcal{H} = \mathcal{H}_{11} + \mathcal{H}_{22} + \mathcal{H}_{12}, \quad (2.7.3)$$

Here, \mathcal{H}_{ii} represents intrapolymer interactions where $i = 1, 2$ and the part \mathcal{H}_{ij} , where $i \neq j$, involves all inter polymer interactions. The potential energy of polymers is independent of monomer momenta, thus the integration over all momenta $\{\mathbf{p}^{2N}\}$ in eq. (2.7.2) gives us a constant which can be ignored. Then, the partition function has the following form

$$Z = \int \exp(-\beta\mathcal{H}) d\mathbf{r}^{2N}. \quad (2.7.4)$$

Instead of considering all the monomer positions, it is convenient to introduce another coordinate which also describes the thermodynamic state of the polymers and is called the reaction coordinate. For example, the distance between the centers of polymer mass or distance between the furthest monomers can be chosen as the reaction coordinate. Let us denote this reaction coordinate as q . Then the probability distribution $P(q)$ of the system along q is given by the Boltzmann distribution integrated over all degrees of freedom apart q :

$$P(q) = \frac{\int \delta[q(\mathbf{r}) - q] \exp(-\beta\mathcal{H}) d\mathbf{r}^{2N}}{\int \exp(-\beta\mathcal{H}) d\mathbf{r}^{2N}}. \quad (2.7.5)$$

Here, $\delta[q(\mathbf{r}) - q]$ denotes the Dirac delta function for the coordinate q . The free energy of the system at the state q can be calculated using this probability distribution as

$$\beta\mathcal{F}(q) = -\ln P(q), \quad (2.7.6)$$

where $\mathcal{F}(q)$ is also called the potential of mean force [79]. The probability distribution $P(q)$ can be obtained directly from computer simulations as the time average

$$P(q) = \lim_{t \rightarrow \infty} \frac{1}{t} \int_0^t \rho[q(t')] dt' \quad (2.7.7)$$

for ergodic systems, where every point of the phase space is visited during simulations, since for ergodic systems the time average is equivalent to the ensemble average. Here, ρ is the number of occurrences of q in a given interval which is a finite width for calculating histograms. In this way, the free energy can be calculated directly from molecular dynamics simulations by monitoring the probability distribution of the system along the reaction coordinate.

2.7.2 Forward Flux Sampling

It is not always possible to sample all the phase space during conventional simulations which run for a finite time. If the free energy barrier is significantly higher than $k_B T$, the phase space at that region is visited very rarely. Therefore, an advance sampling method has to be employed to obtain the free energy of rare events. In this section, one such method called the Forward Flux Sampling (FFS) [76, 80, 81, 82] is discussed. This method is used in this thesis to compute the free energy landscape of systems with high free energy.

To introduce the method, let us consider a transition of a system from a state A to a state B . To perform this transition the system has to overcome a free energy barrier. The states here are determined in terms of an order parameter $\lambda(r)$, where r denotes coordinates in phase space. The key idea of the FFS method is to divide the region between A and B into a series of $n + 1$ interfaces λ_i placed in the following way $A = \lambda_0 < \lambda_1 < \dots < \lambda_{n-1} < \lambda_n = B$ as shown in Fig. 2.13. First of all, one performs conventional molecular dynamics simulations starting from the initial state A . During these simulations the trajectory crosses the border of state A , which corresponds to the interface λ_0 , relatively frequently. When the trajectory crosses the interface λ_0 in the direction of the final state B , the configuration of the system

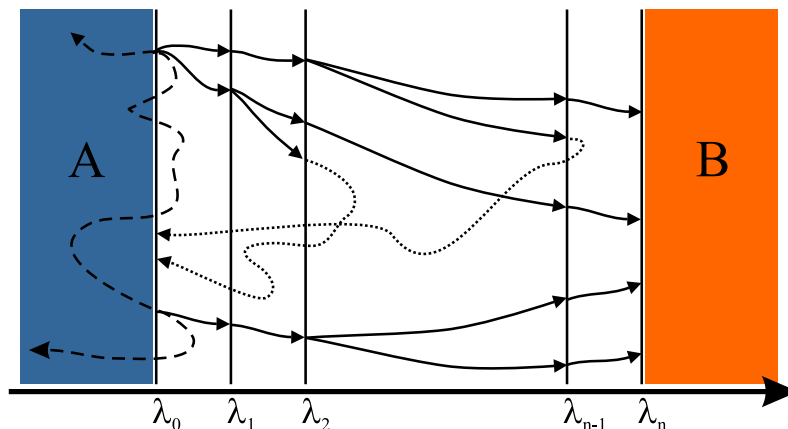


Figure 2.13: Schematic illustration of the Forward Flux Sampling Method. The free energy barrier is located in between the initial state A and the final state B . A sequence of interfaces is placed in the region between these two states. Dashed lines represent initial trajectories, which determine the escape flux. Solid lines show successful trajectories, which reached the state B , and dotted lines show unsuccessful trajectories, which returned to the state A .

is stored. At the end of this simulation, one calculates the escape flux Φ_A , which is a flux of trajectories leaving the initial state A . The collected configurations at the interface λ_0 are used as the starting points of a set of trajectories to explore the next interface λ_1 . Starting next simulations from these configurations, the trajectories can either reach the interface λ_1 or return to the interface λ_0 . In the first case, we again store configurations for exploring the next interface. This procedure is repeated until the final state B is reached. During runs from interface to interface, one can estimate the probability $P(\lambda_{i+1}|\lambda_i)$ that a trajectory coming from the interface λ_i reaches the next interface λ_{i+1} without returning to the border A . Then, the transition rate k_{AB} from the state A to the state B can be obtained from the following equation [83]

$$k_{AB} = \Phi_A \prod_{i=0}^{n-1} P(\lambda_{i+1}|\lambda_i). \quad (2.7.8)$$

Tracing the successful trajectories, which reached the final state B starting from state A , we reproduce the transition paths for the rare events of the transition from the state A to B . In order to obtain a complete sampling in the desired region, in addition to the FFS run from A to B , one needs to reproduce the transition backwards from B to A performing FFS in the reverse direction. To distinguish quantities obtained from forward and backward FFS runs we mark them according to the initial state, so that the subscript A is used to denote the forward runs, whereas the subscript B denotes the backward runs.

In order to calculate the free energy landscape in the region between the states

A and B , one needs to compute stationary probability distributions $\rho(q)$. Note that the order parameter q has to be the same as the order parameter λ . The total probability distribution $\rho(q)$ can be written as a sum of two contributions of forward and backward FFS runs:

$$\rho(q) = \Psi_A(q) + \Psi_B(q), \quad (2.7.9)$$

where Ψ_A and Ψ_B are the contributions of trajectories coming from state A and B , respectively. Here, we take into account all trajectories generated by FFS including those which have returned to the initial state. The functions Ψ_A and Ψ_B are given by

$$\Psi_A = p_A \Phi_{A\tau_A}(q, \lambda_0), \quad (2.7.10)$$

$$\Psi_B = p_B \Phi_{B\tau_B}(q, \lambda_n). \quad (2.7.11)$$

Each of these probabilities consists of a product of three quantities: the probability of the system to be in the initial state A or B , denoted as p_A and p_B respectively, the corresponding initial fluxes of trajectories leaving the initial states Φ_A and Φ_B , and the average time spent by all generated trajectories at the order parameter q which are represented as $\tau_A(q, \lambda_0)$ and $\tau_B(q, \lambda_n)$.

The probabilities p_A and p_B can be found with the help of transition rates k_{AB} and k_{BA} which are computed during FFS runs in both directions according to eq. (2.7.8). Note that in the steady state:

$$k_{AB}p_A = k_{BA}p_B. \quad (2.7.12)$$

The sum of these probabilities is around unity, since the probability of finding the system in the region between A and B is close to zero due to the high free energy barrier in this region. These two conditions lead to

$$p_A = \frac{k_{BA}}{k_{AB} + k_{BA}}, \quad (2.7.13)$$

$$p_B = \frac{k_{AB}}{k_{AB} + k_{BA}}. \quad (2.7.14)$$

The initial flux of trajectories is obtained from the FFS directly as described above. Therefore, we are left with the calculation of average times $\tau_A(q, \lambda_0)$ and $\tau_B(q, \lambda_n)$. In the FFS, we generate a set of interfaces $\{\lambda_i\}$, $i = 0, 1, 2, \dots, n$, then monitoring the trajectories coming from each interface λ_i ($i = 0, 1, \dots, n - 1$ in the forward direction and $i = n, n - 1, \dots, 1$ in the reverse direction) we can compute the distribution function $\pi_A(q, \lambda_i)$ averaged over all trajectories coming from the

interface λ_i . This can be done using the histogram method. The total distribution function $\tau_A(q, \lambda_0)$ is just the sum of all the distribution functions $\pi_A(q, \lambda_i)$

$$\tau_A(q, \lambda_0) = \sum_{i=0}^{n-1} \pi_A(q, \lambda_i). \quad (2.7.15)$$

This expression for $\tau_A(q, \lambda_0)$ does not take into account the fact that not every trajectory coming from the previous interfaces λ_j ($j = 0, 1, \dots, i-1$) has reached the current interface λ_i . In other words, not every trajectory is used for constructing transition path from the initial interface to the current one and, as a consequence, to the final interface. To improve eq. (2.7.15), each distribution function $\pi_i(q)$ has to be weighted by the probability $P(\lambda_i|\lambda_0)$ of reaching the interface λ_i from the initial interface λ_0 . This probability $P(\lambda_i|\lambda_0)$ is a conditional probability that a trajectory has arrived at every previous interface before reaching λ_i and is given by

$$P(\lambda_i|\lambda_0) = \prod_{j=0}^{i-1} P(\lambda_{j+1}|\lambda_j). \quad (2.7.16)$$

Thus, the final expression for $\tau_A(q, \lambda_0)$ is written as follows

$$\tau_A(q, \lambda_0) = \pi_A(q, \lambda_0) + \sum_{i=1}^{n-1} \pi_A(q, \lambda_i) \prod_{j=0}^{i-1} P(\lambda_{j+1}|\lambda_j). \quad (2.7.17)$$

The expression for $\tau_B(q, \lambda_n)$ can be derived similarly, so that

$$\tau_B(q, \lambda_n) = \pi_B(q, \lambda_n) + \sum_{i=n-1}^1 \pi_B(q, \lambda_i) \prod_{j=n}^{i+1} P(\lambda_{j-1}|\lambda_j). \quad (2.7.18)$$

Substituting eq. (2.7.13), (2.7.14), (2.7.17) and (2.7.18) into eq. (2.7.9) we obtain the total normalized probability distribution $\rho(q)$ which allows us to compute the free energy

$$\Delta\beta\mathcal{F}(q) = -\ln(\rho(q)). \quad (2.7.19)$$

Note that if the system is symmetric, so that $p_A = p_B$, meaning that the free energy landscape has a symmetric shape as shown in Fig. 2.14, it is sufficient to perform FFS only in the forward direction. The probability distribution $\tau_B(q, \lambda_n)$ can be obtained from $\tau_A(q, \lambda_0)$ by simple coordinate inversion.

To run the FFS simulations we used the software package Flexible Rare Event Sampling Harness System (FRESHS) [84, 85] where all the basics of this sampling algorithm are implemented. FRESHS is based on a harness system using a server-client scheme which allows us to separate the framework of the FFS algorithm from

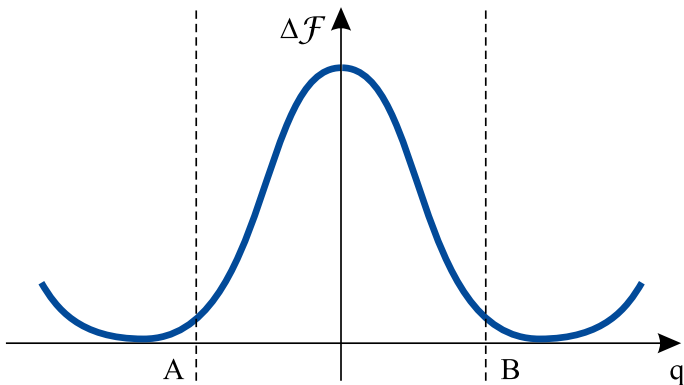


Figure 2.14: Symmetric free energy landscape $\Delta\mathcal{F}$ as a function of reaction coordinate q .

the physical details of the system under investigation. To run simulations, one needs to write a harness script which is executable in ESPResSo and contains all the information about the particles, their interactions and constraints. This script is attached to the client level. Running several clients, one can generate several trajectories simultaneously. Clients communicate to the server which governs the sampling entirely. FRESHS uses an automatic optimized interface placement algorithm that ensures optimal flux through the interfaces and enhance the computational efficiency [85]. The interface placement, storage of the configuration points on the interfaces to a database, as well as the analysis of the database for calculating all the required probabilities and reaction rates are done on the server level.

2.7.3 Widom’s insertion method

The method of Widom insertion is typically used to calculate the effective potentials of complex soft-matter particles or macromolecules such as flexible linear and ring polymers, polymer-coated colloids or dendrimers, in the zero-density limit where the many-body interactions are neglected. The effective potential allows us to describe the behavior of a system composed of such complex particles. To characterize the position of a single complex particle it is convenient to use a single effective coordinate. The geometric center of the particle or the center of mass are usually chosen for this purpose. Each complex particle or polymer is mapped to a single soft-sphere, and the effective potential determines how strong these spheres interact depending on the distance between them.

Originally, the method of Widom insertion was developed for calculating chemical potentials of non-uniform fluids [86]. However, Widom’s approach was adapted to calculate effective interactions between mesoscopic particles in the zero-density limit by Mladek and Frenkel [77], whose derivation we follow below.

Let us consider a system of N complex particles confined in a volume V at a constant temperature T . According to the coarse-graining of the system, each particle i has an effective coordinate denoted by the vector \mathbf{R}_i . The potential energy of the system including all inter- and intra-particle interactions can be written as $U(\mathbf{R}_1, \dots, \mathbf{R}_N)$. Then, the density profile $\rho(\mathbf{r})$ at a position \mathbf{r} is [46]

$$\rho(\mathbf{r}) = \frac{N}{Z_N} \int d\mathbf{R}_1 \dots d\mathbf{R}_{N-1} e^{-\beta U(\mathbf{R}_1, \dots, \mathbf{R}_{N-1}, \mathbf{r})}, \quad (2.7.20)$$

where Z_N is the configurational integral

$$Z_N = \int d\mathbf{R}_1 \dots d\mathbf{R}_N e^{-\beta U(\mathbf{R}_1, \dots, \mathbf{R}_{N-1}, \mathbf{R}_N)}. \quad (2.7.21)$$

The exponent in the density profile can be split into the exponent of the potential energy of $N - 1$ particles and the exponent of the energy change ΔU due to adding the N -th particle at the position \mathbf{r} . This leads to

$$\rho(\mathbf{r}) = \frac{N}{Z_N} \int d\mathbf{R}_1 \dots d\mathbf{R}_{N-1} e^{-\beta U(\mathbf{R}_1, \dots, \mathbf{R}_{N-1})} e^{-\beta \Delta U(\mathbf{R}_1, \dots, \mathbf{R}_{N-1}, \mathbf{r})}. \quad (2.7.22)$$

Using the definition of the ensemble average for $N - 1$ particles the previous equation converges to

$$\rho(\mathbf{r}) = \frac{N Z_{N-1}}{Z_N} \langle e^{-\beta \Delta U(\mathbf{R}_1, \dots, \mathbf{R}_{N-1}, \mathbf{r})} \rangle_{N-1, \mathbf{r}}, \quad (2.7.23)$$

where $\langle \dots \rangle_{N-1, \mathbf{r}}$ denotes the ensemble average of the $N - 1$ particle system at the position \mathbf{r} from the N -th particle. If we consider only two particles with the effective coordinates \mathbf{R}_1 and $\mathbf{r} = \mathbf{R}_2$ the above equation reduces to the following

$$\rho(\mathbf{R}_2) = \frac{N Z_1}{Z_2} \langle e^{-\beta \Delta U(\mathbf{R}_1, \mathbf{R}_2)} \rangle_{N=1, \mathbf{R}_2}. \quad (2.7.24)$$

Now we link the origin of the coordinate system with the position of the first particle \mathbf{R}_1 . Then the second particle is placed at the distance $R_{12} = |\mathbf{R}_2 - \mathbf{R}_1| = |\mathbf{R}_2|$. The density profile $\rho(R_{12})$ of such system can be expressed via the radial distribution function $g(R_{12})$ as $\rho(R_{12}) = \rho g(R_{12})$, where $\rho = N/V$ is the number density. Thus leads to the following form of eq. (2.7.24)

$$\rho g(R_{12}) = \frac{N Z_1}{Z_2} \langle e^{-\beta \Delta U(R_{12})} \rangle_{N=1, R_{12}}. \quad (2.7.25)$$

Since the considered system is in the zero-density limit, the radial distribution function is simply the Boltzmann factor of the effective pair potential $\beta V_{eff}(R_{12})$: $g(R_{12}) = \exp(-\beta V_{eff}(R_{12}))$ [46]. Substituting this argument into the equation above we find that

$$\beta V_{eff}(R_{12}) = -\ln [\langle e^{-\beta \Delta U(R_{12})} \rangle_{N=1, R_{12}}] + C, \quad (2.7.26)$$

where C is a constant which is proportional to the configurational integral of the system and determined by interactions between the particles at the infinite distance $R_{12} \rightarrow \infty$. Thus, we can write that C is

$$C = \ln [\langle e^{-\beta \Delta U(R_{12})} \rangle_{N=1, R_{12} \rightarrow \infty}]. \quad (2.7.27)$$

Note, the effective potential is directly linked to the free energy difference between two states. Namely, when the complex particles are separated by a finite distance R_{12} and when they are infinitely separated ($R_{12} \rightarrow \infty$), so that they do not interact with each other anymore:

$$V_{eff}(R_{12}) = F(R_{12}) - F(R_{12} \rightarrow \infty). \quad (2.7.28)$$

Using this definition one can show that the effective potential is a function of the expectation value of interparticle interactions as eq. (2.7.26) states. Without loss of generality, we demonstrate the latter for two polymers, each consisting of N monomers. If $\{\mathbf{r}^{iN}\}$ denote coordinates of monomers which belong to the i -th polymer ($i = 1, 2$), the partition function for an arbitrary distance between the polymers R_{12} is

$$Z(R_{12}) = \int \int d\mathbf{r}^{1N} d\mathbf{r}^{2N} e^{-\beta[U_{11}(R_{12}) + \Delta U(R_{12}) + U_{22}(R_{12})]}, \quad (2.7.29)$$

where the Hamiltonian of the system is written as a sum of three parts representing intra- $U_{11}(R_{12}) + U_{22}(R_{12})$ and inter- $\Delta U(R_{12})$ particle interactions. Since the free energy is a logarithmic function of the partition function, the exponent of the effective potential at a distance R_{12} can be written in the form

$$e^{-\beta V_{eff}(R_{12})} = \frac{Z(R_{12})}{Z(R_{12} \rightarrow \infty)}. \quad (2.7.30)$$

However, when the particles are infinitely far apart $R_{12} \rightarrow \infty$, the interparticle contribution vanishes making the intraparticle contribution independent of the polymer separation. This reduces the previous expression to

$$e^{-\beta V_{eff}(R_{12})} = \frac{\int \int d\mathbf{r}^{1N} d\mathbf{r}^{2N} e^{-\beta[U_{11} + \Delta U(R_{12}) + U_{22}]} }{\int \int d\mathbf{r}^{1N} d\mathbf{r}^{2N} e^{-\beta[U_{11} + U_{22}]}} = \langle e^{-\beta \Delta U(R_{12})} \rangle. \quad (2.7.31)$$

Taking the logarithm of this expression we obtain

$$\beta V_{eff} = -\ln \langle e^{-\beta \Delta U(R_{12})} \rangle, \quad (2.7.32)$$

which is consistent with the effective potential obtained from the estimation of the radial distribution function in the zero-density limit (see eq. (2.7.26)).

Eq. (2.7.32) provides the basis for computing the effective potential in computer simulations. The advantage of Widom's insertion method is that one needs only simulate a single complex particle (in our case, a single polymer), although two of these are required to construct the effective potential. Running simulations for a single polymer one needs to collect a large number of independent polymer configurations in equilibrium. Then, taking two arbitrary configurations and placing them, so that their centers of mass coincide, we compute the potential energy $\Delta U(R_{12} = 0)$ between the monomer belonging to the different polymers. Consequently, increasing the distance between the polymers with a step of one monomer size and measuring the potential energy at every step, we obtain the inter polymer potential energy $\Delta U(R_{12})$. Repeating this procedure for all possible pairs of configurations, we calculate the mean value of the Boltzmann factor of the inter polymer potential energy at every distance R_{12} . We can then determine the effective potential as a function of R_{12} . Being simple and transparent, Widom's insertion method has been successfully applied to many soft-matter systems, whose effective potential does not exceeds a few $k_B T$ [87], e.g. unconfined chain and ring polymers [88, 89], dendrimers and colloids coated by polyelectrolytes [77].

2.8 Entropic segregation of polymers

Two self-avoiding polymers in confinement repel each other for purely entropic reasons. The repulsion can be very strong, since overlap of the polymers significantly reduces conformational entropy. This drives the polymers towards segregation where the polymers demix moving in the opposite directions, since each of the polymers seeks to gain the entropy of a single polymers. In this section, we discuss the main findings made for understanding of the segregation process following mainly the works [2, 5, 6, 90].

2.8.1 Polymer segregation in cylindrical confinement. Segregation speed and time scale

Consider two linear self-avoiding polymers trapped inside a cylinder of infinite length and diameter D . Each polymer is composed of N monomers of size σ . The cylinder is so narrow that its diameter D is much smaller than the radius of gyration of one unconfined polymer. If the polymers are separated by a distance, so that they do not feel each other's presence, then they expand up to their equilibrium length L_{eq} given by eq. (2.3.34). However, if the polymers are initially in overlap, they start repelling each other with the segregation force F . The segregation force was

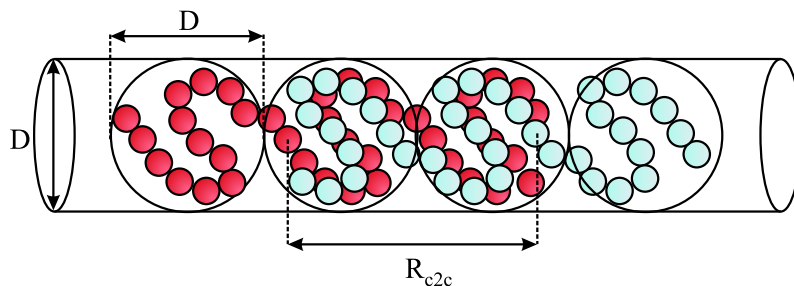


Figure 2.15: Two overlapping linear polymers confined in a cylinder of diameter D and separated by the distance between centers of mass R_{c2c} . Polymers are split into a sequence of blobs of size D .

estimated by Arnold and Jun in Ref. [2] where they employed the de Gennes blob model to treat the segregating polymers (see Fig. 2.15). According to this model, the polymers are split into a sequence of blobs of size D . Using the fact that the overlap of two blobs costs $k_B T$, and assuming that the overlap does not stretch the polymers, the free energy \mathcal{F} of this system depends on the distance between the polymer centers of mass R_{c2c} as

$$\beta \mathcal{F} = \frac{L_{eq} - R_{c2c}}{D}. \quad (2.8.1)$$

Then the segregation force is obtained as the derivative of the free energy with respect to the polymer separation R_{c2c} :

$$F = -\frac{\partial \mathcal{F}}{\partial R_{c2c}} = \frac{k_B T}{D}. \quad (2.8.2)$$

Knowing the segregation force, one can construct the equation of motion for the polymer centers of mass during segregation

$$M \dot{V}_{c2c} = \frac{k_B T}{D} - \Gamma V_{c2c}, \quad (2.8.3)$$

where V_{c2c} is the segregation speed of polymers, each of mass $M = Nm$ with the mass of a single monomer m . Polymer friction is denoted by $\Gamma = N\gamma$, where γ is the friction of one monomer. At the initial condition $V_{c2c} = 0$ at $t = 0$, eq. (2.8.3) has the solution for the segregation speed which scales as

$$V_{c2c} \sim \frac{k_B T}{\gamma D N}. \quad (2.8.4)$$

The inverse proportionality of the segregation speed to the diameter of the cylinder, i.e. the single parameter determining the confinement, leads to a slowing down of polymer segregation in wide cylinders and a corresponding acceleration in narrower cylinders. During segregation the polymers starting from the fully overlapping

2.8. ENTROPIC SEGREGATION OF POLYMERS

configuration cover a distance equal to the equilibrium length of a single polymer, therefore scaling of the segregation time is

$$t_{seg} \sim \frac{L_{eq}}{V_{c2c}} \sim N^2 D^{2-1/\nu}. \quad (2.8.5)$$

The quadratic scaling of the induction time with the number of monomers N indicates that long polymers segregate significantly slower than those composed of fewer monomers. This is also noticeable in the scaling of the segregation speed.

The obtained scalings for the segregation speed and time was proved by molecular dynamics simulations where the polymers were modeled by the bead-spring model [2]. To simulate the segregation process, first one needs to create equilibrium configurations of fully overlapping polymers. However, the initialization of the polymers in the overlap and the following equilibration of this system leads to the polymers to start segregating already during the equilibration process. In order to get the equilibrated configurations where the polymers are still in overlap one needs to hold them in the overlap during the equilibration. To achieve this, Arnold and Jun used the following trick [2]: in the initial configuration each of the two polymers was prepared as a zigzag configuration of monomers linked by bonds.

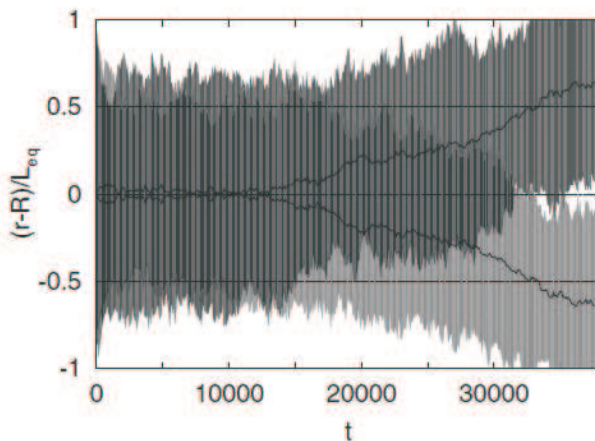


Figure 2.16: Exemplary dynamics of the segregation process. Polymers are composed of $N = 200$ monomers each, the diameter of the cylinder is $D = 7$. The solid lines denote the position of the polymers' centers of mass. Dark and light grey areas correspond to areas occupied by different polymers along the cylinder. The positions of the polymers are relative to the total center of mass and rescaled by the equilibrium length L_{eq} of a single polymer. All the data presented here are collected after removal of the interconnecting bonds. Figure is taken from Ref. [2]. Reprinted figure with permission from A. Arnold and S. Jun, PHYSICAL REVIEW E, 76, 031901, 2007. Copyright (2007) by the American Physical Society.

The two zigzag strands were linked by interconnecting FENE bonds, so that the i -th monomer of one polymer is linked to the i -th monomer of the second polymer. Such a ladder-like configuration was then equilibrated. After equilibration, the interconnecting bonds were removed and we obtained two equilibrated initially overlapping polymers. Thereafter, tracing the position of the centers of mass during the main simulation run, the segregation process was observed. Fig. 2.16 taken from Ref. [2] shows the distance between the centers of mass $R_{c2c}(t)$ along the main cylindrical axis as a function of time measured during a simulation run. When the interconnecting bonds are removed the distance between the centers of mass is zero and corresponds to the time $t = 0$ in Figure 2.16. This distance stays around zero during a time which has been called the induction time and will be discussed later. Eventually, R_{c2c} starts growing, that indicates the initiation of the segregation process, and continues until $R_{c2c} = L_{eq}$, when the polymers do not overlap anymore. Thus, the segregation process was completed and the simulations can be terminated. The simulations of the segregation process were repeated at least 200 times for various system parameters: the length of polymers was 100, 200 and 300 monomers and the diameter of the cylinder varied from 1.5 up to 13 in unites of monomer size. The same picture was observed in Ref. [1] where polymer segregation was studied using Monte-Carlo simulations.

To compute the segregation speed and time, the function $R_{c2c}(t)$ of every sim-

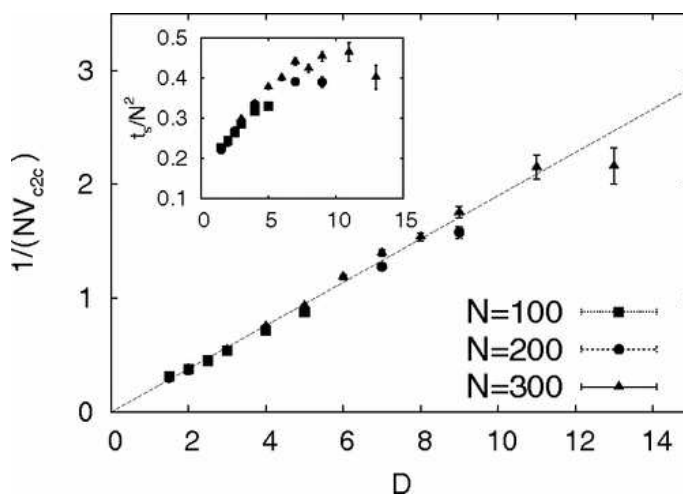


Figure 2.17: Inverse segregation speed V_{c2c} rescaled by the number of monomers N per polymers as a function of the cylinder diameter D . The dash line corresponds to the theoretical prediction given by eq. (2.8.4). Insert: Segregation time t_s rescaled by the squared number of monomers N^2 as a function of the cylinder diameter D . Figure is taken from Ref. [2] and reprinted with permission from A. Arnold and S. Jun, PHYSICAL REVIEW E, 76, 031901, 2007. Copyright (2007) by the American Physical Society.

ulation run was fitted in the range between D and $L_{eq} - D$ by a linear function $V_{c2c}(t - t_i)$, where t_i is the time when the polymers are separated by the distance D which is equivalent to one blob size. The results of the fitting of the segregation speed and time averaged over all simulation runs are represented in Fig. 2.17 taken from Ref. [2] and confirm the theoretically obtained scaling of these quantities given by eq. (2.8.4) and (2.8.5).

However, the polymers do not always start segregating immediately. As one can see in Fig. 2.16, the distance between the centers of mass fluctuates around zero during a period of time called induction. Obviously, during the induction phase the initial symmetry of the system has to be broken in order to initiate segregation. Arnold and Jun [2] suggested that polymers are driven by diffusion during this phase and provided a scaling for the induction time as N^3 , which in fact exceeds the time spent by the polymers for segregation. In Chapter 3, we discuss the problem of the induction phase in more detail, refuting the hypothesis that induction phase is diffusive and provide the correct scaling of the induction time based on Kramers' theory. Moreover, we will revisit the theory of the segregation process and calculate the segregation force taking into account polymer stretching in the overlap region.

2.8.2 Ring polymers in cylindrical confinement

Two self-avoiding ring polymers repel each other much stronger than two equivalent linear polymers composed of the same number of monomers as the rings. Even in the unconfined case, closing a linear polymer to a ring increases the monomer density around its center of mass and self-avoidance of monomers leads to extra repulsion between them. Therefore, a ring topology requires additional free energy in comparison with linear polymers, although the radius of gyration of one ring is about half that of a linear chain due to the closed structure of the ring. For the same reason, the overlap of two rings is more energetically costly than the overlap of linear chains, however, the energetic penalty for overlapping is still of order $k_B T$ (see Fig. 1 in ref. [91] where the effective potentials of polymers for both topologies are presented).

The free energy of overlapping rings should be even higher once they are trapped in a cylinder. In this case, two overlapping rings will constrain each other more than linear polymers under the same confinement. Thus, effective repulsion of rings is much stronger, enhancing the segregation tendency. Indeed, comparing segregation dynamics of linear chains to that of rings, one can immediately see that rings demix more readily spending less time for segregation than linear polymers [1, 92]. However, tracing the positions of the centers of mass during segregation in a cylinder does not provide any explanation of this phenomenon. In order to find an explanation, one needs to calculate the free energy of rings confined in a cylinder.

It is known that narrow cylindrical confinement stretches a linear polymers along

the cylinder, leading to a linear intrachain ordering [5, 3]. Obviously, ring polymers will also be stretched by the cylinder, and they should be linearly ordered to some degree. This provides us the possibility to link ring polymers to linear polymers. This correspondence between linear and ring polymers under cylindrical confinement was found by J. Jung et. al. In Ref. [6], they proposed the approach allowing to treat a ring polymer confined in a cylinder as two linear chains trapped inside of two independent subcylinders of reduced diameter. Studying the relaxation of rings and linear chains (hydrodynamic effects were neglected) by molecular dynamics simulations, where polymers were either stretched or compressed initially, the authors observed that the scaling of the relaxation time of rings is the same as that of linear chains, but has a different prefactor (see Fig. 1 in ref. [6]). Thus, ring topology does not influence the general scaling of the relaxation time τ with the number of monomers N and diameter of the cylinder D , which is $\tau \sim N^2 D^{0.9}$. This finding deviates slightly from the theoretical prediction of the relaxation time for linear polymers, $\tau \sim N^2 D^{1/3}$, based on the blob-scaling approach [93], however, it confirms earlier simulation results [41, 61, 94]. The deviation of the scaling of the relaxation time obtained from simulations from the theoretical predictions is attributed to the finite chain-size effect [41, 61, 94]. The theoretical prediction can be reproduced simulating a polymer composed of at least 10^5 monomer, which makes it rather costly to compute. Nevertheless, the identical scaling of the relaxation time for both polymer topologies implies that the difference between the topologies can be taken into account by an appropriate rescaling of N and D .

Due to stretching of the ring in a narrow cylinder of diameter D , the ring composed of N monomers can be considered as two linear subchains, each consisting of $N/2$ monomers (see Fig. 2.18 (a)). This replacement of the ring by the two corresponding subchains in the initial cylinder has not brought a beneficial result, however, it reduced the discrepancy between the relaxation times, but did not eliminate it entirely (see Fig. 2a in ref. [6]). The next step is to separate the linear subchains and trap each of them into a subcylinder of reduced diameter $D/\sqrt{2}$ as shown in Fig. 2.18 (b). The diameter of the subcylinder is determined from the condition that the sum of the cross-sectional areas of the two subcylinders should be equal to the cross-sectional area of the initial cylinder. In this case, the relaxation times converge better, but not entirely (see Fig. 2b in ref. [6]). It turned out that the perfect choice for the diameters of subcylinders is $D_{eff}/\sqrt{2}$, where D_{eff} is an effective diameter of the initial cylinder defined as a double mean monomer distance from the main cylindrical symmetry axis, weighted with respect to the monomer density (see Fig. 2.18 (c)). The idea of using an effective diameter is based on the fact that monomers do not fill the cylinder uniformly along the short cylindrical axis. Obviously, the effective diameter is smaller than the actual diameter of the cylinder and found to be $D_{eff} = 0.74D$ for rings and $D_{eff} = 0.64D$ for linear chains, when the initial diameter D is less than 10 times the monomer size. Since the effec-

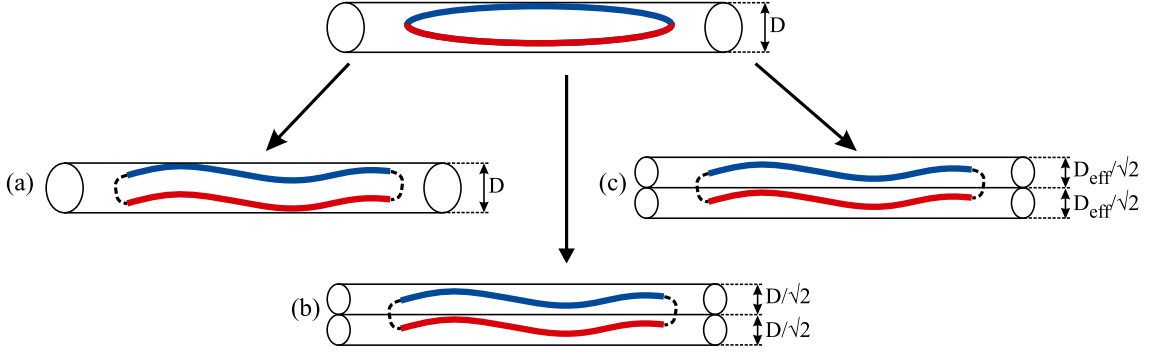


Figure 2.18: Schematic presentation of strategies used for modelling a ring polymer composed of N monomers and confined in a cylinder of diameter D . In all three strategies, the ring polymer is represented as two parallel linear subchains labeled in red and blue colors. Each subchain comprises $N/2$ monomers. (a) Both subchains are trapped in the cylinder of diameter D . (b) Each subchain is trapped in the subcylinder of diameter $D/\sqrt{2}$. (c) Each subchain is trapped in the subcylinder of diameter $D_{eff}/\sqrt{2}$.

tive diameter for rings is larger than for chains, one can conclude that rings occupy space inside the cylinder more effectively. Using the effective diameters, the rescaled relaxation time of rings is in excellent agreement with that for linear polymers, and both follow the expected theoretical prediction $\tau \sim N^2 D^{0.9}$ (see Fig. 2c in ref. [6]). Thus, the ring topology under cylindrical confinement can be most accurately mimicked by two linear chains with the correct rescaling of the number of monomers and diameter of subcylinders confining the chains: $N \rightarrow N/2$ and $D_{eff} \rightarrow D_{eff}/\sqrt{2}$.

It is important to note, that the effective diameters of rings and linear polymers were computed for polymers of finite size. In the case of infinitely long polymers, it is expected that the effective diameters of polymers of both topologies are equivalent and converge to the actual diameter of the cylinder. Then a ring is represented as two parallel subchains, each trapped inside a subcylinder of diameter $D/\sqrt{2}$. Thus, the elongation L of a ring along the cylinder coincides with the elongation of one subchain in the subcylinder and the free energy of the ring $\mathcal{F}_{ring}(L, N, D)$ is equal to the sum of the free energies of subchains:

$$\beta\mathcal{F}_{ring}(L, N, D) = 2\beta\mathcal{F}_{lin}(L, N/2, D/\sqrt{2}), \quad (2.8.6)$$

where the free energy of one subchain \mathcal{F}_{lin} can be calculated using the renormalized Flory approach for a single linear polymer (see eq. (2.3.39)). The exact free energy of a single chain composed of N monomers confined in a cylinder of diameter D as a function of chain elongation along the cylinder can be obtained by adding two constants in front of entropic and interactional terms in eq. (2.3.39):

$$\beta\mathcal{F}_{lin}(L, N, D) = A\frac{L^2}{n_{bl}D^2} + B\frac{Dn_{bl}^2}{L}, \quad (2.8.7)$$

The constants A and B are non-universal constants of order of unity which are only dependent on the type of polymer. Adding these constants we ensure that eq. (2.8.7) gives the exact free energy of the chain in equilibrium (at the equilibrium length $L_{eq}^{lin} = (B/2A)^{1/3}n_{bl}D$) as the number of blobs times the free energy per blob $\mathcal{F}_{bl} = A^{1/3}B^{2/3}3/2^{2/3}$:

$$\beta\mathcal{F}_{lin}(L_{eq}^{lin}, N, D) = \mathcal{F}_{bl}n_{bl}. \quad (2.8.8)$$

According to de Gennes' blob model each subchain composed of $N/2$ monomers can be represented as a sequence of blobs of size $D/\sqrt{2}$. One blob is a unit of the length scale beyond which the polymer feels the confinement. The number of monomers per blob in a subcylinder is equal to $g_{sub} = (D/a\sqrt{2})^{1/\nu} = g2^{-1/2\nu}$, where $g = (D/a)^{1/\nu}$ is the number of monomers inside one blob of size D and $\nu = 3/5$ is the Flory exponent. Then, the number of such blobs is determined as $n_{bl}^{sub} = N/(2g_{sub}) = n_{bl}2^{1/2\nu-1}$, where $n_{bl} = N/g$ is the number of blobs of size D . Substituting these parameters into eq. (2.3.39) the free energy of the ring in terms of the initial parameters of the system N and D converts to the form

$$\beta\mathcal{F}_{ring}(L, N, D) = A2^{(6\nu-1)/2\nu}\frac{L^2}{n_{bl}D^2} + B2^{(2-3\nu)/2\nu}\frac{Dn_{bl}^2}{L}, \quad (2.8.9)$$

Minimization of the free energy $\beta\mathcal{F}_{ring}(L, N, D)$ gives the equilibrium elongation L of the ring along the cylinder:

$$L_{eq}^{ring} = \left(\frac{B}{A}\right)^{1/3} 2^{(3-11\nu)/6\nu} n_{bl}D = 2^{(1-3\nu)/2\nu} L_{eq}^{lin}. \quad (2.8.10)$$

As expected, the equilibrium length of the ring is shorter than the equilibrium length of the corresponding linear chain by a factor of approximately 0.63. Substituting the equilibrium length of the ring into eq. (2.8.9), we obtain the free energy of the ring in equilibrium:

$$\beta\mathcal{F}_{ring}(L_{eq}^{ring}, N, D) = 2^{1/2\nu} A^{1/3} B^{2/3} \frac{3}{2^{2/3}} n_{bl} = 2^{1/2\nu} \mathcal{F}_{lin}(L_{eq}^{lin}, N, D). \quad (2.8.11)$$

This implies that the change of polymer topology from linear chains to rings is energetically costly. The free energy of the ring, which is equivalent to the free energy spent for trapping two subchains in cylinders of reduced diameters, is almost twice the free energy of the equivalent linear polymer. Such a big free energy cost also prevents linear subchains from folding back in the subcylinders and subchains can be viewed as a sequence of blobs which are linearly ordered.

This approach of treating a ring polymers under cylindrical confinement by two linear subchains trapped inside subcylinders has implications for spatial organization of two polymers in a closed cylindrical space to mimic cell-confinement and is discussed in the next section. Moreover, the approach allows us to estimate the free energy of two fully or partially overlapping chains during the segregation process (see Chapter 3). Furthermore, in Chapter 4 we extend this approach for two segregating rings and calculate the free energy as a function of the distance between the polymers' centers of mass.

2.8.3 Spatial polymer organization in closed cylindrical confinement and segregation dynamics

Cylindrical confinement induces spatial ordering of polymers as mentioned in the previous sections. Polymers confined in a cylinder of infinite length are linearly ordered on the length scale larger than the size of a single blob determined by the width of the cylinder. However, polymer spatial ordering can be altered once a polymer is trapped inside a cylinder of a finite length. This change is solely dependent on the asymmetry of the cylinder or, in other words, the ratio of cylindrical axes. This section gives an overview of the polymer spatial ordering under closed cylindrical confinement and its influence on the segregation process.

It is convenient to start the discussion with a description of compression and stretching of a single polymer confined in a cylinder of diameter D and finite length L_{cyl} . If the length of the cylinder is larger than the polymer's equilibrium length L_{eq} given by eq. (2.3.34), the polymer is unperturbed in the longitudinal direction by the presence of the walls closing the cylinder (see Fig. 2.19 (a)). Obviously, the blob picture is valid in this case and the polymer resembles a linear sequence of blobs of size D . Inside each blob, the presence of confinement is not significant. The free energy of the chain can be reproduced by the renormalized Flory approach given by eq. (2.3.38) and predicts the free energy dependence on the longitudinal extension L of the polymer. Taking a derivative of the free energy with respect to L , one can find the scaling relation for the force induced by polymer compression or extension:

$$D\beta f = D\beta \frac{\partial \mathcal{F}}{\partial L} = 2A \left(\frac{L}{L_{eq}} \right) - B \left(\frac{L}{L_{eq}} \right)^{-2}. \quad (2.8.12)$$

The validity of this expression for the force was examined by computer simulations and reported in Ref. [41]. It turned out that eq. 2.8.12 accurately predicts the force for weak compression and stretching when the longitudinal polymer extension is in the range of $0.5L_{eq} < L < 1.2L_{eq}$.

To continue the discussion below we will assume that the longitudinal compression of the polymer was induced by the presence of walls closing the cylinder of a finite length from both sides. Therefore, if the length of the cylinder is less than

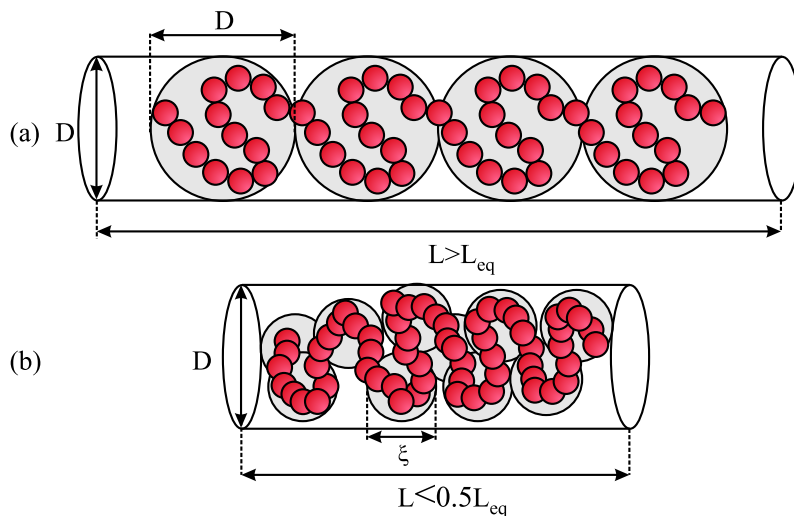


Figure 2.19: Blob pictures of polymers trapped inside a cylinder of finite length. (a) The length of the confining cylinder is larger than the equilibrium length of the polymer. Unperturbed by longitudinal compression, the polymer splits into a series of linearly ordered blobs whose size is determined by the diameter D of the cylinder. (b) The length of the cylinder is smaller than half of the equilibrium polymer length. The diameter of the cylinder is the same as in the case (a). Longitudinal compression causes the breaking up of the blobs of size D into smaller ones of size ξ .

the equilibrium length L_{eq} of the polymer, the longitudinal extension of the polymer always coincides with the length of the cylinder, since the polymer will seek to occupy all available space inside the cylinder to maximize its entropy. However, decreasing the length of the cylinder ($L < 0.5L_{eq}$), the compression becomes so strong that the blob picture is no longer applicable. In this case, the blobs break into smaller blobs [41] as shown in Fig. 2.19 (b), and the free energy has to be calculated in a different way than for weak compression. Since the polymer is strongly compressed, the main contribution to the free energy comes from monomer collisions along the chain, and the polymer can be mapped by the equivalent semidilute polymer solution [90]. The monomer-monomer contact probability within volume V in the semidilute solution was estimated by des Cloizeaus [52, 53], who applied the Lagrangian theory used to study phase-transition models like the Ising model to polymer semidilute solutions. Multiplying the contact probability by the total number of monomers N comprising the polymer, we obtain the free energy of the polymer under strong compression:

$$\beta\mathcal{F} \approx N \left(\frac{Na^3}{V} \right)^{1/(3\nu-1)} \approx \left(\frac{R_g^3}{V} \right)^{1/(3\nu-1)}, \quad (2.8.13)$$

where $R_g \sim aN^\nu$ denotes the radius of gyration of the corresponding unconfined

2.8. ENTROPIC SEGREGATION OF POLYMERS

polymer, and $V \sim D^2L$ is the volume of the cylinder. Note, that eq. (2.8.13) preserves the de Gennes prediction of the free energy cost $k_B T$ per blob. However, in this case the size of the blobs ξ is smaller than the diameter of the cylinder D and determines the correlation length of the monomers, below which monomer correlations are similar to those in the bulk:

$$\xi \approx ag^\nu \approx \left(\frac{Na^{1/\nu}}{V} \right)^{\nu/(1-3\nu)}, \quad (2.8.14)$$

where g denotes the number of monomer per blob of size ξ . The latter approximation has been found from the condition that the monomer concentration ρ within the cylinder remains the same as within a single blob: $\rho = N/V = g/\xi^3$. Thus, the compression force in the strongly confining cylinder is

$$-D\beta f \sim \left(\frac{L_{eq}}{L} \right)^{3\nu/(3\nu-1)} \sim \left(\frac{L_{eq}}{L} \right)^{9/4}. \quad (2.8.15)$$

This scaling of the compressing force has been confirmed by computer simulations for $L < 0.5L_{eq}$ [41]. Therefore, the force-compression relation can be applied for studying the elastic response of chromosomes of elongated bacteria which are tightly trapped inside a bacterial shell.

Compressing a single polymer inside a cylinder of a finite length we have observed two pictures, namely, the polymer resembles a linear string of blobs under weak compression, whereas moderate compression causes a breaking of this ordering and altering the blob picture, so that blobs are no longer linearly ordered. Similar effects were observed for the system of two polymers trapped inside a cylinder of finite length [3, 5, 95]. Let us fix the diameter of a narrow cylinder and start reducing the length of the cylinder by a system of pistons pushing on the ends of the cylinder. If initially the length of the cylinder is twice as long as the double equilibrium length L_{eq} of one of the polymers under the same cylindrical constraints, and the polymers are in the segregated state, they do not feel any longitudinal compression induced by the pistons and the presence of each other (see Fig. 2.20 (a)). Therefore, the polymers will remain segregated because their mixing requires free energy. Thus, the compressing force is equal to zero and each polymer is described by the traditional blob model where the blobs are the size of the diameter of the cylinder and ordered linearly. Moving the pistons towards each other, the polymers become weakly compressed, however, they still resist mixing and resemble “touching cigars” as shown in Fig. 2.20 (b). The resistance to mixing continues until the compression force reaches the magnitude that corresponds to the longitudinal compression of each compressed polymer up to approximately $0.5L_{eq}$ [3]. The compressing force grows according to the scaling (2.8.15), if we continue compressing the polymers. In this moderate compression regime, blobs comprising each polymer break into smaller ones as previously discussed. The polymers start partially overlapping (compare Fig. 2.20 (c)),

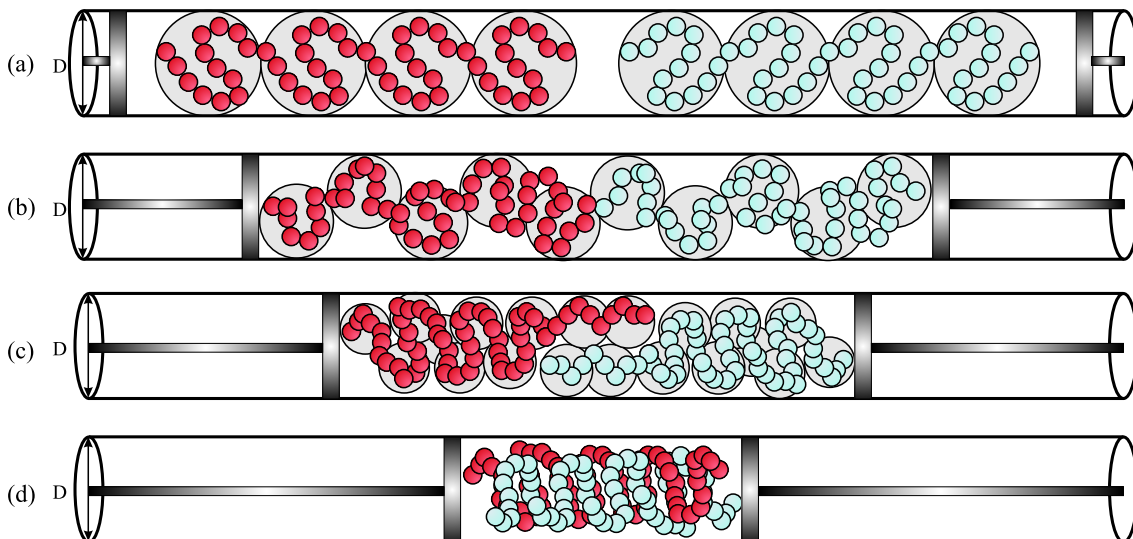


Figure 2.20: Schematic illustration of two self-avoiding polymers trapped between two pistons in a cylinder of diameter D . (a) The distance between the pistons is larger than twice equilibrium length of one polymers. Polymers are represented as linear sequences of blobs of size D . (b)-(d) Polymers are compressed longitudinally. (b) Weak compression regime. Polymers remain segregated in spite of compression. (c) Moderate compression regime. Polymers start overlapping partially. (d) Strong compression regime. Polymers are mixed completely.

since after losing their linear ordering the polymers can more easily penetrate each other trying to minimize the free energy cost of the strong compression. However, the penetration is also energetically expensive, since it inserts the linear ordering in the region of the overlap, therefore polymers have to find an energetic balance between the ordering in the overlap and the compression outside this region. In the strong compression regime, the size of the blobs becomes comparable to the size a of one monomer and the force scales cubically with the length of the cylinder. Such a strong compression forces the polymer to mix completely as shown in Fig. 2.20 (d).

It is worth mentioning that the polymers trapped inside of a wider cylinder mix more readily [3], since the free energy cost of overlap is independent of the blob size, but depends on the number of blobs. Obviously, the size of the blobs in the overlap is larger for wider cylinders, leading to fewer blobs in the overlap. This means that the miscibility of linear polymers under cylindrical confinement strongly depends on both the length of the cylinder and its diameter. This dependence is reflected in the miscibility diagram [3, 5]. This diagram shows the length of the overlap region in the plane of $x = R_F/D$ and $y = R_F/\xi$ axes, where $R_F \sim N^\nu$ is the Flory radius and ξ denotes the size of the blobs or the correlation length of self-avoidance. The

diagram is based on the convention that $\xi = \phi^{-3/4}$, where ϕ is the volume fraction of monomers [47]. Walking along the x axis we reduce the cylinder in diameter, whereas an increase in y corresponds to diminishing the blob size ξ and occurs when the length of the cylinder decreases. Thus, this diagram provides comprehensive information about polymer miscibility for all possible cylindrical confinements starting from very long narrow cylinders up to disk-like confinement. The main conclusion from the diagram is that the asymmetry of the cylindrical confinement is required for effective polymer segregation either along the longitudinal axis, if the cylinder is elongated, or along the radial axis, if the cylinder has a disk-like shape. The corresponding diagram for ring polymers which is based on the same principles as the one for linear polymer can be found in Ref. [6]. Comparing the diagrams for polymers of both topologies one can see that rings are less miscible than linear polymers, since the effect of ring topology corresponds to reducing of the confining cylinder as discussed in the previous section.

More general information about polymer miscibility or, in other words, their segregation tendency was reported in ref. [40] where the phase diagram of two linear polymer in a closed geometry of dimension $D \times D \times L$. This diagram is similar to the abovementioned diagrams, however, it covers not only all the regimes found in cylindrical confinement, but also allows us to compare the segregation tendency for slit-like confinement with different aspect ratios.

Chapter 3

Segregation of linear polymers under cylindrical confinement

As it has been underlined in the Introduction, entropy is the main mechanism driving polymers confined in a cylinder toward segregation, since two overlapping polymers tend to demix in order to gain the conformational entropy of single polymers in the cylinder. In the past years considerable effort has been made to investigate this entropic process and obtain its time scales. In the work [2] the time scale of the entropic segregation for two self-avoiding polymers has been theoretically derived using the de Gennes' blob model and proved by computer simulations. The main theoretical assumption in this model was that the overlap of polymers does not stretch them. The latter means that the entropic force driving the polymer segregation remains constant during the whole process. However, in reality, overlap of polymers leads to an increase of the polymer length along the cylinder due to inter-polymer self-avoidance and, therefore, the segregation force has to change with the length of the overlapping region. In this Chapter, we recalculate the segregation force taking into account polymer stretching which depends on the length of the overlapping region. To this aim, we split the system into overlapping and nonoverlapping regions and use the renormalized Flory approach [6, 41] to estimate the free energies of these "territories". With this, we are able to calculate the free energy of segregating polymers at any degree of the polymer separation. We show that the segregation force computed from the free energy is indeed nonconstant during segregation, but this fact does not influence the main scaling of segregation time obtained in Ref. [2].

However, the simulations in the work [2] also show that the initial symmetry of the system has to be broken before the entropic segregation can set in. Before this has happened, two initially fully overlapping chains do not move with respect to each other, and no segregation can take place. Usually, this induction phase takes a short period of time, but it might last even longer than the segregation process itself. In the work [2] it was argued that the symmetry breaking is a diffusive process with

3.1. FORCE CALCULATION OF SEGREGATING LINEAR POLYMERS.

much slower timescale than the actual segregation [2]. In this Chapter we show that the main mechanism of induction is not diffusion of the entire chains, but rather the arrangement of the chain ends to a configuration allowing to initiate segregation. The correct arrangement is in fact a rare event that causes an exponential timescale of the induction with the number of monomers.

The material of this chapter has been published in Ref. [92, 96] together with A. Arnold:

- Elena Minina and Axel Arnold – Induction of entropic segregation: the first step is the hardest. *Soft Matter*, **10**(31), 5836-5841, 2014.¹
- Elena Minina and Axel Arnold – Entropic segregation of ring polymers in cylindrical confinement. *Macromolecules*, **48**(14), 4998-5005, 2015.²

3.1 Force calculation of segregating linear polymers.

We consider two self-avoiding linear polymers confined in an infinitely long cylinder of diameter D as shown in Fig. 3.1, where each polymer consists of N monomers of size a . Note, that the cylinder is so narrow that its diameter is significantly smaller than the radius of gyration of the single unconfined polymer ($D \ll R_g$). In the following, we compute the free energy of overlap of those two polymers as a function of the center of mass distance R_{c2c} . This implies that we assume that the dynamics are much faster than segregation, so that the latter is a quasi-static process and is therefore unaffected by hydrodynamic interactions. From the obtained free energy we derive the segregating force, which is not constant as previously assumed [2].

In the de Gennes blob model [47], a single polymer in such a cylinder is modeled as $n_{bl} = N/g$ blobs of size D and g monomers each. Because the blob size is equal to the cylinder diameter, the monomers within a blob do not hit the confinement and behave like in a free polymer, so that $g = (D/a)^{1/\nu}$ with the Flory exponent $\nu \approx 0.6$. The free energy of compression is then

$$\mathcal{F} = \mathcal{F}_{bl}n_{bl}, \quad (3.1.1)$$

where the free energy per blob \mathcal{F}_{bl} is a nonuniversal constant. For two nonoverlapping polymers, the free energy is just twice this value.

To calculate the free energy of two (partially) overlapping polymers, we use the renormalized Flory approach of Jung et al [6]. The idea is that the overlap of

¹Reproduced by permission of The Royal Society of Chemistry

²Reprinted with permission from E. Minina and A. Arnold, *Macromolecules*, **48**(14), 4998-5005, 2015. Copyright (2015) American Chemical Society.

CHAPTER 3. SEGREGATION OF LINEAR POLYMERS UNDER
CYLINDRICAL CONFINEMENT

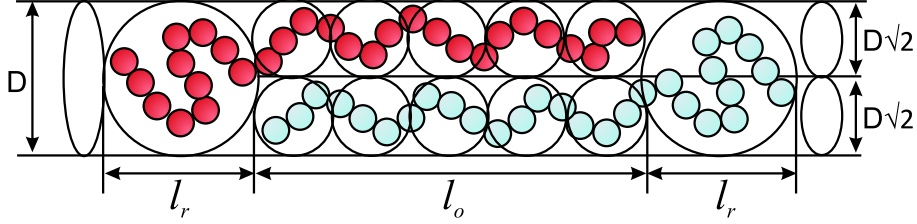


Figure 3.1: Two linear polymers of equal length in a cylinder of diameter D during segregation. In the overlap region, the cylinder splits into two subcylinders of diameter $D/\sqrt{2}$. The overlapping part spans a distance of l_o along the cylinder, the released parts occupy sections of length l_r each.

two chains in a cylinder of diameter D costs the same amount of free energy as trapping these chains into two subcylinders of reduced diameter $D/\sqrt{2}$ individually (see section 2.8.2 for more details). In a way, each polymer occupies its own distinct territory. Now, we split the system into three parts along the main cylindrical axis, with two regions where monomers are already released from the overlap and the overlap region (see Fig. 3.1). In the two outer regions, the free energy can be described by single chains of N_0 monomers each in a cylinder of diameter D . The free energy of the released parts is therefore

$$\mathcal{F}_r(n_0) = 2\mathcal{F}_{bl}n_0, \quad (3.1.2)$$

where $n_0 = N_0/g$ is the number of blobs in the overhanging regions.

The overlap region contains the remaining $N - N_0$ monomers of each polymer, which split into $(N - N_0)/g_{sub}$ blobs of size $D/\sqrt{2}$ consisting of $g_{sub} = (D/\sqrt{2}a)^{1/\nu} = g2^{-1/2\nu}$ monomers. Therefore, the free energy of the polymers in the overlap region is

$$\mathcal{F}_o(n_0, n_{bl}) = 2\mathcal{F}_{bl}(n_{bl} - n_0)2^{1/2\nu}, \quad (3.1.3)$$

leading to the total free energy of

$$\mathcal{F}_{2ch}(n_0, n_{bl}) = 2\mathcal{F}_{bl} [n_0 + (n_{bl} - n_0)2^{1/2\nu}], \quad (3.1.4)$$

and the force of

$$F_{2ch} = -\frac{\partial \mathcal{F}_{2ch}(n_0, n_{bl})}{\partial R_{c2c}} = 2\mathcal{F}_{bl}(2^{1/2\nu} - 1)\frac{\partial n_0}{\partial R_{c2c}}, \quad (3.1.5)$$

where R_{c2c} is the distance between the centers of mass of the two polymers. Note that we need only the partial derivative with respect to n_0 , because $n_{bl} = N/g$ does not change during segregation. However, due to the smaller accessible volume, the polymers stretch noticeably in the overlap region, and R_{c2c} does not scale proportional to n_0 , as assumed in Ref [2].

3.1. FORCE CALCULATION OF SEGREGATING LINEAR POLYMERS.

We are thus left with calculating the right most derivative in eq. (3.1.5). To this aim, we first express R_{c2c} as a function of n_0 and then invert this functional dependence. The length along the cylinder occupied by the released parts is $l_r = n_0 D$, and the length spanned by the overlapping part is

$$l_o = \frac{(N - n_0 g) D}{g_{sub} \sqrt{2}} = (n_{bl} - n_0) D 2^{1/2\nu - 1/2}. \quad (3.1.6)$$

Taking the system's center of mass as the origin, the centers of mass of the two polymers are

$$R_{c\pm} = \pm \frac{m_r}{2M} (l_o + l_r), \quad (3.1.7)$$

where M is the total mass of one polymer, and m_r denotes the mass of polymers in one of the released parts. Because the mass of a polymer is proportional to its number of beads, $m_r/M = n_0/n_{bl}$, and we find

$$R_{c2c} = R_{c+} - R_{c-} = \frac{n_0}{n_{bl}} (l_o + l_r). \quad (3.1.8)$$

Substitution of the lengths gives

$$R_{c2c} = \frac{n_0 D}{n_{bl}} [n_0 + (n_{bl} - n_0) 2^{1/2\nu - 1/2}], \quad (3.1.9)$$

which inverts to

$$n_0(R_{c2c}) = \frac{1}{2[1 - 2^{(1-\nu)/2\nu}]} \left(-n_{bl} 2^{(1-\nu)/2\nu} + \sqrt{n_{bl}^2 2^{(1-\nu)/\nu} + 4[1 - 2^{(1-\nu)/2\nu}] \frac{R_{c2c} n_{bl}}{D}} \right). \quad (3.1.10)$$

Taking the derivative of eq. (3.1.10) with respect to the R_{c2c} and substituting it into eq. (3.1.5) we obtain

$$F_{2ch} = \frac{\mathcal{F}_{bl} [2^{1/2\nu} - 1] 2^{(3\nu-1)/2\nu}}{D \left(1 + 2[2^{(\nu-1)/2\nu} - 1] \frac{n_0}{n_{bl}} \right)}. \quad (3.1.11)$$

The ratio n_0/n_{bl} varies from 0 to 1 during segregation, therefore the segregation force is not constant, but increases by 80% toward the end of segregation, see Fig. 3.2. Polymer stretching is clearly observed in the simulation results as presented in Fig. 6 (a-d) of Ref. [2]. The overlapping polymers are about 20% longer than they are after segregation, that is in good agreement with our estimate. Fig. 2 in the same reference also shows the acceleration of segregation towards the end of the process.

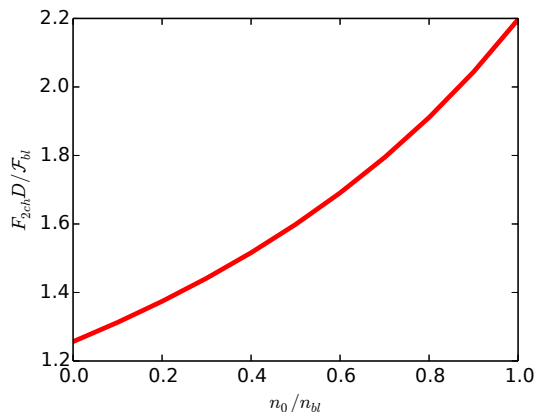


Figure 3.2: Segregation force of two chains trapped in a cylinder rescaled by the diameter of the cylinder and free energy per one blob \mathcal{F}_{bl} as a function of ratio n_0/n_{bl} .

Note that the scaling of the force with respect to diameter of the cylinder is always $F \sim 1/D$, irrespective of whether this compression is taken into account. Therefore, the scaling prediction $V \sim 1/(ND)$ for the *average* segregation speed given in Ref. [2] for a constant segregation force is still a good approximation. Because of that, the segregation time scaling of $t_s \sim N^2 D^{2-1/\nu}$ also holds for long polymers.

3.2 Induction phase

In this section, we investigate the origin of the induction phase which occurs before the segregation of polymers under cylindrical confinement sets in. The idea that the induction is diffusive has been rejected when we repeated simulations of polymer segregation and plotted the distribution of the induction and segregation times. Note, that the details of these simulations are presented in section 2.8.1 and we unconditionally followed this description to set up the simulations. Fig. 3.3 shows the distributions of induction and segregation time for segregation of two polymers with $N = 300$ beads each in the cylinder of diameter $D = 7$. The polymers are completely free to move, but are initially set up such that they fully overlap. The distributions clearly differ, with the induction time being exponentially distributed. In this case of relatively short chains, the mean induction time is still shorter than the mean segregation time, but already comparable. This shows that the induction phase is by no means negligible in the overall segregation process. The exponential distribution of induction time contradicts the earlier proposed in Ref. [2] idea of the diffusive induction with time scale $N^3 D^{2-2/\nu}$.

In the following we demonstrate that during the induction phase the polymer ends rearrange themselves so that the configuration of polymers becomes appropri-

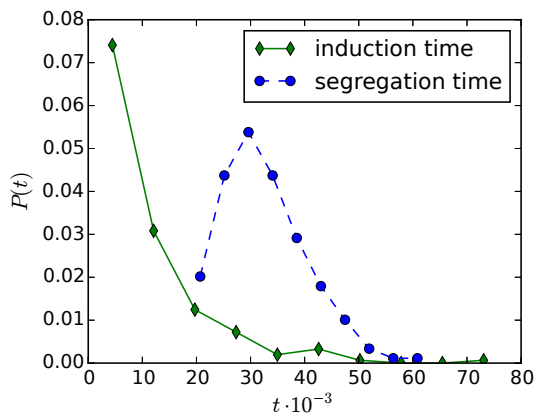


Figure 3.3: Exemplary distribution of the induction and segregation time t obtained from computer simulations of polymers consisting of $N = 300$ beads each in a cylinder of diameter $D = 8$.

ate for segregation. In order to start segregation, the two overlapping chains need to arrange such that different chains hang over at the two ends of the polymers (compare Fig. 3.4 (b)). In such a configuration, a small displacement of the size of a blob is sufficient to start segregation. If, however, one of the polymers is trapped between the ends of the second one, segregation cannot start (Fig. 3.4 (a)). This trapping is the main origin of induction, and the timescale of induction is the timescale of the polymers switching roles at one of the ends. In the following we calculate the induction time theoretically and perform molecular dynamics simulations to prove the theoretical predictions.

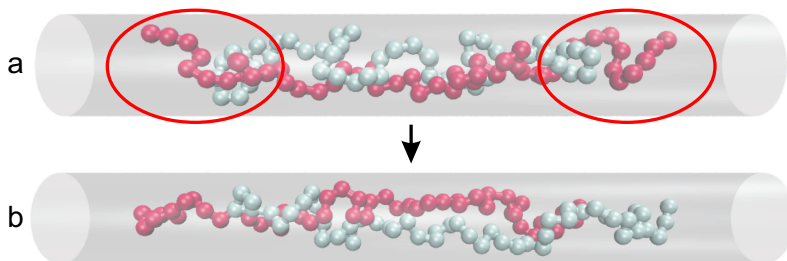


Figure 3.4: Ordering of two polymers in a cylinder: (a) typical trapped polymer configuration during the induction phase; (b) configuration that allows for entropic segregation.

3.2.1 Theoretical calculation of induction time

For simplicity, we consider only one half of the two polymers, that is, two overlapping self-avoiding linear polymers that consist of $N = N_t/2$ monomers of size a each and are confined in a cylinder of diameter D . Here N_t is the number of monomers belonging to one of the polymers of the full system. Rather than enforcing full overlap, we allow the chains to segregate partially, however, only at the one end of the two chains, compare Fig. 3.5. The other side corresponds to the center of the overlapping polymers. If the chains are sufficiently long, this is justified, because there is barely any interaction between the two ends. We use the difference d between the positions of the outermost beads of the chains to characterize the overhang. If $d = 0$, the chains are fully overlapping, however, we will show that this is typically entropically disfavored. Role switching of the chain ends is characterized by a sign switch of d . The timescale of this process is what we are interested in, since it characterizes the timescale to overcome a trapped configuration.

To determine the free energy of this system, we use the renormalized Flory approach [41] described in Chapter 2. A single polymer of length N in a cylinder of diameter D is represented as a chain of $n_{bl} = N/g$ blobs, where $g = (D/a)^{1/\nu}$ is the number of monomers per blob with $\nu \approx 0.6$. Inside such a blob, the polymer is considered to be a free self avoiding polymer with g monomers. The diameter of such a blob is the size of a free polymer coil of g beads, which by construction is D . Then the equilibrium length of the polymer is $L_{eq} = n_{bl}D$ and its free energy is [47, 41, 6]

$$\mathcal{F}(n_{bl}) = \mathcal{F}_{bl}n_{bl} = \mathcal{F}_{bl}N/g, \quad (3.2.1)$$

where the constant \mathcal{F}_{bl} is the free energy per blob, a nonuniversal constant depending on the type of polymer. Note that the diameter D enters the free energy only through

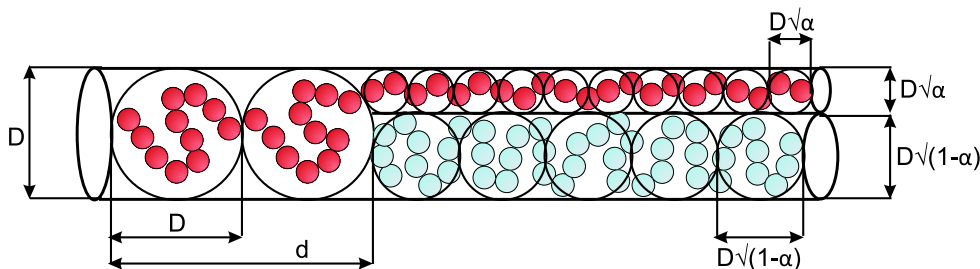


Figure 3.5: Schematic view of an overhang configuration. The blob size is equal to the cylinder diameter D , the overhang is described by the difference d between the positions of the leftmost beads of the two chains. In the overlap region, we follow the model of Jung et al. [6] and assume the two chains to be confined to effective cylinders of diameter $D\sqrt{\alpha}$ and $D\sqrt{1-\alpha}$, respectively.

the number of monomers in a blob, g .

The free energy of our system consists of three contributions: the first one is the free energy of the overhanging tail, the second and third contributions are the free energy of the remaining part of this polymer in the overlap region and the free energy of the other polymer, respectively. The free energy of the overhanging tail consisting of $n_o = d/D$ overhanging blobs can be directly computed from the Flory energy and is

$$\mathcal{F}_1(n_o) = \mathcal{F}_{bl}n_o. \quad (3.2.2)$$

To compute the free energy of the second and third contributions, we extend the renormalized Flory approach proposed by Jung et al [6]. In this approach two fully overlapping polymers in a cylinder with diameter D are treated as two single polymers trapped in effective subcylinders of reduced diameter $D/\sqrt{2}$ each.

The overhanging polymer contributes less monomers to the overlap region than the trapped one, and thus occupies less space. This we model by considering two subcylinders with effective diameters $D_2 = D\sqrt{\alpha}$ and $D_3 = D\sqrt{1-\alpha}$, respectively, so that the parameter α is the area fraction of the cylinder occupied by the overhanging polymer in the overlapped region. Each subcylinder confines a single polymer that can be again considered as a sequence of blobs with a free energy given by eq. (3.2.1).

For the subcylinder of diameter D_2 the polymer splits into $(N - n_o g)/g_2$ blobs with $g_2 = (D_2/a)^{1/\nu} = g\alpha^{1/2\nu}$ monomers, so that its free energy is

$$F_2 = \mathcal{F}_{bl}(n_{bl} - n_o)\alpha^{-1/2\nu}. \quad (3.2.3)$$

The trapped chain in the subcylinder of diameter D_3 has its full N beads in the overlap region and thus consists of N/g_3 blobs, where the number of monomers per blob is $g_3 = (D_3/a)^{1/\nu} = g(1-\alpha)^{1/2\nu}$. Its free energy is therefore

$$F_3 = \mathcal{F}_{bl}n_{bl}(1-\alpha)^{-1/2\nu}. \quad (3.2.4)$$

Combining the three contributions, the free energy of the system with $n_o = |d|/D$ overhanging blobs can be written as

$$\mathcal{F}(n_o, n_{bl}) = \mathcal{F}_{bl}[n_o + (n_{bl} - n_o)\alpha^{-1/2\nu} + n_{bl}(1-\alpha)^{-1/2\nu}]. \quad (3.2.5)$$

Here, the diameter D enters the free energies only indirectly through the number of monomers in a blob. We determine the parameter α from the condition that both chain segments in the overlap region should be in equilibrium and occupy the same stretch L along the cylinder:

$$L = (n_{bl} - n_o)D\sqrt{\alpha}^{-1-1/\nu} = n_{bl}D\sqrt{1-\alpha}^{-1-1/\nu}, \quad (3.2.6)$$

CHAPTER 3. SEGREGATION OF LINEAR POLYMERS UNDER CYLINDRICAL CONFINEMENT

which leads to

$$\alpha(n_o, n_{bl}) = \left[1 + \left(1 - \frac{n_o}{n_{bl}} \right)^{2\nu/(\nu-1)} \right]^{-1}. \quad (3.2.7)$$

In the fully mixed state ($n_o = 0$) the splitting parameter is $\alpha = 1/2$, therefore, the free energy of this state has the form

$$\mathcal{F}(n_o = 0, n_{bl}) = \mathcal{F}_{bl} n_{bl} 2^{1+1/2\nu}. \quad (3.2.8)$$

We are left with determining the equilibrium number of overhanging blobs, n_o . To this aim, we insert the equilibrium splitting α in (3.2.5) and rewrite the free energy in terms of the ratio $\delta = n_o/n_{bl} = |d|/L_{eq}$. The free energy difference between configurations with overhang ratio δ given by eq. (3.2.5) and the fully mixed state $\delta = 0$ given by eq. (3.2.8) is

$$\begin{aligned} \frac{\Delta\mathcal{F}(\delta, n_{bl})}{n_{bl}\mathcal{F}_{bl}} &= \frac{1}{n_{bl}\mathcal{F}_{bl}} [\mathcal{F}(\delta, n_{bl}) - \mathcal{F}(\delta = 0, n_{bl})] = \\ &= \delta + (1 - \delta)[(1 - \delta)^{2\nu/(\nu-1)} + 1]^{1/2\nu} + \\ &\quad + [(1 - \delta)^{2\nu/(1-\nu)} + 1]^{1/2\nu} - 2^{1+1/2\nu}, \end{aligned} \quad (3.2.9)$$

which solely depends on the ratio δ . Fig. 3.8 shows this universal free energy difference, which has a single, pronounced minimum, corresponding to the equilibrium state. We denote with \mathcal{F}_{min} the free energy difference per blob between this minimum and the fully mixed state.

Note that our universal free energy curve predicts a nonzero gradient at $\delta = 0$. Therefore, the free energy as a function of the signed distance d has a sharp nondifferentiable peak at $d = 0$, which is clearly unphysical. This is due to the fact that the blob picture no longer holds for the overhanging part if $n_o \ll 1$, i. e. there are much less beads than necessary for a single blob. In that case, the overhanging part no longer feels the confinement, and thus has a different free energy with a smooth curvature. This is confirmed by our simulation data as presented below.

When the polymers switch roles, i. e., in case d switches the sign, the free energy barrier

$$\mathcal{F}_{barrier} = n_{bl}\mathcal{F}_{min} \quad (3.2.10)$$

between the minimum and $n_o = 0$ has to be overcome, making it a rare event. According to Kramers' or reaction-rate state theory [97], the switching rate k is

$$k \sim \mathcal{D} \sqrt{\mathcal{F}_0'' \mathcal{F}_b''} e^{-\beta\mathcal{F}_{barrier}}, \quad (3.2.11)$$

where \mathcal{F}_0'' and \mathcal{F}_b'' denote the curvatures at equilibrium distance and the top of the barrier, respectively. Following the scaling properties of the free energy, \mathcal{F}_0'' and \mathcal{F}_b'' scale like $1/(D^2 n_{bl})$. Finally, \mathcal{D} denotes the diffusion constant, which in our case is dominated by the motion of the outermost blob and therefore scales like $1/g$. Thus, the rate is

$$k \sim \frac{1}{D^2 g n_{bl}} e^{-\beta \mathcal{F}_{barrier}} = \frac{1}{D^2 N} \exp\left(-\beta \mathcal{F}_{min} \frac{N}{g}\right). \quad (3.2.12)$$

Coming back to the initial question of the origin of the induction phase, we note that it is delayed whenever one of the polymers is trapped. To escape this trapping, the polymers have to switch roles at one of the two ends, and the induction time is nothing but the mean first passage time, which behaves like

$$t_{in} \sim \frac{1}{k} \sim D^2 N \exp\left(\beta \mathcal{F}_{min} \frac{N}{g}\right) \sim D^2 N_t \exp\left(\beta \mathcal{F}_{min} \frac{N_t}{2g}\right), \quad (3.2.13)$$

in terms of the total length N_t of the two polymers. Note that there are only two nonuniversal parameters, namely the free energy minimum per blob \mathcal{F}_{min} , which captures the static properties of the polymer, and the proportionality prefactor, which captures its diffusional dynamics.

The most striking feature of eq. (3.2.13) is the exponential dependency on the number of monomers, in contrast to the earlier prediction $t_{in} \sim N_t^3$ based on diffusion of the full chains [2]. We will now present computer simulation results that in depth verify the main assumptions in this derivation and show that eq.(3.2.13) explains the induction time reported in Ref. [2] well.

3.2.2 Simulation details

Our simulations follow the approach used by Arnold and Jun in Ref. [2]. With the aim to investigate switching of the polymer ends during the induction phase we take only halves of the system considered in Ref. [2] due to the symmetry of the system with respect to the its center of mass. Two polymers are trapped inside an open infinitely long cylinder of diameter D . Such cylinder can play a role of the cell membrane of an elongated bacterium, which grows during the cell cycle.

We represent the polymers as a bead-spring chains of $N_t/2$ beads with diameter $a = 1$ in dimensionless units, linked by spring-like bonds. The excluded volume of the beads as well as the wall are modeled by the Weeks-Chandler-Andersen (WCA) potential (2.5.1) described in Chapter 2. The springs between the beads of the chains are finite extensible nonlinear elastic (FENE) bonds (2.5.3) with the maximal stretch $r_F = 2a$ and interaction strength $\epsilon_F = 40k_B T$. Note, that ϵ_F is the product of the spring constant $10k_B T/a^2$ and r_F^2 , so that we employ the same FENE interaction as in Ref. [2].

CHAPTER 3. SEGREGATION OF LINEAR POLYMERS UNDER CYLINDRICAL CONFINEMENT

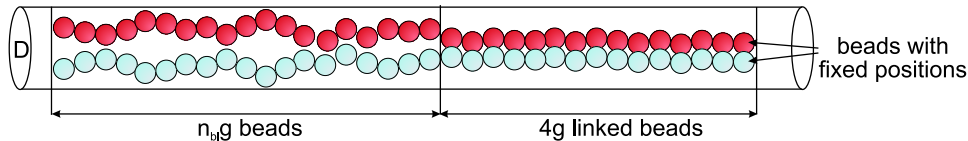


Figure 3.6: Schematic view of the simulation setup. The two rightmost beads are fixed to prevent diffusion, the following $4g$ beads are pairwise cross-linked. Only the remaining $n_{bl}g$ beads on the left are free overlapping polymers.

We perform molecular dynamics simulations of this system using the simulation package ESPResSo [68]. To propagate the system, we employ a velocity Verlet integrator [43] with a fixed time step of 0.01. The system is kept at constant temperature by means of the Langevin thermostat with dimensionless friction 1, which models embedding in a solvent (see section 2.4.3).

For all graphs reported below, we use $\nu = 0.59$ as the Flory exponent. In the simulations of the switching process, we recreate the system used for the theoretical considerations. We consider two polymers of length $(n_{bl} + 4)g$ with two beads on one end fixed, which prevents center of mass diffusion along the cylinder. The number of beads per blob was determined in Ref. [94] from fitting $g = (D/a)^{1/\nu}$ to the single chain data, from which it was obtained that $a = 1.31$. Initially, the system is prepared ladder-like, i. e., the i -th beads of both polymers are bonded. After equilibration we remove $n_{bl}g$ cross-linking bonds, but keep four blobs next to the fixed beads interconnected (compare Fig. 3.6). These four blobs are used as a buffer to prevent back-bending of the polymers. We then vary the diameter of the cylinder $D = 3, 4, \dots, 7$ and the noncross-linked length of the polymers $N = n_{bl}g$, where $n_{bl} = 5, 6, \dots, 20$. The resulting free chain lengths are between 30 and 550 beads. The scaling of the length with the diameter ensures that the polymers are neither too short at large diameters, nor excessively long at small diameters. We perform 500,000 time steps for each parameter set.

3.2.3 Results

Fig. 3.7 shows the evolution of the difference d of the positions of the outermost free beads for an exemplary simulation with $n_{bl} = 10$ blobs in a cylinder of diameter $D = 6$. Sign switching of d indicates that the overhanging polymer has switched. Clearly, this switching is a rare event with a moderate barrier height. Fig. 3.7 also shows that the overhang is on average approximately 2 blobs. This reflects that the trapped polymer cannot be compressed too strongly, but on the other hand, the fully mixed state is unfavorable, as predicted.

From the distribution of the number of overhanging blobs we can compute the free energy of a certain overhang by $\Delta\mathcal{F}(\delta)k_B T = -\ln P(\delta) + \ln P(0)$. Fig. 3.8 shows the free energy distribution for fixed diameter $D = 6$ and fixed $n_{bl} = 10$,

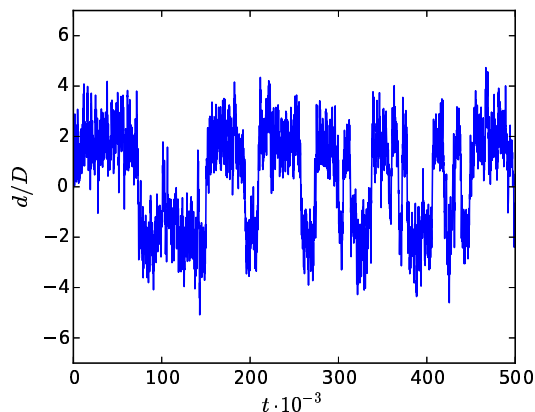


Figure 3.7: Difference d between the positions of the leftmost beads versus time t for two polymers of length $n_{bl} = 10$ beads in a cylinder of diameter $D = 6$. A sign switch indicates that the overhanging polymer has switched.

respectively. We also show our free energy prediction eq. (3.2.9), where we have chosen as the free energy per blob $\mathcal{F}_{bl} = 5k_B T$ to match our simulation results.

While the overall shape is well predicted by our theory, the equilibrium overhang is clearly underestimated. However, if we use an effective overhang of $\delta_{eff} = 0.5\delta$, we can match the simulation data rather well. This is probably due to the fact that the transition between overlap and overhang region is not sharp as in our model, but smoothed out, which effectively decreases the overhang. This assumption is supported by Fig. 6 of Ref. [2], which shows that the density of beads of the overlapping chains gradually changes along the main axis of the cylinder.

Note that the collapse is much better for the constant diameter than constant number of blobs. This is due to the fact that the scaling regime is only realized for relatively large diameters as reported before [2, 6]. However this would require longer polymers, which would make the sampling of the energy barrier problematic due to the large free energy difference. The right hand graphs of Fig. 3.8 demonstrate that unlike our prediction, the free energy is not peaked at $\delta = 0$, but smooth. However, the curvature is surprisingly large, so that this curvature dominates the prefactor of the switching rate.

Fig. 3.9 shows the numerically determined depth of the minimum for a wide range of cylinder diameters and chain lengths. There is some spread in the data because the bottom of the free energy landscape is relatively flat and we report the numerically lowest observed free energy. Nevertheless, for all diameters D and chain lengths, we find the energy barrier to scale linearly with n_{bl} as predicted by eq. (3.2.5), and by fitting to our results, we can determine that $\mathcal{F}_{min} \approx 0.19 \pm 0.05 k_B T$ for our polymer model. This value we use in all remaining plots.

CHAPTER 3. SEGREGATION OF LINEAR POLYMERS UNDER
CYLINDRICAL CONFINEMENT

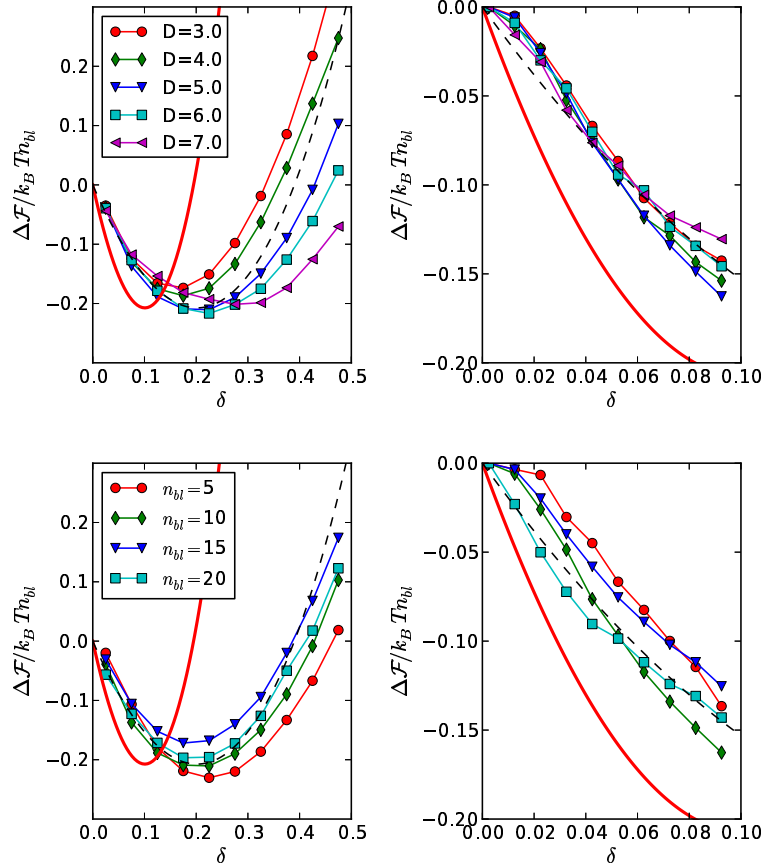


Figure 3.8: Free energy difference landscapes for fixed $n_{bl} = 10$ (top) and fixed $D = 6$ (bottom). The left graphs show free energies as measured in the simulations and our prediction eq. (3.2.9) (solid red) as a function of the ratio $\delta = n_o/n_{bl} = |d|/(Dn_{bl})$, assuming a free energy of $\mathcal{F}_{bl} = 5k_B T$ per blob. The dashed black line gives the same prediction using an effective overhang $\delta_{eff} = 0.5\delta$. The right graphs show the same data, but zoomed in at the top of the barrier. This demonstrates that the free energy difference is a smooth function at the top of the barrier $\delta = 0$.

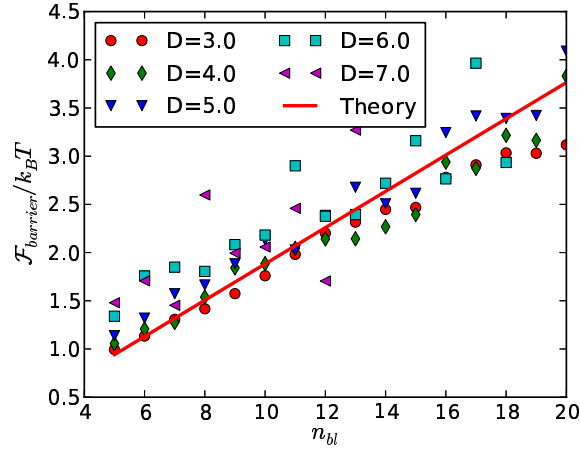


Figure 3.9: The height of the energy barrier $\mathcal{F}_{barrier}$ as a function of the polymer length in terms of blobs $n_{bl} = N/g$ for various diameters D of the cylinder. The line is the theoretical prediction $\mathcal{F}_{min} n_{bl}$, using the free energy barrier per blob $\mathcal{F}_{min} \approx 0.19 k_B T$ as single fit parameter for all curves.

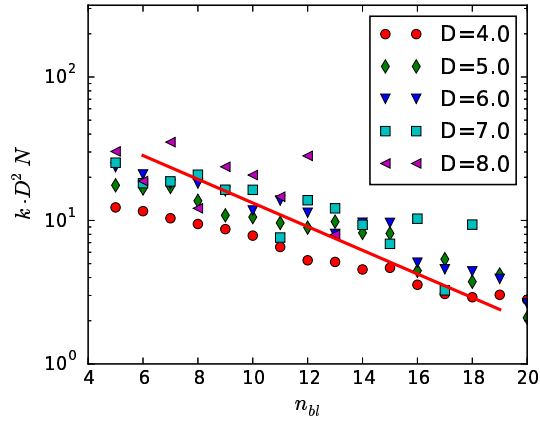


Figure 3.10: The rate of switching k times $D^2 N$ versus the polymer length in terms of blobs $n_{bl} = N/g$. The solid line shows the predicted exponential scaling relation (3.2.12) using the previously measured $\mathcal{F}_{min} \approx 0.19 k_B T$.

CHAPTER 3. SEGREGATION OF LINEAR POLYMERS UNDER CYLINDRICAL CONFINEMENT

Fig. 3.10 shows that the switching rate k also scales as predicted $k \sim \exp(-\beta\mathcal{F}_{min}n_{bl})/(D^2N)$. To that aim, we plot the rate of switching times D^2N versus the polymer length in terms of blobs. In the simulations, we measure the rate of switching by counting sign changes in d , however recording d only every 100 time steps to avoid counting recrossings. Again there is noticeable spread in the data for larger diameters, because the rate decreases with the diameter, making it difficult to measure. However, the $D = 3$ curve clearly lies somewhat below the rest of the data, which we attribute to the fact that the blob picture does not hold well at these relatively small diameters. The data for $D > 4$ distributes around $k = \gamma/(D^2N) \exp(-\beta\mathcal{F}_{min}n_{bl})$, where we insert $\mathcal{F}_{min} = 0.19k_B T$ as determined from Fig. 3.9. The only remaining fitting parameter was the effective friction coefficient γ , which we found to be approximately 12 in dimensionless simulation units [2].

Finally, Fig. 3.11 shows that the induction time scales indeed like $1/k$, as predicted. In this figure, the data given in Fig. 5 of Ref. [2] was replotted not as a function of the diameter D , but as function of the total number of blobs. The induction time was rescaled by D^2N_t , so that eq. (3.2.13) predicts a single exponential increase, which is well reproduced by our data for n_{bl} up to 20. For larger n_{bl} , the data still collapses, but does not follow the predicted exponential. This is due to the fact that by construction of this data, the diameter decreases with increasing n_{bl} , and we reach the lower limit $D = 4$ for the blob picture to hold. Since the

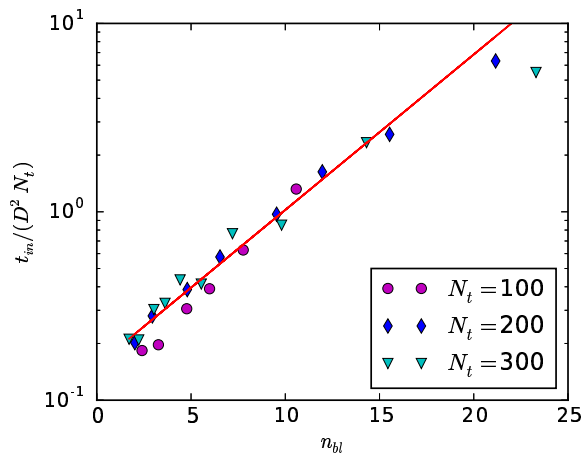


Figure 3.11: The induction time t_{fs} as given in Ref. [2] rescaled by D^2N_t versus the number of blobs n_{bl} for different number of monomers N_t per chain. The data agree well with our theoretical prediction (3.2.13) for the induction time using the previously determined barrier per blob $\mathcal{F}_{min} = 0.19k_B T$, which is shown as red line. Above 20 blobs, the data still collapses, but deviates from the exponential prediction due to small cylinder diameters.

simulation models are identical, we employ the same barrier free energy per blob \mathcal{F}_{min} in the slope of the exponential, which fits the data rather well. This is another strong indication that the role switching plays an important part in the induction phase.

3.3 Modeling replication process

In the previous sections, we considered the polymers that have been initially replicated. However, it is known that replication and segregation in elongated bacteria occurs concurrently [32]. In this section, we check if the replication can influence the induction phase. To this aim we perform molecular dynamics simulations where we consider two initially overlapping linear polymers which replicate with a finite rate. The polymers are modeled with the help of the bead-spring model (see section 2.5) with the same parameters of interactions used in section 3.2.2 dedicated to investigation of the induction time of linear chains. The polymers have been cross-linked initially. To model replication, we remove the cross-linking bonds sequentially at a constant rate of f_{rep} . In this manner we mimic two daughter strands gradually growing from one mother strand, but this approach leads to much more robust molecular dynamics than regularly adding new beads. When the replication is completed, we continue simulations until the end of polymer segregation. We measure the positions of the centers of mass during both replication and segregation. We carried out 200 independent runs for chains of length $N = 200, 300$ and diameters $D = 7, 8$. We also tested different replication rates varying f_{rep} from 1 down to 10^{-2} . This spans the entire relevant range, because time 1 corresponds to the relaxation time associated with the motion of individual beads, while at rate 10^{-2} the replication is slower than segregation.

The distributions of the induction time at different replication rates depicted in Fig. 3.12 show that the induction phase remains pronounced even for polymers replicating at finite rate. Fast replication ($f_{rep} \geq 0.1$ in Fig. 3.12) does not change the induction time distribution compared to immediate replication. At lower rates, the time to full replication determines the segregation time distribution. The most likely segregation time is the one corresponding to the time it takes to full replication, i.e., two independent polymers. Segregation can set in earlier, when about half of the necessary replication time has passed. On the other hand, once the polymers are independent, there is still the exponential distribution observed for immediately replicated polymers. This demonstrates that there is no significant “pre-segregation” of the already replicated parts of the polymers during replication. Even after slow replication, it is still relatively likely to observe situations where one of the polymers is trapped in between the ends of the other one.

Fig. 3.13 shows the distribution of the segregation time at different replication

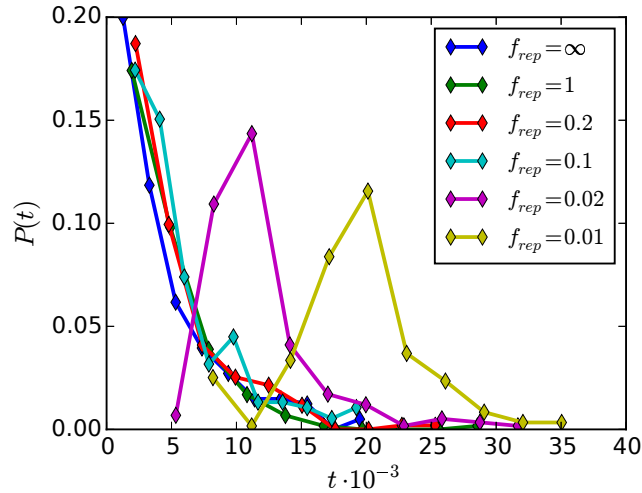


Figure 3.12: Distribution of induction time t of two linear polymers replicating with replication rate f_{rep} obtained from computer simulations. At $f_{rep} = \infty$, the polymers replicate immediately and at $f_{rep} = 1$, the time between two bond releases is the relaxation time of the particle-particle interactions. Each polymer consists of $N = 200$ monomers, the cylinder diameter is $D = 7$. Clearly, the replication rate only has an influence if the replication time exceeds the typical induction time.

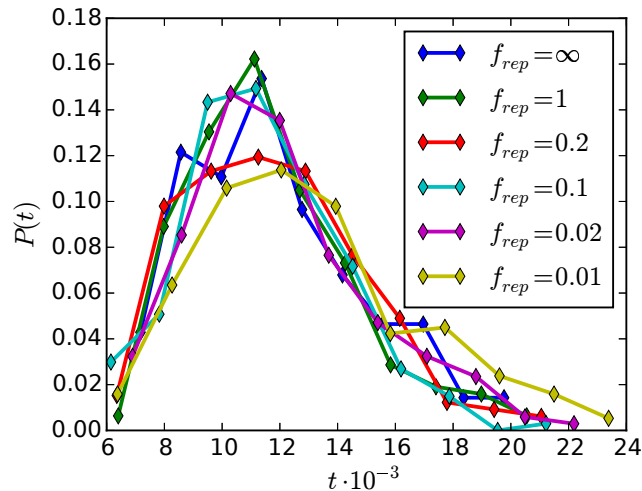


Figure 3.13: Distribution of segregation time t of two linear polymers replicating with replication rate f_{rep} obtained from computer simulations. At $f_{rep} = \infty$, the polymers replicate immediately and at $f_{rep} = 1$, the time between two bond releases is the relaxation time of the particle-particle interactions. Each polymer consists of $N = 200$ monomers, the cylinder diameter is $D = 7$.

rates obtained in simulations. The starting point for counting the segregation time was that when the polymers were displaced by the distance equal to the diameter of the cylinder D or one blob size. The counting continued until the total separation of the polymers. Comparing the distributions for different finite replication rates to the one for immediately replicated polymers ($f_{rep} = \infty$), one can clearly note the similarity in their shapes. This confirms that the replication included into our model does not affect the time-scales of the segregation process.

3.4 Conclusion

In this chapter, we clarified several questions related to segregation of linear polymers under cylindrical confinement. First of all, we proposed a self-consistent approach to calculate the free energy of two segregating polymers at any stage of the segregation process. This approach is based on splitting of the territories occupied by the monomers released from the overlap and those who are still in the overlap. Applying the renormalized Flory approach [6, 41] to each of these territories, we obtain the free energy depending on the positions of the polymers' centers of mass. This allows us to compute forces during polymer segregation taking into account the fact that the overlap of polymers leads to their stretching along the cylinder. We showed that the segregation force is not constant due to the stretching as it has been previously thought, although the latter does not affect the previously obtained scalings for segregation time and speed.

We have investigated the induction phase of the segregation process of flexible chains in a confining cylinder. Our results suggest that the induction phase is not governed by diffusion of the chains as argued before, but rather by an ordering process at the polymer ends. It is entropically favorable for the polymers to at least partially segregate at their ends. As this happens independently, one polymer may be trapped by the other, so that no segregation can take place. This trapped state has to be overcome by switching the roles of the polymers on one side, which is a rare event due to a free energy barrier at full overlap. Both free energy calculations based on the blob model and molecular dynamics simulations show that the height of the barrier is proportional to the number of blobs in the polymer. Using Kramers' theory one can estimate the switching rate and by that the duration of the induction phase, which scales exponentially with the energy barrier and thus the length of a polymer. For long polymers, the induction time therefore becomes dominating over the actual segregation time, making entropic segregation a very slow process on average.

A finite replication rate does not facilitate segregation. Even at slow rates, trapped configurations are as likely as if the polymers would have been replicated immediately, and segregation does not set in before at least half of the polymers

CHAPTER 3. SEGREGATION OF LINEAR POLYMERS UNDER CYLINDRICAL CONFINEMENT

are replicated. This once more confirms that entropic segregation and induction are inevitably linked.

Chapter 4

Segregation of ring polymers under cylindrical confinement

It is known that cylindrical confinement induces linear ordering of chain polymers [1, 3, 6]. Ring polymers due to their topology are even more ordered that enhances segregation [1, 6]. In this Chapter, we introduce a generalization of the renormalized Flory approach proposed by Jung et al [6], the territorial renormalized Flory approach, which allows us to estimate the free energy of many overlapping chains in cylindrical confinement. Using this approach, we investigate the time scales of entropic segregation of rings in open cylindrical confinement, which mimics a growing, idealized simple bacterium of elongated shape. Both segregation and induction take significantly less time for rings compared to linear chains, which we confirm by computer simulations.

The material of this section has been published in Ref. [92] together with Axel Arnold:

- Elena Minina and Axel Arnold – Entropic segregation of ring polymers in cylindrical confinement. *Macromolecules*, **48**(14), 4998-5005, 2015.¹

4.1 Segregating ring polymers

4.1.1 Theoretical details

If we replace the two linear chains by rings, they repel stronger due to the additional self-constraining of the rings. To show that, we repeat the calculation of the segregation force for two overlapping rings, using the renormalized Flory approach also to take into account the ring topology.

¹Reprinted with permission from E. Minina and A. Arnold, *Macromolecules*, **48**(14), 4998-5005, 2015. Copyright (2015) American Chemical Society.

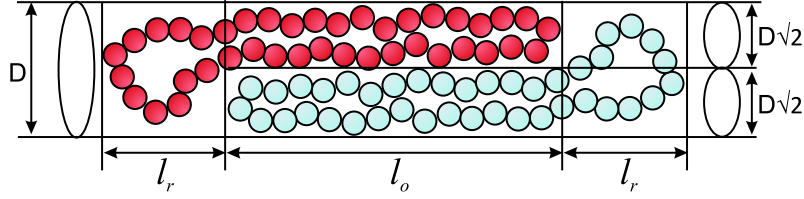


Figure 4.1: Two segregating ring polymers in an infinitely long cylinder of diameter D . The rings only overlap in the region of width l_o , in the nonoverlapping regions of width l_r the rings are only confined by the cylinder. Jung et al. have shown that a single ring polymer in confinement is equivalent to two single chains in subcylinders of diameter $D/\sqrt{2}$. In the overlap region, the accessible volume for each linear subchain is decreased by the presence of three other chains, so that its subcylinder is only $D/2$ wide.

We again split the system into overlapping and nonoverlapping regions as for linear chains (see Fig. 4.1). Let us assume that the total number of monomers of one ring released from overlap is N_0 . In the renormalized Flory approach [6], such a part of a ring is represented by two parallel subchains of length $N_0/2$ monomers each, which are confined to subcylinders of diameter $D/\sqrt{2}$. A blob of this diameter contains $g_{sub} = g2^{-1/2\nu}$ monomers, and the $N_0/2$ monomers in total occupy a section of length $l_r = N_0g^{-1}D2^{(1-3\nu)/2\nu}$. To calculate the length of overlap, we apply this approach twice, we thus deal with four subchains of length $(N - N_0)/2$, trapped in subcylinders of diameters $D/2$ each. Therefore the overlap occupies $l_o = (N - N_0)g^{-1}D2^{(1-2\nu)/2\nu}$ along the cylinder.

The free energy of two overlapping chains of equal length, whether connected in a ring or disconnected, is almost four times as high as the free energy of a single chain, see eq. (3.1.3). Since all the contributions to the free energy can be represented as free energies of overlapping chains, the total free energy of two segregating rings scales as the free energy of two chains (3.1.4) as follows:

$$\mathcal{F}_{2r}(n_0, n_{bl}) = 2^{1/2\nu} \mathcal{F}_{2ch}(n_0, n_{bl}), \quad (4.1.1)$$

where $n_0 = N_0/g$ and $n_{bl} = N/g$. The additional factor 2 in eq. (3.1.3) drops out, because the length of the linear subchains is half of the ring size. Substituting the ring l_r and l_o into eq. (3.1.8), we find the distance between the centers of mass distance is

$$R_{c2c}^r = \frac{n_0 D}{n_{bl}} 2^{1/2\nu-3/2} [n_0 + (n_{bl} - n_0)2^{(1-\nu)/2\nu}] = 2^{1/2\nu-3/2} R_{c2c}. \quad (4.1.2)$$

Then finally the force between two segregating rings is

$$F_{2r} = -\frac{\partial \mathcal{F}_{2r}}{\partial R_{c2c}^r} = -2^{3/2} \frac{\partial \mathcal{F}_{2ch}}{\partial R_{c2c}} = 2^{3/2} F_{2ch}. \quad (4.1.3)$$

CHAPTER 4. SEGREGATION OF RING POLYMERS UNDER CYLINDRICAL CONFINEMENT

Therefore, rings repel noticeably stronger than linear chains of the same length, by a factor of almost 3. However, the scaling of the free energy or force is unaltered by the ring topology.

Solving the equation of motion for the centers of mass provided by eq. (2.8.3), we obtain that the segregation speed of rings V_{c2c}^r scales like

$$V_{c2c}^r \sim \frac{2^{3/2}}{DN} \sim 2^{3/2} V_{c2c}^{ch}, \quad (4.1.4)$$

where V_{c2c}^{ch} denotes the segregation speed of linear chains. Note that this is based on the assumption of a constant force, in practice the segregation accelerates when the polymers have nearly completely segregated. However, just like for linear chains, this describes the scaling of the average segregation speed well, and gives a good estimate for the segregation time. This will be confirmed by our computer simulation data that will be presented in section 4.1.3.

4.1.2 Simulation details

In order to verify our theoretical predictions, we performed molecular dynamics simulations following the approach proposed by Arnold and Jun [2]. We consider an open cylinder of diameter D . Inside the cylinder we trap two ring polymers represented by a bead-spring model. Each polymer consists of N beads of size $a = 1$ with excluded volume interaction modeled by the Weeks-Chandler-Anderson potential (2.5.1). The same potential is used to describe interactions between the beads and the wall of the cylinder. Each bead is linked by two spring-like bonds to its neighboring beads to create a ring, using the finite extensible nonlinear elastic potential (FENE) (2.5.3). The maximal extension of these bonds is $r_F = 1.5a$ and the interaction strength of the FENE potential is $\epsilon_F = k_F r_F^2 = 22.5k_B T$ with the spring constant $k_F = 10k_B T/a^2$. In comparison to Ref. [2] we slightly reduced the maximal extension in order to prevent excessive bond energies, which occur more frequently in ring systems.

The simulations are computed using the simulation package ESPResSo [68]. We employ a velocity Verlet integrator [43] with fixed time step 0.01 to propagate the system. The temperature of the system is kept constant at $T = 1$ using the Langevin thermostat.

We start the simulations in a perfectly symmetric configuration of two overlapping rings. The rings are cross-linked like a ladder, i. e. the i -th beads of both rings are linked. We equilibrate this system, then we remove the cross-linking bonds. Without these additional bonds, the system would start to segregate right away, without equilibrating. Starting from the moment that we cut the cross-links, we compute the centers of mass distance of the rings in order to continue until complete segregation. Simulations are performed for polymers composed of $N =$

100, 200, 300, 600 beads, and we vary the diameter of the cylinder $D = 4, 5, \dots, 13$. We carry out 100 independent simulation runs for each set of parameters of the system.

4.1.3 Results

Fig. 4.2 shows the exemplary segregation dynamics of ring polymers obtained from the computer simulations. Despite different polymer topology, rings trapped in a cylinder segregate similar to the linear chains. Initially the rings are in the fully overlapping configuration, therefore the positions of their centers of mass coincide at the time $t = 0$. Then, the polymers do not move with respect to each other during the induction phase with a small fluctuation of the centers of mass around zero. In the presented example, the blue ring is trapped in between the ends of the red one as it was also observed for linear polymer during the induction. Finally, the switching of the ends on one side of the cylinder has been performed releasing the blue polymer from the trap. With this the polymers start segregating rapidly moving in the opposite directions from each other until they do not overlap any longer. Comparing Fig. 4.2 with the segregation dynamics of linear polymers shown in Fig. 2.16, one can note that the segregation as well as the induction phase take significantly less time for rings than for their linear counterparts.

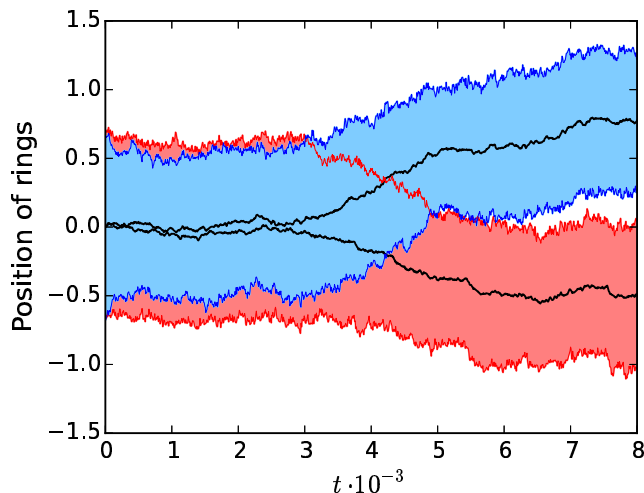


Figure 4.2: Segregation picture of ring polymers. Rings are composed of $N = 200$ monomers each, the diameter of cylinder is $D = 6$. The blue area corresponds to the position of the blue ring. The red area depicts to the position of the red polymer. Black lines in the middle of the areas are the positions of the rings' centers of mass. All the positions are rescaled by the equilibrium length of the corresponding single polymer.

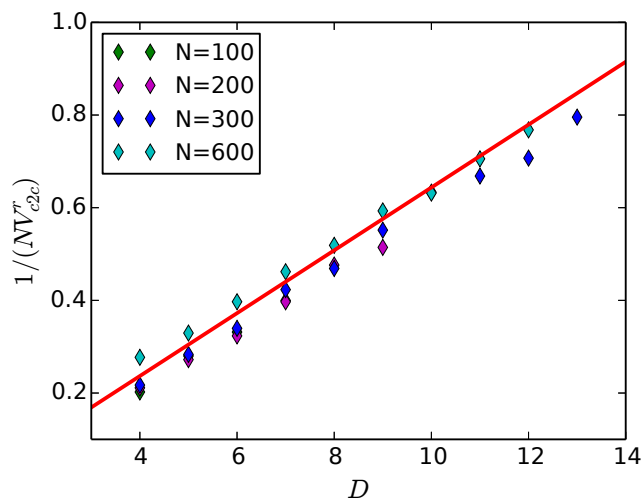


Figure 4.3: Average speed V_{c2c}^r of two segregating rings of different lengths in a cylinder of diameter D , rescaled by the number of monomers per ring. The colored symbols denote the simulation data. The red line is the theoretical prediction (4.1.4), the segregation speed of linear polymers V_{c2c}^{lin} was taken from Ref. [2].

Fig. 4.3 shows the measured in simulations average segregation speed of two ring as a function of the cylinder diameter D . The simulation data are well described by the theoretical prediction eq. (4.1.4). Thus the segregation speed preserves the inverse linear scaling with the polymer length and the diameter of the cylinder. The agreement between the simulation data and theory confirms that the ring topology speeds up the segregation by a constant factor of $2^{3/2}$ over linear chains of the same length as predicted.

Fig. 4.4 shows that the induction time distribution is also qualitatively unchanged, compared to the one for linear chains. The induction time is exponentially distributed as one would expect from an activated process, so that infrequently the induction can take much longer than the following segregation. However, compared to linear chains, rings spend much less time both for induction and segregation.

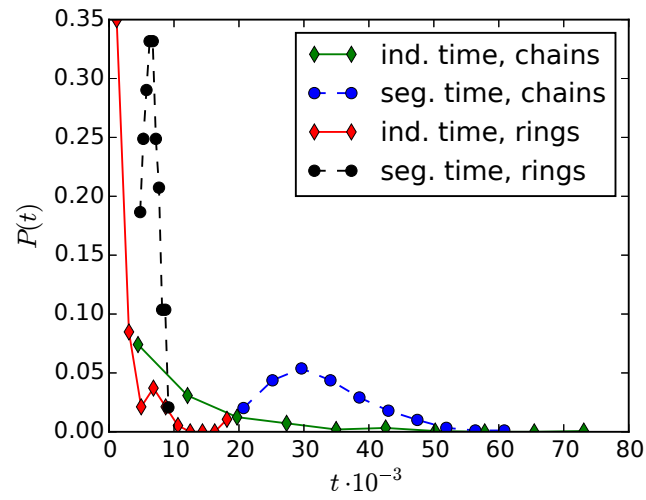


Figure 4.4: Distribution of induction and segregation time t of two ring polymers obtained from computer simulations and of two linear polymers obtained from simulations in Ref. [96]. In both systems each polymer consists of $N = 300$ monomers and the cylinder diameter is $D = 8$.

4.2 Induction phase of ring polymers

4.2.1 Theoretical details

Next, we compute the induction time, i.e., the time the system takes to break initial symmetry. To this aim, two overhanging regions need to form that consist of approximately a blob, or $\approx g$ monomers. However, there is one additional condition, namely that the two overhanging regions are filled by monomers of different polymers (see Fig. 4.5(b)). If they belong to the same polymer, these overhanging regions trap the other polymer, which inhibits segregation (see Fig. 4.5(a)). In the latter configuration, the polymer ends have to switch their relative position on one side of the cylinder before segregation can start. Because of a large free energy barrier at full overlap, this reordering is a rare event. The barrier height is proportional to the length of the polymer, therefore the induction time scales exponentially with the number of beads in the polymers [96], and it is thus much slower than the actual, quadratic segregation time.

We start computing the induction time of ring polymers following the same approach as presented in section 3.2. We consider halves of the two rings that are pinned at the open ends, but can segregate at the other end of the cylinder (see Fig. 4.6). To characterize the switching of the polymer ends, we use the sign of the distance d between the outermost monomers. Like for linear polymers the free energy $\mathcal{F}(N_0)$ of such a system is a sum of three contributions: from the N_0 beads in the overhanging tail of one polymer, from the remaining part of this polymer in the overlap area and from the other polymer, which is completely in the overlap region.

The renormalized Flory approach for the ring topology implies that each of these contributions can be written as the free energy of two overlapping linear chains in appropriate subcylinders. However, in this case, the splitting between the subcylinders is no longer equal: the compressed polymer contributes more monomers to the

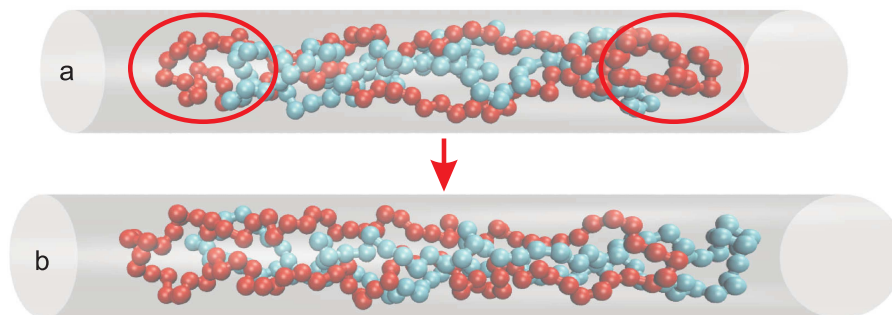


Figure 4.5: Configurations of ring polymers in a cylinder: (a) One polymer is trapped between the overhanging ends of the other polymer during induction phase. (b) Configuration required for polymer segregation.

4.2. INDUCTION PHASE OF RING POLYMERS

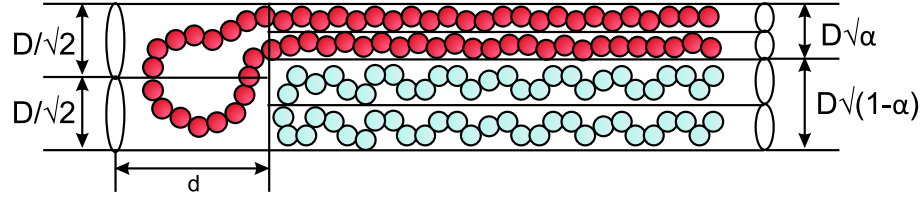


Figure 4.6: Geometry split of halves of two rings used for investigation of induction time during segregation in a cylinder of diameter D . Typically, one chain hangs over, where d is the length of the overhang region. In the overlap region, the numbers of monomers of the two overlapping chains differ, therefore they occupy different amounts of the available cross-section. This is described by the geometric splitting parameter α .

overlap region and therefore also occupies more of the available space. In the following, let α be the fraction of the cross-section occupied by the compressed polymer. Then this half ring is represented by two linear chains of $N/4$ beads each, constrained to a subcylinder of $D\sqrt{\alpha}/2$ (see Fig. 4.6). The chains in the overlap part of the other polymer are confined to diameter $D\sqrt{(1-\alpha)}/2$. Thus, in this general form, the polymers occupy different, but nonoverlapping “territories” across the cylinder, which is why we call this approach “territorial” Flory theory.

Following eq. (3.1.3), we can simply rescale the free energy for linear chains given by eq. (3.2.5), and obtain that the total free energy depending on $n_0 = |d|/D$ and $n_{bl} = N/g$ scales like

$$\mathcal{F}(n_0, n_{bl}) = 2^{1/2\nu} \mathcal{F}_{lin}(n_0, n_{bl}), \quad (4.2.1)$$

where $\mathcal{F}_{lin}(n_0, n_{bl})$ is the free energy of two linear polymers each composed of $n_{bl}g/2$ monomers, that are confined to a cylinder of diameter D with an overhang of n_0g monomers. Note that the geometry splitting parameter α remains the same for rings and is given by eq. (3.2.7).

To determine the free energy difference between full overlap ($d = 0$) and a state with $|d| > 0$, we rewrite the free energy of the configuration with overhanging monomers in terms of $\delta = 2n_0/n_{bl} = 2N_0/N$, i. e. the fraction of overhanging beads compared to the length of the half ring that we consider, and subtract the free energy at full overlap:

$$\begin{aligned} \frac{\Delta\mathcal{F}(\delta, n_{bl})}{n_{bl}\mathcal{F}_{bl}} &= \frac{\mathcal{F}(\delta, n_{bl}) - \mathcal{F}(0, n_{bl})}{n_{bl}\mathcal{F}_{bl}} = \\ &= 2^{1/2\nu} [\delta + (1 - \delta)\alpha^{-1/2\nu} + (1 - \alpha)^{-1/2\nu}]. \end{aligned} \quad (4.2.2)$$

The behavior of the this free energy difference is shown in Fig. 4.7 and discussed in detail in section 4.2.3, however already here we underline that the free energy difference of rings has the same shape as the free energy difference of linear polymers with a pronounced peak at $\delta = 0$ and a minimum. The position of this minimum

CHAPTER 4. SEGREGATION OF RING POLYMERS UNDER CYLINDRICAL CONFINEMENT

corresponds to the equilibrium ratio of overhang and cylinder diameter, and the depth at the minimum is the free energy barrier that the polymers have to overcome when switching positions of the polymer ends. Obviously the free energy barrier for rings also scales like the free energy barrier of chains with an additional prefactor $2^{1/2\nu}$:

$$\mathcal{F}_{barrier}^r = 2^{1/2\nu} \mathcal{F}_{barrier}^{ch} = 2^{1/2\nu} \mathcal{F}_{min}^{ch} \frac{n_{bl}}{2}, \quad (4.2.3)$$

where \mathcal{F}_{min}^{ch} is the free energy difference per blob of a linear chain between the minimum and full overlap. Note the additional factor $1/2$ compared to eq. (3.2.10) from the section 3.2, which stems from the fact that here N denotes the full length of the ring, while in section 3.2 N denoted half the chain length.

The main scaling of the free energy barrier with the polymer length n_{bl} remains linear. Applying Kramers' or reaction-rate theory [97], the switching rate of rings is

$$k \sim \mathcal{D} \sqrt{\mathcal{F}_0'' \mathcal{F}_b''} e^{\beta \mathcal{F}_{barrier}^r}, \quad (4.2.4)$$

where $\beta = 1/k_B T$. \mathcal{F}_0'' and \mathcal{F}_b'' are the curvatures at the equilibrium distance and at the top of the barrier, respectively. Because of the linear rescaling of the free energy difference for rings with respect to linear chains the curvatures scale like $2^{1/2\nu}/(D^2 n_{bl})$. However, the diffusion constant remains the same as for linear chains $\mathcal{D} \sim 1/g$. Therefore the switching rate of rings is

$$k \sim \frac{2^{1/2\nu}}{D^2 n_{bl} g} \exp(-\beta \mathcal{F}_{barrier}^r) \sim \frac{2^{1/2\nu}}{D^2 N} \exp\left(-\beta 2^{1/2\nu} \mathcal{F}_{min}^{ch} \frac{N}{2g}\right). \quad (4.2.5)$$

The induction time is the mean first passage time of polymers switching roles, which we compute from this as

$$t_{in} \sim \frac{1}{k} \sim D^2 N \exp\left(\beta 2^{1/2\nu} \mathcal{F}_{min}^{ch} \frac{N}{2g}\right). \quad (4.2.6)$$

As in the case of chains, the induction time scales exponentially in the length of the polymers, and dominates the total segregation time for long polymers.

4.2.2 Simulation details

To investigate the induction phase and compute the induction time of two segregating polymers under cylindrical confinement we perform molecular dynamics simulations in ESPReso following the approach presented for linear chains in section 3.2.2. We consider only half rings of $N/2$ beads. These half rings are modeled in the same manner as described in section 4.1.2 using the bead-spring model with initial cross-linked configuration. However, we fix the positions of the beads corresponding to the middle of the full rings to prevent diffusion of the total center

of mass. Next to these fixed beads we create a wall on the side opposite to the polymers to mimic the presence of the second half chain. This is important, because otherwise the polymers would back-bend and simply segregate into left and right halves around this fix point. After equilibration of the system we remove the cross-linking bonds and record the signed distance d between the outermost beads of the chains for 1,000,000 time steps. In this set of simulations we also vary the polymer length and diameter of the cylinder $D = 4, 5, \dots, 13$. However, in order to maintain good statistics for all effective blob numbers n_{bl} , we adapt the polymer length to the diameter as $N = n_{bl}g$ for $n_{bl} = 1, 2, \dots, 20$, where $g = (D/a)^{1/\nu}$, $\nu = 0.59$ is the Flory exponent and $a = 1.31$ is the effective persistence length [94]. This results in ring lengths between 6 and 1000 beads.

4.2.3 Results

In order to demonstrate the validity of the territorial renormalized Flory approach in treating systems of multiple overlapping chains, we compute the free energy landscape of switching. In Fig. 4.7 we plot an exemplary free energy difference

$$\Delta\mathcal{F}(\delta) = -k_B T [\ln P(\delta) - \ln P(0)] \quad (4.2.7)$$

as a function of the ratio $\delta = 2N_0/N$ of overhanging beads to beads in the half chain, which we compute from the probabilities $P(\delta)$ observed during the simulations. The

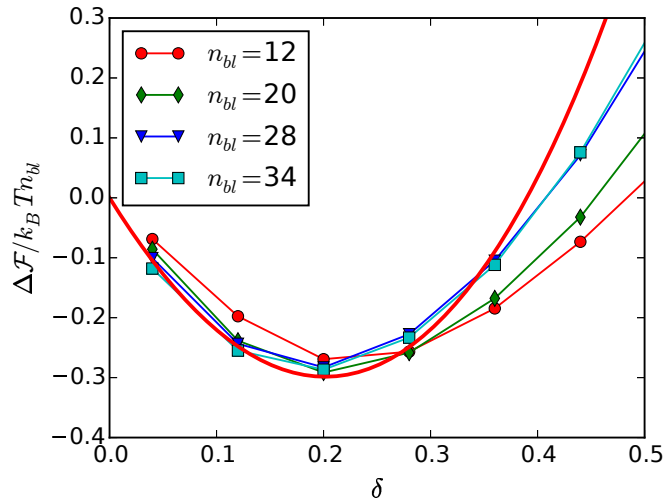


Figure 4.7: The free energy as a function of $\delta = 2N_0/N$ for ring polymers trapped in a cylinder of diameter $D = 6$. The number of monomers in rings varies from $n_{bl} = 12$ to 34 blobs. The red line denotes the theoretical prediction given by eq. (4.2.2) with $\mathcal{F}_{bl} = 5k_B T$.

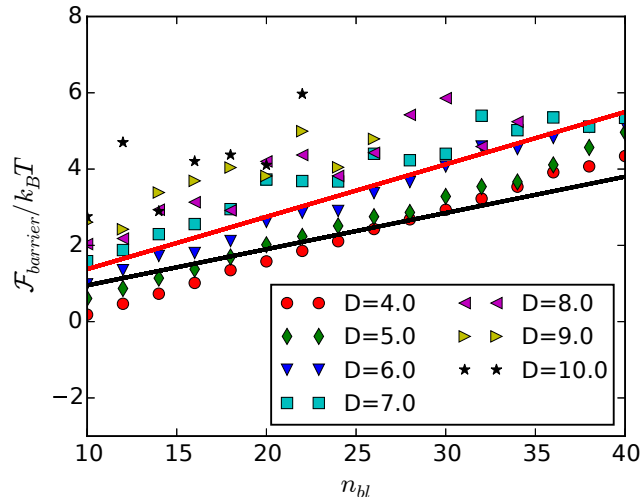


Figure 4.8: Free energy barrier $\mathcal{F}_{barrier}$ as a function of the number of blobs $n_{bl} = N/g$. Different symbols correspond to different cylinder diameters D . The red line is the theoretical prediction for ring polymers given by eq. (4.2.3) with the free energy per chain taken from Ref. [96], the black line is corresponding prediction for linear chains [96].

free energy landscape between full overlap and the equilibrium position is well predicted by our theory, only for large numbers of overhanging beads deviations occur. This is not unexpected, since this means that for the overhanging chain, only few beads are left for the overlap region, so that the chain becomes fairly stretched and the blob picture breaks down. Again, there are no qualitative differences between rings and chains as reported in Ref. [96], only the free energy per blob for rings is larger by a factor of $2^{1/\nu}$ due to the additional confinement.

To estimate the free energy barrier that the rings have to overcome to switch their roles, we plot the free energy difference between minimum and the local maximum at $\delta = 0$ as a function of the number of blobs $n_{bl} = N/g$ in Fig. 4.8. As expected, the free energy barrier grows rapidly with the polymer length. We found good agreement between the simulation data and the theoretical prediction eq. (4.2.3) when inserting the free energy barrier per blob of a linear chain as reported in Ref. [96] and applying the additional factors for rings.

In the simulations we also measured the switching rate of the polymer ends by counting how many times d changes its sign. These data are shown in Fig. 4.9 as a function of the polymer length in terms of $n_{bl} = N/g$. The red line corresponds to the theoretical prediction eq. (4.2.5), where the free energy difference per blob for linear chains $\mathcal{F}_{min}^{ch} = 0.19k_B T$ was taken from Ref. [96]. Again, there is very good agreement between simulation and theory, and the exponential decay of the switching rate with polymer length is clearly visible.

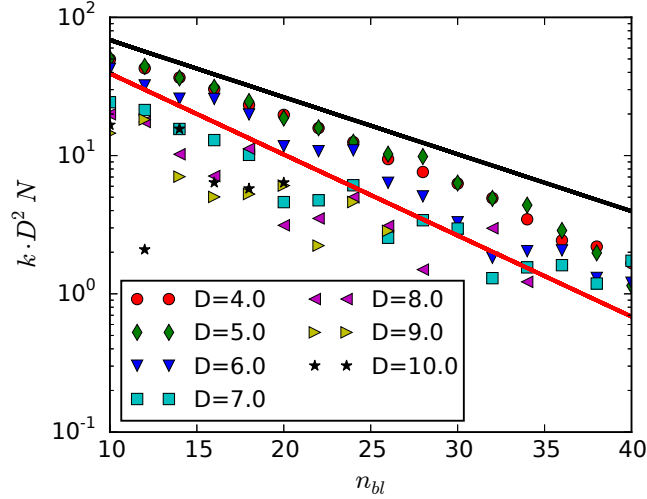


Figure 4.9: Rate of switching of k rescaled by $1/DN^2$ versus the number of blobs $n_{bl} = N/g$. Different symbols correspond to different cylinder diameters D . The red line is the theoretical prediction from eq. (4.2.5), the black line the corresponding prediction for linear chains [96].

Fig. 4.10 shows the resulting induction time for ring polymers as measured in the simulations of segregation process reported in section 4.1.2. By rescaling with a factor of D^2N , all data fall on a single master curve as predicted by eq. (4.2.6). Here we use the same value of the free energy barrier per blob $\mathcal{F}_{min}^{ch} = 0.19k_B T$ as reported in Ref. [96] for linear polymers. As for linear chains, the induction time for rings increases exponentially with the chain length. This proves that the different topology of rings and chains has no qualitative influence on the induction time. The only difference is quantitative, in the sense that the exponential growth of the induction time with the polymer length is slower by a factor of $2^{1/2\nu-1} \approx 0.9$ compared than for linear chains of the same length. Thus the induction time for long rings is much smaller than the one of equally sized linear chains, but still much longer than the actual segregation time.

The deeper reason that the ring topology almost does not play a role lies in the “territorial” behavior of confined polymers. A ring in confinement gets compressed and acts like two parallel polymers that cannot segregate. Otherwise, the two half-rings do not entangle and occupy more or less tube-like territories. Adding a second or more rings or linear chains does not alter this picture: each chain occupies a distinct tube and barely interacts with the other chains apart from reduction of its tube.

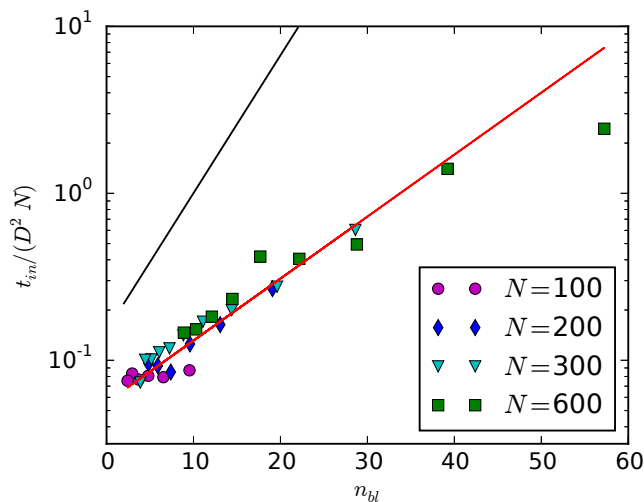


Figure 4.10: Induction time of ring polymers rescaled by the DN^2 as a function of $n_{bl} = N/g$. Symbols correspond to the simulation data for systems with different total number of monomers N per ring. The red line is the theoretical prediction given by eq. (4.2.6), the black line is the corresponding prediction for linear chains [96].

4.3 Conclusion

In this chapter, we have investigated the entropic segregation of two ring polymers confined in an open cylinder. The main theoretical approach that we have used through out this chapter is the territorial renormalized Flory approach which turned out to be very powerful for studying overlapping polymers in cylindrical confinement. In this approach, rings are treated as two overlapping linear chains, and the free energy of any number of overlapping chains is simply the sum of the free energies of the underlying chains. This is a consequence of the fact that polymers in cylindrical confinement tend to occupy individual tubes that do not entangle. Therefore, the only interaction is the sharing of accessible volume.

Our computations do not only confirm earlier results [6] that ring topology facilitates segregation, but show that the segregation time scale of rings is strictly proportional to the one of linear chains with the same number of monomers. The induction time grows slower with the polymer length, but still exponentially. Therefore, the induction phase for large rings takes much less time compared to chains, but still much longer than the segregation itself. Thus, it dominates the overall segregation time scale for long polymers.

All our theoretical findings are well supported by molecular dynamics computer simulations. This does not only validate our theory, but shows the broad applicability of the territorial renormalized Flory theory for studying systems with any

number of overlapping polymers of different length in confinement.

Chapter 5

Compression of polymers under cylindrical confinement

A significant effort has recently been made in understanding a relationship between intra- and interpolymer ordering, discussed in sec. 2.8.3, and segregation tendency of self-avoiding polymers confined in a cylinder of finite size, since it has a relevance to chromosome organization and segregation in elongated bacteria [3, 5]. It has been observed that greater asymmetry of the confining cylinder (i.e. a more elongated cylinder) enhances segregation tendency, and the polymers are the most miscible in cylinders where the aspect ratio of cylindrical axes is of order of unity [3, 5]. Another important parameter which influences the chain miscibility is the volume fraction of monomers. High volume fraction leads to more compact packing of polymers inside the cylinder, which in turn increases miscibility. Jung and coworkers constructed the effective miscibility diagrams [3, 5] which couple the aspect ratio of the cylindrical confinement to the volume fraction of monomers and give the explicit answer on the degree of polymer miscibility measured in terms of the overlapping region of polymers. As known, overlap of polymers costs free energy, therefore, the polymer miscibility depends on the free energy barrier between two states where the polymers are fully mixed and where the polymers are separated the most.

In this chapter, we investigate the behavior of polymers confined in a cylinder of finite length at relatively low volume fraction and various aspect ratios of cylindrical axes. Using molecular dynamics simulations, we compute the free energy barrier between complete mixing of polymers and at their maximum separation. We also estimate the free energy theoretically using the renormalized Flory approach.

5.1 Conventional Brute Force Simulations

We consider two self-avoiding linear polymers consisting of N monomers of size a confined in a cylinder of diameter D . In contrast to the previous two chapters, the

5.1. CONVENTIONAL BRUTE FORCE SIMULATIONS

cylinder is of finite length L . The excluded volume of monomers and the interactions between the monomers and walls of the cylinder are modeled by the Weeks-Chandler-Andersen potential (see eq. (2.5.2)). The monomers are linked by FENE bonds (see eq. (2.5.3)) with the spring constant $k_F = 10k_B T/a^2$ and maximal stretching $r_F = 2a$.

To obtain the free energy landscape of two polymers and estimate the free energy barrier of fully overlapping and nonoverlapping polymers we perform conventional brute force molecular dynamics simulations using the simulation package ESPResSo [68, 98] for different polymer lengths $N = 100, 200$ and 300. We fix the total volume fraction of monomers at $\phi = 2Nv_0/V_{cyl} = 0.076$ which is typical for modeling *E. coli* chromosomes [8, 99, 100]. Here, $v_0 = \pi a^3/6$ is the volume of one monomer and $V_{cyl} = \pi L D^2/4$ denotes the volume of the cylinder. Keeping the volume fraction constant, we consider different cylindrical geometries by varying the aspect ratio of the cylinder L/D with $D = 4.0, 5.0, \dots, 20.0$. Thus, in the limiting cases we have a very long cylinder with small diameter and a disk-like confinement. Note, that throughout this chapter all the lengths are measured in units of one monomer size.

We start the simulations with a snake-like initial configuration of the polymers as shown in Fig. 5.1. For simplicity, each polymer occupies half of the cylinder along the radial cylindrical axis. Since the length of the cylinder is usually smaller than the length of the perfectly stretched polymer ($L < Na$), the first L/a monomers construct a linear row along the longitudinal axis of the cylinder and the rest of the monomers, which did not fit in this row, go to the second row parallel to the first one. This procedure is repeated until all the monomers are packed into a cylinder. Note that the distance between the rows is always equal to one monomer size in order to prevent breaking the bonds between the last and first monomers of two consecutive rows. After equilibration of the system, we record the distance between the polymers' centers of mass R_{c2c} during 10^6 time steps $\delta t = 0.01$.

Fig. 5.2 shows the distance between the polymers' centers of mass R_{c2c} along the longitudinal axis of the cylinder measured during the brute force simulations for different aspect ratios L/D of the cylinder. For long cylinders of small diameter

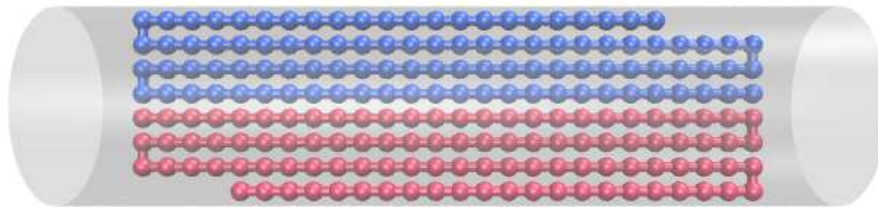


Figure 5.1: Simulation snapshot of the initial snake-like configuration of two polymers composed of $N = 100$ monomers in a finite cylinder of diameter $D = 8.0$.

CHAPTER 5. COMPRESSION OF POLYMERS UNDER
CYLINDRICAL CONFINEMENT

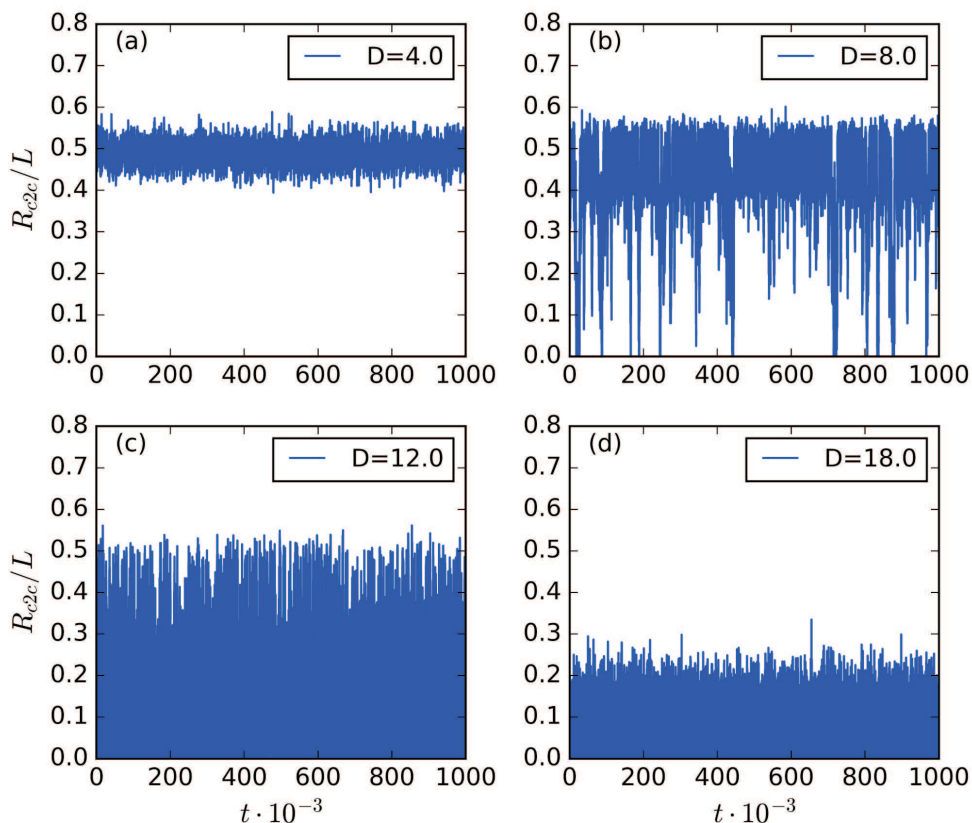


Figure 5.2: Distance between the polymers' centers of mass rescaled by the length L of the cylinder versus time t obtained in the brute force simulations for polymers composed of $N = 100$ monomers. (a) The diameter of the cylinder is $D = 4.0$, the aspect ratio $L/D=27.4$. Overlap of polymers is not detected during simulations. (b) The diameter of the cylinder is $D = 8.0$, the aspect ratio $L/D = 3.4$. Polymers mix readily, however, prefer to segregate. (c) The diameter of the cylinder is $D = 12.0$, the aspect ratio $L/D = 1.0$. (d) The diameter of the cylinder is $D = 18.0$, the aspect ratio $L/D = 0.3$. (c)-(d) Polymers are mixed along the longitudinal cylindrical axis.

the distance between the centers of mass stays around $0.5L$ and never reaches zero (see Fig. 5.2 (a)). This means that each polymer occupies one half of the cylinder along the longitudinal axis and they absolutely resist mixing due to high free energy cost for the overlap. When the aspect ratio L/D decreases, the cylinder becomes shorter and wider, but is still elongated. In this case, the distance between the centers of mass starts approaching zero indicating that the polymers mix more readily (compare Fig. 5.2 (b)). This is a signature that the free energy difference between the mixed and segregated states of the polymers diminishes, however, it does not drop to zero, since the polymers still prefer to segregate. As soon as the

5.1. CONVENTIONAL BRUTE FORCE SIMULATIONS

aspect ratio is close to unity, it is very likely to find the polymers in the mixed state along the longitudinal axis of the cylinder (see Fig. 5.2 (c)). However, the distance between the centers of mass can still reach $0.5L$ enough frequently. Decreasing the aspect ratio below unity ($L/D < 1$), where the cylinder resembles a disk, changes the main axis of the cylinder from the longitudinal axis to the radial one. In this case, the polymers still tend to segregate, but along the radial axis that diminishes the deviation of longitudinal R_{c2c} from zero (compare Fig. 5.2 (d)).

To summarize the spatial organization of the polymers, we compute the most probable distance between the centers of mass R_{c2c} along the longitudinal axis of the cylinder for different aspect ratios of the cylinders L/D and plot it rescaled by the length of the cylinder L as shown in Fig. 5.3. One can note that the most probable distance between the centers of mass is independent of polymer length N and only aspect ratio changes its magnitude. For the cylinders with aspect ratio $L/D > 6$, the polymers prefer to stay separated with the distance $R_{c2c} = 0.5L$, meaning that the polymers do not overlap and each of them occupies one half of the cylinder despite the longitudinal compression. This distance decreases by 10% with the following decrease of the aspect ratio down to $L/D \approx 3$. The polymers start overlapping in such cylinders, however, the overlapping region is rather small and does not exceed a distance equal to three monomer sizes. The length of the overlapping region increases for cylinders of smaller aspect ratio $L/D < 3$, and eventually the polymers become totally miscible so that $R_{c2c} = 0$. Such a spatial organization of the polymers is consistent with the miscibility diagram (see Refs. [3, 5]) of linear polymers at the

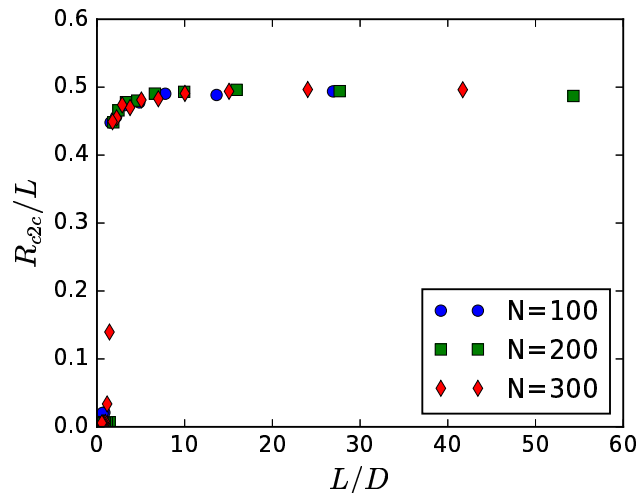


Figure 5.3: The most probable distance between the polymers' centers of mass R_{c2c} rescaled by the length of the cylinder as a function of the cylindrical aspect ratio L/D . Different symbols correspond to different polymer lengths.

volume fraction $\phi = 0.076$.

5.2 Forward Flux Sampling Simulations

As it has been shown in the previous section, in the conventional brute force simulations the polymers do not always come close enough to each other to sample all possible polymer separation (for example, see Fig. 5.2(a)). Obviously, during the brute force simulations the polymers spend most of the time in the state with the lowest free energy, which corresponds to the polymer separation $R_{c2c} \approx L/2$. Due to the high free energy barrier, especially for long cylinders with small diameter, the polymers stay separated with the distance between the centers of mass $R_{c2c} \approx L/2$ and are not found in the mixed state where $R_{c2c} = 0$ as shown in the next section. The lack of data at small polymer separations does not allow us to compute the free energy landscape of the polymers depending on their separation. To fill this gap, we use the Forward Flux Sampling (FFS) method discussed in sec. 2.7.2. This method can sample the whole phase space along the reaction coordinate, which is the distance between the polymers' centers of mass R_{c2c} in our case. To run FFS simulation, we employ the software package FRESHHS [84, 85]. To start the simulations, one needs to choose the initial interface. In principle, the initial interface can be set to the largest possible separation of polymers $R_{c2c} \approx L/2$, which has been determined in the brute force simulations. However, the histogram analysis of the trajectories of the centers of mass computed in the brute force simulations shows that the polymers are found enough frequently at slightly closer distances up to $R_{c2c} = R_{c2c}^*$ where the free energy is $3k_B T$ higher than at the largest separation $R_{c2c} \approx L/2$. Therefore, we shift the initial interface to R_{c2c}^* , but still ensure a good initial flux of trajectories through the initial interface. The parameters of the system, such as the length of the polymers N , the diameter of the cylinder D and the position of the initial interface R_{c2c}^* are listed in Tab. 5.1. All the next interfaces are placed using the optimal automatic interface placement algorithm implemented in FRESHHS [85]. Collecting the trajectories of the polymers' centers of mass, which cross every interface 100 times, and analyzing them by the histogram method discussed in sec. 2.7.2, we obtain the free energy landscape for the polymer separation $0 \leq R_{c2c} \leq R_{c2c}^*$. We carry out 10 independent FFS simulations to provide good statistics. Merging the free energy landscapes obtained from the brute force simulations to those obtained from the FFS simulations, we find the free energy landscape shown in Fig. 5.4 for the full range of the polymer separation which covers both situations, namely, fully overlapping polymers with $R_{c2c} = 0$ and the most segregated state $R_{c2c} \approx L/2$.

N=100	D	4.0	5.0	6.0					
	R_{c2c}^*	46	29	19					
N=200	D	4.0	5.0	6.0	7.0	8.0			
	R_{c2c}^*	97	63	42	30	21			
N=300	D				7.0	8.0	9.0	10.0	11.0
	R_{c2c}^*				47	35	24	16	14

Table 5.1: System parameters for the FFS simulations.

5.3 Free energy of polymers

The free energy landscapes of two polymers trapped in a finite size cylinder are obtained using two methods depending on the type of simulations. For the brute force simulations in which the sampling of the polymer separation at $R_{c2c} = 0$ has been achieved with good statistics, we use the probability distributions of the distance between the polymers' centers of mass $P(R_{c2c})$ to compute the free energy as follows

$$\beta\Delta\mathcal{F}(R_{c2c}) = -\ln(P(R_{c2c})) + \ln(P(R_{c2c} = 0)). \quad (5.3.1)$$

For the systems listed in Tab. 5.2, the free energy landscapes are obtained by joining two methods and can be expressed as

$$\beta\Delta\mathcal{F}(R_{c2c}) = \begin{cases} \beta\Delta\mathcal{F}_{FFS}(R_{c2c}), & 0 \leq R_{c2c} \leq R_{c2c}^* \\ -\ln(P(R_{c2c})) + \beta\Delta\mathcal{F}_{FFS}(R_{c2c}^*), & R_{c2c} > R_{c2c}^*. \end{cases} \quad (5.3.2)$$

where $\beta\Delta\mathcal{F}_{FFS}(R_{c2c})$ denotes the free energy difference obtained from the FFS simulations using eq. (2.7.19) according to the method based on calculations of the weighted histograms of trajectories as described in sec. 2.7.2. In the case where $R_{c2c} > R_{c2c}^*$, we again use the probability distributions of R_{c2c} collected during the brute force simulations, but shift the logarithms of them by the free energy $\beta\Delta\mathcal{F}_{FFS}(R_{c2c}^*)$ to determine the depth of the free energy correctly.

Fig. 5.4 depicts the free energy landscapes calculated using eq. (5.3.1) and (5.3.2) for polymers composed of $N = 100$ monomers and trapped in cylinders of different aspect ratios L/D . For elongated cylinders where the aspect ratio is larger than unity ($L/D > 1$), the free energy landscape has a pronounced maximum at $R_{c2c} = 0$ where the polymers are in full overlap, and then decays with an increase of the distance between the polymers' centers of mass until it reaches its minimum at the polymer separation $R_{c2c} \approx 0.5L$. Since each polymer seeks to occupy one half of the cylinder, the polymers prefer to segregate due to the high free energy cost for

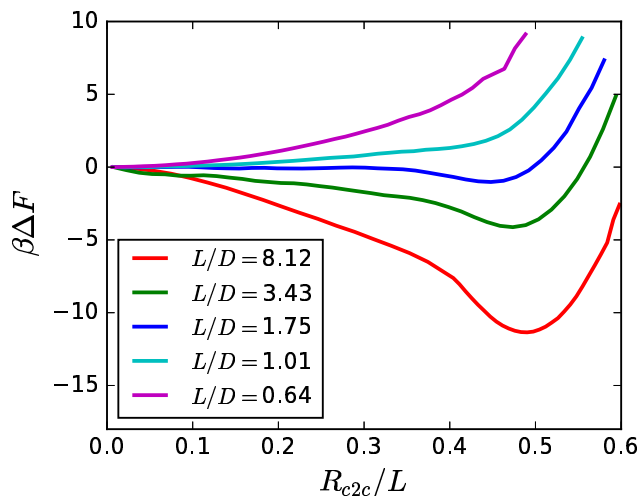


Figure 5.4: Free energy landscapes of two polymers as a function of the distance between the centers of mass R_{c2c} along the longitudinal axis of the cylinder rescaled by the length of the cylinder L . Polymers are composed of $N = 100$ monomers each and trapped in a cylinder of diameter D and length L .

overlapping. The further increase of the free energy at $R_{c2c} > 0.5L$ is induced by the presence of the impenetrable walls which close the cylinder at both its ends. However, with decreasing the aspect ratio the depth of the minimum diminishes and the position of the minimum moves a bit closer to zero as shown in Fig. 5.3. This means that the polymers become slightly more miscible along the longitudinal axis of the cylinder and have a small overlapping region as discussed in the previous section. Finally, at $L/D < 1$, the free energy landscape changes its shape so that the minimum is located at $R_{c2c} = 0$, indicating that the polymers have reached the highest level of miscibility along the longitudinal axis. However, even for $L/D < 1$ the polymers still tend to segregate because of their self-avoidance. In this case, the polymers segregate along the radial axis, since the main axis has changed from the longitudinal axis to the radial one.

5.4 Free energy barrier

The height of the free energy barrier $\mathcal{F}_{barrier}$ which two separated polymers have to overcome in order to mix in elongated cylinders was computed numerically as the depth of the minimum in the free energy landscapes (see Fig. 5.4) and is shown in Fig. 5.5 for a wide range of the aspect ratio L/D of the cylinder. The highest free energy barrier is observed for the longest cylinders. Decreasing the aspect

ratio, the polymers become more compressed longitudinally, but they still resist mixing, since the polymers have to pay a free energy penalty for overlap. However, being longitudinally compressed is also energetically expensive. This cost grows with increasing longitudinal compression for shorter cylinders, leading to a decrease in the free energy barrier which disappears once the aspect ratio L/D reaches unity.

To estimate the height of the free energy barrier $\mathcal{F}_{barrier}$ theoretically, one needs to determine the free energy of two overlapping polymers $\beta\mathcal{F}_{mix}$ and the free energy of two segregated polymers $\beta\mathcal{F}_{seg}$ and then take their difference:

$$\beta\mathcal{F}_{barrier} = \beta\mathcal{F}_{mix} - \beta\mathcal{F}_{seg}. \quad (5.4.1)$$

We calculate these free energies using the renormalized Flory approach (for more details see sec. 2.3.4 and Ref. [41, 61]). According to this approach the free energy of a single polymer composed of N monomers depends on the polymer extension l along the cylinder of diameter D as follows

$$\beta\mathcal{F}(l, N, D) \sim A \frac{l^2}{(N/g)D^2} + B \frac{D(N/g)^2}{l}, \quad (5.4.2)$$

where $g = (D/a)^{1/\nu}$ is the number of monomers per blob of size D with the Flory exponent $\nu = 0.6$. The constants A and B are nonuniversal constants. The renormalized Flory approach gives an accurate scaling of the free energy of polymers in

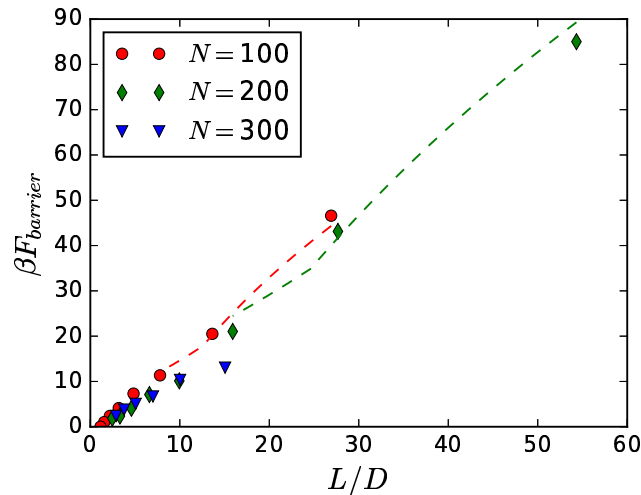


Figure 5.5: Height of the free energy barrier $\beta\mathcal{F}_{barrier}$ as a function of the cylindrical aspect ratio L/D . Different symbols correspond to simulation data. The dashed curves are the theoretical predictions given by eq. (5.4.6). Colors of both symbols and theoretical curves match to the color scheme given for different polymer lengths.

CHAPTER 5. COMPRESSION OF POLYMERS UNDER CYLINDRICAL CONFINEMENT

equilibrium where a polymer expands to its equilibrium length $L_{eq} = Na^{1/\nu}D^{1-1/\nu}$. However, as it has been discussed in Chapter 2, it is also valid for polymers compressed up to one half of the polymer's equilibrium length [5, 41], that allows us to apply this approach to our longitudinally compressed polymers whose length l is still larger than one half of the equilibrium length:

$$l > \frac{L_{eq}}{2}. \quad (5.4.3)$$

When two polymers are separated so that they do not overlap, each of the polymers occupies one half of the cylinder $l = L/2$ for the considered here systems. In this case, the free energy of such polymers can be written as

$$\beta\mathcal{F}_{seg} = 2\beta\mathcal{F}\left(\frac{L}{2}, N, D\right). \quad (5.4.4)$$

From the condition (5.4.3) follows that eq. (5.4.4) is applicable to polymers confined in a cylinder whose length is $L > L_{eq}$. Since the volume fraction of monomers is fixed in our systems, the length of the cylinder can be expressed as $L = 4Na^3/(3D^2\phi)$. Note that both the length of the cylinder and the equilibrium length of one polymer scales linearly with N . This leads to the condition that the diameter of the cylinder should not exceed $D = 6.0$ at the volume fraction $\phi = 0.076$, independently of the number of monomers N .

To calculate the free energy of overlapping polymers where $R_{c2c} = 0$, we split the polymers' territories by trapping the polymers in imaginary subcylinders with diameter $D/\sqrt{2}$ as discussed in Chapter 3 for linear polymers in an infinitely long cylinder. The lengths of the subcylinders coincide with the length L of the initial cylinder. Since the confining cylinders considered in this chapter are of finite length, there exist two possible situations depending on the length of the cylinder. The cylinder can be so long that each polymer expands to its equilibrium length $L_{eq}^{sub} = Na^{1/\nu}(D/\sqrt{2})^{1-1/\nu} = L_{eq}2^{(1-\nu)/2\nu}$ in the subcylinder of reduced diameter. Otherwise $L < L_{eq}^{sub}$, the polymers are compressed to the length equal to the length of the cylinder ($l = L$). Therefore, the free energy of polymers in overlap also depends on the length of the cylinder and can be written as

$$\beta\mathcal{F}_{mix} = \begin{cases} 2\beta\mathcal{F}\left(L_{eq}2^{(1-\nu)/2\nu}, N, \frac{D}{\sqrt{2}}\right), & \text{if } L \geq L_{eq}2^{(1-\nu)/2\nu} \\ 2\beta\mathcal{F}\left(L, N, \frac{D}{\sqrt{2}}\right), & \text{otherwise.} \end{cases} \quad (5.4.5)$$

After the substitution of eq. (5.4.4) and eq. (5.4.5) into eq. (5.4.1) we obtain the free energy barrier in the following form:

$$\beta\mathcal{F}_{\text{barrier}} = \begin{cases} 2 \left[A \left(\frac{N}{g} 2^{1/2\nu} - \frac{L^2}{4(N/g)D^2} \right) + B \left(\frac{N}{g} 2^{1/2\nu} - \frac{2D(N/g)^2}{L} \right) \right], \\ \text{if } L \geq L_{eq} 2^{(1-\nu)/2\nu} \\ 2 \left[A \frac{L^2}{(N/g)D^2} \left(2^{1-1/2\nu} - \frac{1}{4} \right) + B \frac{D(N/g)^2}{L} (2^{(2-\nu)/2\nu} - 2) \right], \\ \text{otherwise.} \end{cases} \quad (5.4.6)$$

We also plot the theoretical predictions for the height of the free energy barrier given by eq. (5.4.6) in Fig. 5.5 for cylinders of diameter $D \geq 6.0$ where the Flory approach is applicable for estimating the free energy of polymers in the segregated state. We found a good agreement between the free energy determined in computer simulations and the theoretical predictions using the constants $A = 0.41$ and $B = 0.49$ as fitting parameters to the simulation data. The theoretical predictions confirm that the free energy barrier depends not only on the geometric parameters of the cylinder, but also on the polymer length N . The change in slope of the theoretical curves occurs at the aspect ratio $L/D = N(3\phi)^{1/(3\nu-1)} 2^{(1+3\nu)/2(1-3\nu)}$, below which the polymers are compressed longitudinally even in overlap, that corresponds to the crossover from the upper case in eq. (5.4.6) to the lower one. Despite the obtained agreement between the theory and the simulation data, the complex dependence of $\beta\mathcal{F}_{\text{barrier}}$ on the aspect ratio L/D (see eq. (5.4.6)) does not give a straightforward scaling for the free energy barrier with the aspect ratio which looks like linear at the first glance.

However, in wider cylinders ($6.0 < D \lesssim 11.0$) which are still elongated ($L/D \gtrsim 3$), we observe that the polymers also resist to mix. Moreover, this resistance is so strong that the polymers prefer to stay separated occupying a half of the cylinder without overlapping as shown in Fig. 5.3 which depicts the most probable distance between the centers of mass R_{c2c} as a function of the aspect ratio L/D . Therefore, one can try to estimate the free energy $\beta\mathcal{F}_{\text{seg}}$ of the separated polymers using eq. (5.4.4). Thus, the free energy barrier can still be calculated using eq. (5.4.6) for such cylinders. In Fig. 5.6 we plot the free energy barrier for the aforementioned cylinders and the theoretical predictions given by eq. (5.4.6). The constants A and B are again used as the fitting parameters. Since the free energy barrier depends not only on the aspect ratio L/D , but also on the number of monomers N , which compose the polymers, the fitting of eq. (5.4.6) to the simulation data has been done for each polymer length independently, where we obtained the following fitting constants: $A = 0.64$ and $B = 0.35$ for $N = 100$, $A = 0.41$ and $B = 0.18$ for $N = 200$, $A = 0.26$ and $B = 0.07$ for $N = 300$. With these fitting parameters we found a good agreement between the free energy barrier computed in simulations and theoretical predictions based on the renormalized Flory approach. However, the spread of the

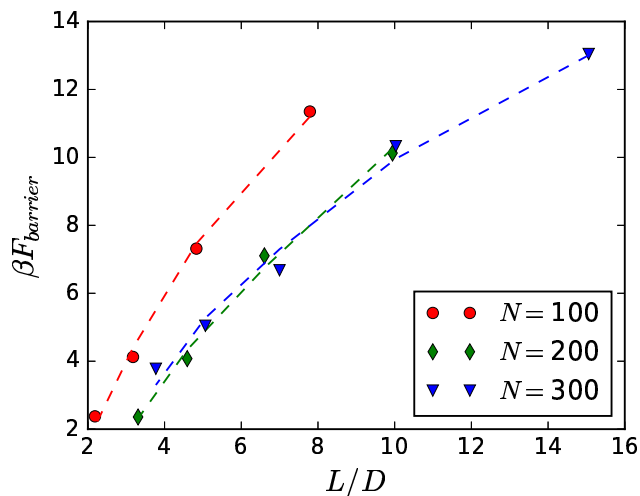


Figure 5.6: Height of the free energy barrier $\beta\mathcal{F}_{\text{barrier}}$ as a function of the cylindrical aspect ratio L/D , where the diameter of the cylinder is in range $6.0 < D < 11.0$. Different symbols correspond to simulation data. The dashed curves are the theoretical predictions given by eq. (5.4.6). Colors of both symbols and theoretical curves match to one color scheme given for different polymer lengths.

fitting parameters A and B for different N indicates that the Flory approach is not accurate enough to estimate the free energy of polymers in such cylinders. This is caused by the fact that the polymers are so strongly longitudinally compressed that the length of each polymer along the cylinder becomes smaller than one half of its equilibrium length. As it was shown by Jun and coworkers in Ref. [41], one can not rely on the renormalized Flory approach for such compressed polymers.

5.5 Conclusion

In this chapter, we investigated the relationship between the spatial organization of two linear self-avoiding polymers confined in a cylinder of finite length for different aspect ratios of the cylinder and the polymer miscibility. At the relatively low volume fraction of monomers $\phi = 0.076$ considered here, the polymers tend to segregate, and each of them occupies one half of the cylinder along the longitudinal axis in elongated cylinders ($L/D > 1$) or along the radial axis in disk-like cylinders ($L/D < 1$). Such a behavior of polymers is consistent with the miscibility diagram constructed for linear polymers in Ref. [3, 5]. The resistance of polymers to mix is induced by high free energy cost for overlapping. Combining both brute force and FFS simulations, we computed the free energy barrier that two separated polymers have to overcome in order to be found in the fully mixed state, where the positions

of the polymers' centers of mass along the longitudinal axis of the cylinder coincide. We showed that this free energy barrier decays with a decrease of the degree of the cylindrical elongation that is also confirmed by the theoretical predictions based on the renormalized Flory approach. Moreover, this theoretical approach can be applied to estimate the free energy barrier in relatively short, but still elongated cylinders, where the polymers are already significantly compressed along the longitudinal axis of the cylinder. However, the theoretical estimation in this case is less accurate than for narrow and more elongated cylinders.

Our findings have a relevance to chromosome segregation in elongated bacteria. Since the entropic segregation is an essential part of the chromosome segregation, a high free energy barrier causes stronger repulsion between the chromosomes while they are segregating from the fully mixed state. On the other hand, when the polymers have segregated, the free energy barrier keeps them separated while the wall which will separate two newborn cells is under construction.

In future, our work can be extended by computing the free energy barriers for lower and higher volume fractions of monomers and adding them to the miscibility diagram (see Ref. [3, 5]). This will make the miscibility diagram more detailed: it can be used not only as a map for the spatial organization of polymers, but, in addition, contain the information about the energetic cost of such an organization.

Chapter 6

Effective potential of linear polymers confined in a slit

In this chapter we compute the effective potential of two linear polymers using the method of Widom insertions [77]. This method is unbiased and, therefore, does not require a guess for an initial bias potentials. In addition, it does not depends on the diffusion of the polymers in contrast to brute force simulations or simulations based on the advanced sampling techniques and it is relatively easy to implement. All this advantages make the method of Widom insertions favorable for obtaining the effective potential of polymers in a slit.

The effective potential gives a precise answer to the question how strong polymers interact with each other depending on the distance between the polymers' centers of mass. This allows one to estimate the polymers' repulsion and provides a background for understanding the segregation process of polymers confined in a slit.

6.1 Simulation model

According to the method of Widom insertion which is described in section 2.7.3, first one needs to generate a large number of equilibrium configurations of a single polymer in a slit. To this end, we employ molecular dynamics simulations using the simulation package ESPResSo [68, 98]. The polymer is modelled using the bead-spring model (see section 2.5). The monomers of size $a = 1$ interact via the Weeks-Chandler-Andersen potential (see eq. (2.5.2)) and are linked by FENE bonds (see eq. (2.5.3)) with the spring constant $k_F = 10k_B T/a^2$ and maximal stretching $r_F = 2a$. The polymer is placed between two infinite walls separated by the distance H . The interactions between the monomers and walls are described by the same WCA potential which is used for modelling the excluded volume of monomers. We employ a velocity Verlet integrator with fixed time step 0.01 to propagate the system. The temperature of the system is kept constant using the Langevin thermostat with

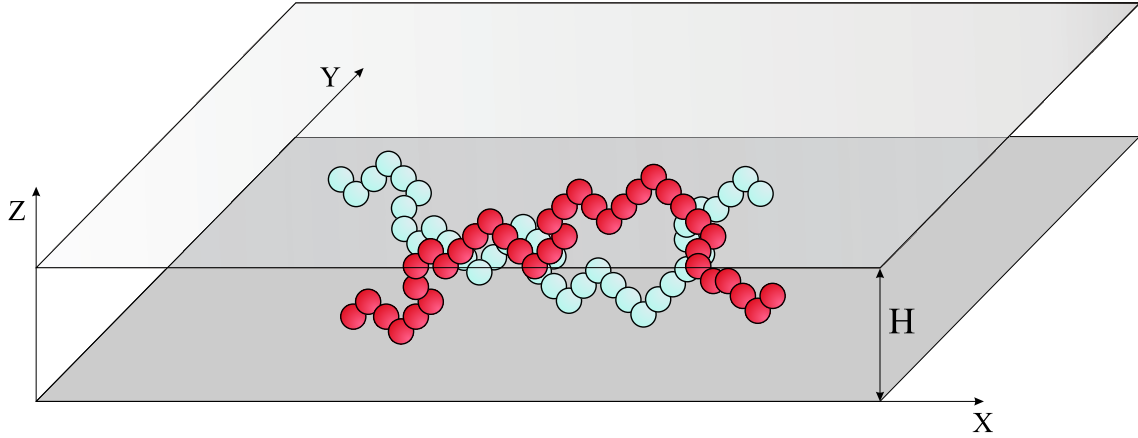


Figure 6.1: Two overlapping polymers confined in a slit of width H .

dimensionless friction 1.

We start simulations with a perfectly stretched configuration of the polymer. After equilibrating the polymer during 10^6 time steps, we store its configurations during $2 \cdot 10^7$ time steps with the interval 10^5 time steps. Thus, we obtain $N_{conf} = 2,000$ equilibrium configurations which we use to calculate the effective potential depending on the distance between the polymers' centers of mass as follows. When the equilibrium configurations are prepared, we take two different configurations and place them between the walls so that the polymer' centers of mass in the XY -plane coincide (see Fig. 6.1), and compute the Boltzmann factor of the inter-polymer interactions. Then we shift one of the polymers by the distance of half monomer size $a/2$ along the X axis keeping the position of the second polymer unchanged and again compute the Boltzmann factor of inter-polymer interactions in this state. This way we ensure that the centers of mass are displaced by half monomer size $a/2$ in XY plane. This procedure was repeated until the polymers become so distant from each other that they do not interact anymore. Considering all possible pairs of the equilibrium configurations of single polymer which is $N_{conf}(N_{conf} - 1)/2 = 1,999,000$, and taking the ensemble average of the Boltzmann factor, we obtain the effective potential V_{eff} of two polymers confined in a slit as follows

$$\beta V_{eff}(R_{c2c}) = -\ln\langle e^{-\beta\Delta U(R_{c2c})}\rangle, \quad (6.1.1)$$

where $\beta = 1/k_B T$ and R_{c2c} is the distance between the centers of mass. $\Delta U(R_{c2c})$ denotes the inter-polymer potential energy.

The simulations were performed for polymers composed of $N = 50$ and 100 monomers in a slit of width $H = 3.0, 4.0, 5.0$ and 6.0 in the units of one monomer size.

6.2 Results

Fig. 6.2 and 6.3 show the effective potentials of two polymers of different lengths confined in a slit of width H as a function of the distance between the centers of mass R_{c2c} rescaled by the radius of gyration R_g of a single polymer in the slit. One can note that the effective potentials converge to zero at $R_{c2c} \approx 3R_g$ for all systems indicating that the inter-polymer interactions vanish beyond the distance $3R_g$. Since the radius of gyration scales with the number of monomers comprising polymers as $N^{3/4}$ (see eq. (2.3.41)), the effective potential also depends on the size of the polymer along the slit. Such a size dependence of the effective potential has previously been observed for unconfined linear and ring polymers [88, 89, 91, 101].

When moving polymers towards each other ($R_{c2c} < 3R_g$), we force them to overlap, and the excluded volume interactions between the polymers in the overlapping region lead to an increase in the effective potential. The effective potential grows rapidly with the decrease of the distance between the centers of mass up to $R_{c2c} \approx 0.6R_g$. However, this tendency changes in the region $0 \leq R_{c2c} \lesssim 0.6R_g$ and the shape of the effective potential resembles a plateau with a small rise towards $R_{c2c} = 0$.

Such a change in the shape of the effective potentials can be explained by looking at the regions where the monomers are in overlap. Fig. 6.4 shows exemplary simulation snapshots of two polymers at different degrees of the centers' of mass separation.

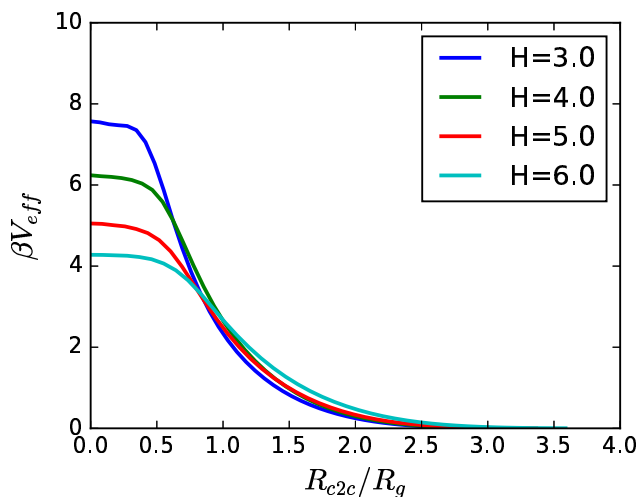


Figure 6.2: Effective potential of two linear polymers confined in a slit of width H as a function of the distance between the centers of mass R_{c2c} rescaled by the radius of gyration R_g of a single polymer under the same confinement. Each polymer is composed of $N = 50$ monomers.

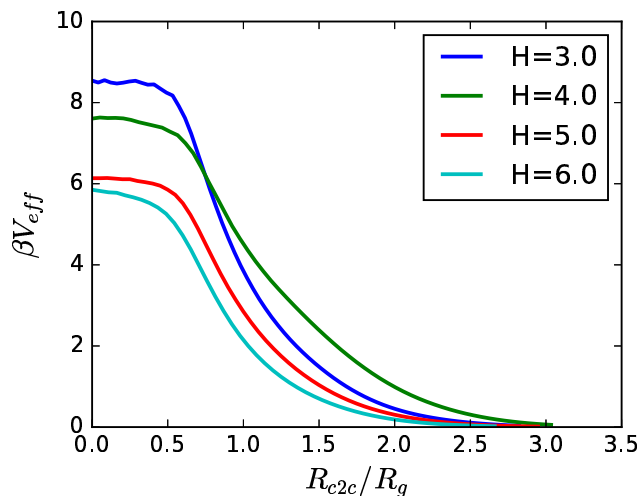


Figure 6.3: Effective potential of two linear polymers confined in a slit of width H as a function of the distance between the centers of mass R_{c2c} rescaled by the radius of gyration R_g of a single polymer under the same confinement. Each polymer is composed of $N = 100$ monomers.

Comparing the configuration of nonseparated polymers $R_{c2c} = 0$ (Fig. 6.4 (a)) and the configuration where the polymers are separated by the distance $R_{c2c} = 0.48R_g$, one can note that the total area where the monomers are in overlap is comparable in both cases and contains approximately the same number of overlapping monomer. Since the interactions of the overlapping monomers give the main contribution to the effective potential, the effective potential for the shown configurations and configurations, where the distance between the centers of mass is in between zero and approximately half of the radius of gyration, have about the same height that creates the plateau. Further increasing the distance between the centers of mass reduces the overlapping area as depicted in Fig. 6.4 (c) for $R_{c2c} = R_g$, leading to a decay of the effective potential.

A similar behavior of the effective potential with the plateau-like region at the beginning of the polymers' separation has been observed for polymers confined in a cylinder [9]. However, the size L_{eq} of polymers in a cylinder is much larger than the one in a slit, and therefore the polymers overlap at longer distances of polymers' separation. The length of the plateau in this case is comparable to the diameter $D \ll L_{eq}$ of the cylinder, that makes the plateau less pronounced over all range of the polymers' separation where the inter-polymer interactions are nonzero.

It is worth mentioning that increasing the width of the slit leads to a decrease in the height of the effective potential. This is expectable, because the compression induced by the confinement weakens for wide slits decreasing the confinement free

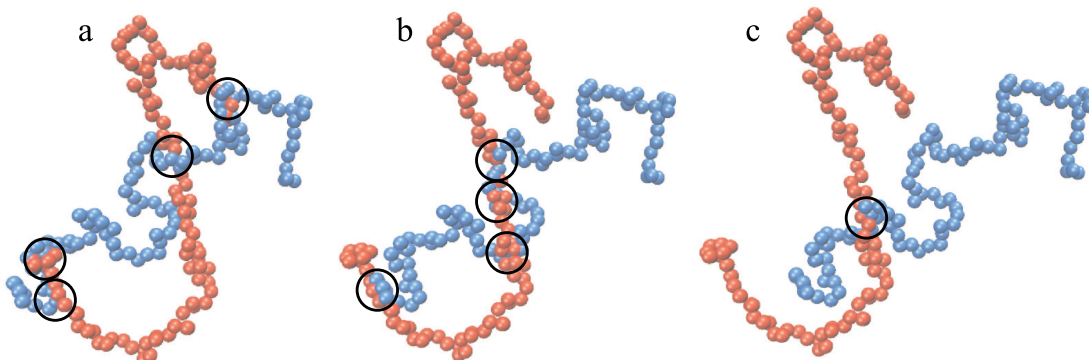


Figure 6.4: Top view on exemplary configurations of polymers composed of $N = 100$ monomers in a slit of width $H = 5.0$. (a)-(c) The same configurations of polymers, but different distances between the centers of mass R_{c2c} . (a) Polymers' centers of mass coincide. (b) The polymers are separated by the distance $R_{c2c} = 0.48R_g$. (c) The polymers are separated by the distance $R_{c2c} = R_g$. Circles mark overlapping areas.

energy, and the effective potential in the limiting case ($H \geq 3R_g$) have to converge to the one of unconfined polymer [88, 89, 101].

6.3 Conclusion

In this chapter, the effective potential of two linear self-avoiding polymers confined in a narrow slit was computed using the method of Widom insertions [77]. The obtained effective potentials, which depend on the distance between the polymers' centers of mass, have a pronounced plateau-like region at the beginning of the polymers' separation. The appearance of the plateau region, where the polymers' separation is in the range between zero and $\approx 0.6R_g$, is caused by the fact that the number of overlapping monomers stays almost constant in this range. Beyond this region the number of overlapping monomers diminishes to zero leading to the monotonic decay of the effective potential towards zero.

In summary, we gave only rough estimation of the length of the plateau, therefore, an additional study is required in order to understand how the length and the height of the plateau depend on the polymer length and the width of the slit. In future, one needs to develop a theory that allows one to estimate the free energy of a single polymer as well as two overlapping polymers in a slit-like confinement. This theory can be based either on the statistics of a self-avoiding walk or on the Flory approach with an appropriate rescaling of the lengths as it was done in the renormalized Flory approach for cylindrical confinement. Then, one can perform additional simulations for longer polymers which will be more time consuming than for the polymers considered in this chapter. Moreover, the obtained effective po-

tentials have a tendency to increase in height for longer polymers and narrower slits. We discovered that the method of Widom insertions applied to polymers confined in a slit gives accurate effective potentials with a height up to $10k_B T$, therefore, for longer polymers we would recommend to use one of the advanced sampling methods instead of Widom's insertions despite all its advantages.

Chapter 7

Summary and outlook

Overlapping polymers confined in a cylinder experience strong repulsion that drives them towards segregation. This has biological relevance to chromosome segregation in single-celled elongated bacteria such as *E. coli* because in principle, chromosomes can segregate for purely entropic reasons without any help from active mechanisms. In this thesis, we investigated entropic segregation of polymers under cylindrical confinement of infinite length where the confining cylinder is so narrow that its diameter is significantly smaller than the radius of gyration of the unconfined polymers.

We performed molecular dynamics simulations using the simulation package ESPResSo. We modeled the polymers as simple beads connected by springs. In addition to computer simulations we developed a theoretical model for calculating the free energy of the polymers depending on their degree of separation. This model is based on the splitting of territories occupied by monomers that are released from overlap and those that still overlap. By applying the renormalized Flory approach to each of the territories we showed that the force that repels the polymers is not constant during segregation as it has been found in the previous theoretical model used for studying segregation of linear polymers. In contrast to the previous model, our theoretical approach takes into account the fact that the overlap of polymers stretches them along the cylinder, allowing us to estimate the free energy more accurately and find the non-constant behavior of the force. However, we show that the force remains inversely proportional to the diameter of the cylinder, independently of whether the polymer stretching has been taken into account. Therefore, the stretching does not influence the main scaling laws of the average segregation speed $V \sim 1/ND$ and time $t_{seg} \sim N^2 D^{2-1/\nu}$, where N is the polymer length and D is the diameter of the confining cylinder, both obtained from the previous simpler model.

As we observed in simulations, an important part of the polymer segregation in a cylinder of infinite length is an induction phase, which occurs before polymers start separating. During this induction phase the perfectly symmetrical configuration of

two overlapping polymers has to be broken. This causes a delay in initiation of the segregation process.

A part of this thesis was dedicated to studying the breaking mechanism and time scales of the induction phase which has not been investigated before. We showed that during the induction phase one polymer can be spontaneously trapped between the ends of the second polymer preventing polymer segregation. In order to initiate the segregation, polymers have to arrange their ends so that each polymer has only one end released from the overlap. Only this configuration allows the polymers to start segregating. To make such an arrangement of the ends, the polymers have to overcome a free energy barrier from the fully overlapping configuration. By calculating the free energy using our approach with splitting territories, we determined that the height of this barrier scales linearly with the polymer length, making the correct arrangement a rare event. Using Kramers' theory we found that the induction time scales exponentially with the free energy barrier and, therefore, with the polymer length. We confirmed the theoretically obtained scaling of the induction time using computer simulations. With this, we conclude that the induction phase of long polymers confined in a cylinder of infinite length is much longer than actual segregation, which scales quadratically with the polymer length. Induction, therefore, dominates segregation for long polymers.

Since entropic segregation has a straightforward relevance to chromosome segregation in bacteria, we also examined if one of the important biological details, namely replication, can influence the induction phase. We studied the behavior of two initially overlapping polymers that replicate at a finite rate. It turned out that the induction phase remains pronounced independently of the replication rate: fast replication does not change the induction time distribution either qualitatively or quantitatively. At slow replication, segregation can set in during replication, however it is relatively likely that after replication one polymer is trapped between the ends of the second polymer. This immediately leads to the problem of the correct arrangement of the polymer ends during the induction phase. Moreover, we also showed that the replication does not affect the actual segregation and does not change its time scales.

It is known that chromosomes of elongated bacteria have a circular shape. In this thesis, we also studied ring polymers in order to elucidate how ring topology affects the entropic segregation and induction phase. To this end, we generalized the renormalized Flory approach to calculate the free energy of two segregating ring polymers theoretically. The generalization is based on the splitting of territories depending on the polymers' overlapping regions and the fact that a ring polymer confined in a narrow cylinder can be mimicked by two linear polymers trapped in imaginary subcylinders of reduced diameter. Using computer simulations, we proved that our territorial renormalized Flory approach gives correct estimations of the free energy of two segregating rings and, moreover, is applicable to calculations

of the free energy of many overlapping chains. This approach allowed us not only to justify that ring topology facilitates segregation, but also to find that it speeds up the segregation by a constant factor $2^{3/2}$ in comparison with linear polymers of the same length. We also show that the induction phase of ring polymers takes less time than for linear chains. Despite this, the induction time still scales exponentially with the polymer length, which we confirmed with computer simulations. Therefore, for long polymers the induction phase remains dominant over actual segregation independently of the polymer topology.

Confining two polymers in a cylinder of a finite length can change the spatial organization of polymers depending on the shape of the cylinder, which influences polymer miscibility. We investigated the relationship between the spatial organization and polymer miscibility at a relatively low monomer volume fraction $\phi = 0.076$. We varied the aspect ratio of the cylindrical axes to cover all possible shapes of the cylinder from very long and narrow cylinders to disk-like confinement. We showed that polymers confined in an elongated cylinder repel each other so strongly that they resist mixing along the cylinder despite the longitudinal compression induced by confinement, and, therefore, each of the polymers occupies half of the cylinder. When the cylinder resembles a disk, the polymers start readily mixing along the longitudinal axis of the cylinder, however, due to their self-avoidance they segregate along the radial axis of the cylinder. This behavior is consistent with the miscibility diagram that shows the degree of the polymer overlap for different cylindrical parameters. The resistance of polymers against mixing in elongated cylinders is caused by the free energy barrier that two separated polymers have to overcome in order to mix. With the help of the conventional brute force molecular dynamics simulations performed using ESPResSo and Forward Flux Sampling simulations performed using FRESHS, we computed this free energy barrier for different aspect ratios of the cylinder and polymer lengths. We found that the free energy barrier grows as the aspect ratio increases, such that the highest free energy barrier corresponds to the longest and narrowest cylinder. The free energy barrier converges to zero as soon as the aspect ratio becomes close to unity. Our theoretical predictions of the free energy barrier, obtained using the renormalized Flory approach, also confirm the trend that we observed in simulations. The obtained results have an implication for chromosome segregation in single-celled bacteria and the morphology of bacteria: the more elongated the confining geometry, the higher the free energy of overlapping chromosomes, which leads to stronger repulsion of chromosomes while they are segregating. Thus, elongated shapes facilitate segregation. However, the segregation should not be necessarily fast, but it has to be efficient in order not to disturb other ongoing processes in cells during their division. It might be that nature optimized the shape of prokaryotic bacteria exactly for this reason, leading to an environment full of bacteria of different elongated shapes.

In future, one could extend the study of the polymers confined in a cylinder of

finite length and estimate the free energy barrier that two separated polymers have to overcome at higher and lower volume fractions of monomers. Adding the values of the barriers to the miscibility diagram will make the diagram more detailed, since it will contain not only information about the spatial organization of the polymers depending on the geometrical shape of confinement, but also the free energy cost for such an organization.

Apart from cylindrical confinement, polymers can also segregate in a narrow slit for the same purely entropic reason. In this thesis, we made the first steps towards understanding entropic segregation in a slit geometry and studied how effectively the polymers repel each other in this confining geometry. To this end, using the method of Widom insertion, we computed the effective potentials of two polymers confined between two parallel plates. The plates are placed so close to each other that the distance between them is significantly smaller than the radius of gyration of the unconfined polymers. The obtained effective potentials, which depend on the distance between the polymers' centers of mass, have a pronounced plateau-like region at the beginning of the polymer separation that then decays towards zero. Zero effective potential is reached when the polymers' separation equals three times the radius of gyration of a single polymer, independently of the polymer length. We also showed that the plateau region of the effective potentials is induced by the fact that the number of overlapping monomers, which give the contribution to the effective potential, does not change at the beginning of the separation. A similar behavior of the effective potential has been previously found for polymers in a cylinder, although in the latter case, the plateau is much smaller and comparable to the diameter of the cylinder. How the plateau length depends on the polymer length and the width of the confining slit remains an open question for further investigation. Another important problem that arises from this thesis, and which is also connected to finding a scaling law for the length of the plateau, is how to calculate the effective potential theoretically. Currently there is no appropriate theory that can estimate the free energy of two overlapping polymers in a slit, which is an outstanding theoretical problem of polymer physics. This theory has to count the number of overlapping blobs accurately, which is difficult to achieve in slits, since polymers in slits lose the linear ordering observed in cylinders. In principle, one can still rely on the Flory approach, but in this case the approach requires a renormalization as was done in the renormalized Flory approach for cylindrical confinement.

Finally, I would like to conclude that this thesis clarifies some questions regarding entropic segregation of polymers under confinement, helps to systemize the study about this process and also states new questions which can inspire to future investigations in this field.

Acknowledgements

Four years of my life were given to the project presented in this thesis. Looking back you understand how much has been done during this time, which run very fast. Here I would like to thank all the people, who supported me during this period.

Firstly, I would like to express my sincere gratitude to my advisor Dr. Axel Arnold for an opportunity to work on this highly interesting project and supervising me during this four years. Without all his advice and guidance, this work would not have been possible.

I am also very grateful to Prof. Dr. Christian Holm for taking over the supervision in the last year of my work on this thesis, and for creating a nice atmosphere at the Institute for Computational Physics (ICP), where I worked on this project.

I would like to express my gratitude to Prof. Dr. Cristos Likos for an opportunity to join his group at the University of Vienna for three months. His supervision during that time and many inspiring discussions helped me to extend this project and achieve new results, which became a part of this thesis.

Many thanks go to my colleagues for having a pleasant time at ICP. During this four yeas I met so many wonderful people, who became good friends. Especially I would like to thank Dr. Rudolf Weeber and Dr. Owen Hickey for their precious support whenever I needed.

Besides, I am very thankful to my former supervisor Dr. Sofia Kantorovich, who practically opened the world of science to me, who inspired and helped to make the first steps in theoretical studying Soft Matter.

Last but not the least, I would like to thank my family and Vlad for supporting me spiritually throughout writing this thesis.

Bibliography

- [1] S. Jun and B. Mulder. Entropy-driven spatial organization of highly confined polymers: Lessons for the bacterial chromosome. *Proceedings of the National Academy of Sciences*, 103(33):12388–12393, 2006.
- [2] A. Arnold and S. Jun. Time scale of entropic segregation of flexible polymers in confinement: Implications for chromosome segregation in filamentous bacteria. *Phys. Rev. E*, 76:031901, 2007.
- [3] Y. Jung and B.-Y. Ha. Overlapping two self-avoiding polymers in a closed cylindrical pore: Implications for chromosome segregation in a bacterial cell. *Phys. Rev. E*, 82:051926, 2010.
- [4] Y. Liu and B. Chakraborty. Segregation of polymers in confined spaces. *Physical biology*, 9(6):066005, 2012.
- [5] Y. Jung, J. Kim, S. Jun, and B.-Y. Ha. Intrachain ordering and segregation of polymers under confinement. *Macromolecules*, 45(7):3256–3262, 2012.
- [6] Y. Jung, C. Jeon, J. Kim, H. Jeong, S. Jun, and B.-Y. Ha. Ring polymers as model bacterial chromosomes: confinement, chain topology, single chain statistics, and how they interact. *Soft Matter*, 8:2095–2102, 2012.
- [7] D. Račko and P. Cifra. Segregation of semiflexible macromolecules in nanochannel. *The Journal of Chemical Physics*, 138(18):184904, 2013.
- [8] J. Shin, A. G. Cherstvy, and R. Metzler. Mixing and segregation of ring polymers: spatial confinement and molecular crowding effects. *New Journal of Physics*, 16(5):053047, 2014.
- [9] J. M. Polson and L. G. Montgomery. Polymer segregation under confinement: Free energy calculations and segregation dynamics simulations. *The Journal of Chemical Physics*, 141(16):164902, 2014.
- [10] J. O. Tegenfeldt, C. Prinz, H. Cao, S. Chou, W. W. Reisner, R. Riehn, Y. M. Wang, E. C. Cox, J. C. Sturm, P. Silberzan, and R. H. Austin. The dynamics

BIBLIOGRAPHY

- of genomic-length DNA molecules in 100-nm channels. *Proceedings of the National Academy of Sciences of the United States of America*, 101(30):10979–10983, 2004.
- [11] J. O. Tegenfeldt, C. Prinz, H. Cao, R. L. Huang, R. H. Austin, S. Y. Chou, E. C. Cox, and J. C. Sturm. Micro- and nanofluidics for DNA analysis. *Analytical and Bioanalytical Chemistry*, 378(7):1678–1692, 2004.
- [12] N. A. Champbell. *Biology*. Benjamin Commings, fourth edition, 1996.
- [13] J. M. Berg, J. L. Tymoczko, and L. Stryer. *Biochemistry*. New York: Freeman, fifth edition, 2002.
- [14] D. J. Mai, C. Brockman, and C. M. Schroeder. Microfluidic systems for single DNA dynamics. *Soft Matter*, 8:10560–10572, 2012.
- [15] J. Pelletier, K. Halvorsen, B.-Y. Ha, R. Pappalardo, S. J. Sandler, C. L. Woldringh, W. P. Wong, and S. Jun. Physical manipulation of the *Escherichia coli* chromosome reveals its soft nature. *Proceedings of the National Academy of Sciences*, 109(40):E2649–E2656, 2012.
- [16] W. Reisner, K. J. Morton, R. Riehn, Y. M. Wang, Z. Yu, M. Rosen, J. C. Sturm, S. Y. Chou, E. Frey, and R. H. Austin. Statics and dynamics of single DNA molecules confined in nanochannels. *Phys. Rev. Lett.*, 94:196101, 2005.
- [17] K. Jo, M. D. Dhingra, T. Odijk, J. J. de Pablo, M. D. Graham, R. Runnheim, D. Forrest, and D. C. Schwartz. A single-molecule barcoding system using nanoslits for DNA analysis. *Proceedings of the National Academy of Sciences*, 104(8):2673–2678, 2007.
- [18] T. T. Perkins, S. R. Quake, D. E. Smith, and S. Chu. Relaxation of a single DNA molecule observed by optical microscopy. *Science*, 264:822 – 826, 1994.
- [19] M. D. Wang, H. Yin, R. Landick, J. Gelles, and S. M. Block. Stretching DNA with optical tweezers. *Biophysical Journal*, 72(3):1335 – 1346, 1997.
- [20] C. Bustamante, S. B. Smith, J. Liphardt, and D. Smith. Single-molecule studies of DNA mechanics. *Current Opinion in Structural Biology*, 10(3):279 – 285, 2000.
- [21] T. T. Perkins, D. E. Smith, R. G. Larson, and S. Chu. Stretching of a single tethered polymer in a uniform flow. *Science*, 268:83 – 87, 1995.
- [22] M. Rubinstein and R. H. Colby. *Polymer Physics*. Oxford University Press, 2003.

- [23] S. L. Levy, J. T. Mannion, J. Cheng, C. H. Reccius, and H. G. Craighead. Entropic unfolding of DNA molecules in nanofluidic channels. *Nano Letters*, 8(11):3839–3844, 2008.
- [24] M Cabodi, S. W. P. Turner, and H. G. Craighead. Entropic recoil separation of long DNA molecules. *Analytical Chemistry*, 74(20):5169–5174, 2002. PMID: 12403567.
- [25] S. W. P. Turner, M. Cabodi, and H. G. Craighead. Confinement-induced entropic recoil of single DNA molecules in a nanofluidic structure. *Phys. Rev. Lett.*, 88:128103, 2002.
- [26] C. H. Reccius, J. T. Mannion, J. D. Cross, and H. G. Craighead. Compression and free expansion of single DNA molecules in nanochannels. *Phys. Rev. Lett.*, 95:268101, 2005.
- [27] J. Han and H. G. Craighead. Separation of long DNA molecules in a micro-fabricated entropic trap array. *Science*, 288(5468):1026–1029, 2000.
- [28] K. D. Dorfman. DNA electrophoresis in microfabricated devices. *Rev. Mod. Phys.*, 82:2903–2947, 2010.
- [29] Y.-W. Yeh, A. Taloni, Y.-L. Chen, and C.-F. Chou. Entropy-driven single molecule tug-of-war of DNA at micro-nanofluidic interfaces. *Nano Letters*, 12(3):1597–1602, 2012. PMID: 22329347.
- [30] D. J. Bonthuis, C. Meyer, D. Stein, and C Dekker. Conformation and dynamics of DNA confined in slitlike nanofluidic channels. *Phys. Rev. Lett.*, 101:108303, 2008.
- [31] J. T. Mannion, C. H. Reccius, J. D. Cross, and H. G. Craighead. Conformational analysis of single dna molecules undergoing entropically induced motion in nanochannels. *Biophysical Journal*, 90:4538–4545, 2006.
- [32] D. Bates and N. Kleckner. Chromosome and replisome dynamics in *E. coli*: Loss of sister cohesion triggers global chromosome movement and mediates chromosome segregation. *Cell*, 121:899–911, 2005.
- [33] P. Wang, L. Robert, J. Pelletier, W. L. Dang, F. Taddei, A. Wright, and S. Jun. Robust growth of *Escherichia coli*. *Current Biology*, 20(12):1099 – 1103, 2010.
- [34] D. Bates, J. Epstein, E. Boye, K. Fahrner, H. Berg, and N. Kleckner. The *Escherichia coli* baby cell column: a novel cell synchronization method provides new insight into the bacterial cell cycle. *Molecular Microbiology*, 57(2):380–391, 2005.

BIBLIOGRAPHY

- [35] J. K. Fisher, A. Bourniquel, G. Witz, B. Weiner, M. Prentiss, and N. Kleckner. Four-dimensional imaging of *E.coli*: Nucleoid organization and dynamics in living cells. *Cell*, 153(4):882 – 895, 2013.
- [36] S. Taheri, S. Brown, J. T. Sauls, D. McIntosh, and S. Jun. Single-cell physiology. *Annual Review of Biophysics*, 44:123 – 142, 2015.
- [37] B. Youngren, H.J. Nielsen, S. Jun, and S. Austin. The multifork *Escherichia coli* chromosome is a self-duplicating and self-segregating thermodynamic ring polymer. *Genes & Development*, 28(1):71 – 84, 2014.
- [38] X. Wang, C. Possoz, and D. J. Sherratt. Dancing around the divisome: asymmetric chromosome segregation in *Escherichia coli*. *Genes & Development*, 19(19):2367–2377, 2005.
- [39] N. J. Kuwada, K. C. Cheveralls, B. Traxler, and P. A. Wiggins. Mapping the driving forces of chromosome structure and segregation in *Escherichia coli*. *Nucleic Acids Research*, 41(15):7370–7377, 2013.
- [40] S. Jun and A. Wright. Entropy as the driver of chromosome segregation. *Nat Rev Micro*, 8:600–607, 2010.
- [41] S. Jun, D. Thirumalai, and B.-Y. Ha. Compression and stretching of a self-avoiding chain in cylindrical nanopores. *Phys. Rev. Lett.*, 101:138101, 2008.
- [42] T. Romantsov, I Fishov, and O. Krichevsky. Internal structure and dynamics of isolated *Escherichia coli* nucleoids assessed by Fluorescence Correlation Spectroscopy. *Biophysical Journal*, 92(8):2875 – 2884, 2007.
- [43] D. Frenkel and B. Smit, editors. *Understanding Molecular Simulation. From Algorithms to Applications*. Academic Press, 2 edition, 2001.
- [44] R. Kubo. *Statistical Mechanics. An Advance Course with Problems and Solutions*. Elsevier Science Publishers, 1988.
- [45] L. D. Landau and E. M. Lifshitz. *Course of Theoretical Physics. Volume 5. Statistical Physics. Part 1*. Pergamon Press, 1980.
- [46] J. P. Hansen and I. R. McDonald. *Theory of Simple Liquids*. Academic Press, Burlington, third edition, 2006.
- [47] P.-G. de Gennes. *Scaling Concepts in Polymer Physics*. Cornell University Press, 1979.
- [48] A. Yu. Grosberg and A. R. Khokhlov. *Statistical Physics of Macromolecules*. AIP Press, 1994.

-
- [49] M. Doi. *Introduction to Polymer Physics*. Clarendon Press, Oxford, 1996.
- [50] I. Teraoka. *Polymer Solutions. An Introduction to Physical Properties*. John Wiley & Sons, Inc., New York, 2002.
- [51] J. C. Le Guillou and J. Zinn-Justin. Critical exponents for the n -vector model in three dimensions from field theory. *Phys. Rev. Lett.*, 39:95–98, 1977.
- [52] J. des Cloizeaux. Lagrangian theory for a self-avoiding random chain. *Phys. Rev. A*, 10:1665–1669, 1974.
- [53] J. des Cloizeaux. The lagrangian theory of polymer solutions at intermediate concentrations. *Journal de Physique*, 36(4):281–291, 1975.
- [54] M. Doi and S. F. Edwards. *The Theory of Polymer Dynamics*. Oxford University Press, 1986.
- [55] L. J. Fetters, N. Hadjichristidis, J. S. Lindner, and J. W. Mays. Molecular weight dependence of hydrodynamic and thermodynamic properties for well-defined linear polymers in solution. *Journal of Physical and Chemical Reference Data*, 23:619–640, 1994.
- [56] J. P. Cotton. Polymer excluded volume exponent ν : An experimental verification of the n vector model for $n = 0$. *Journal de Physique - Letters*, 41(9):231–234, 1980.
- [57] S. F. Edwards. The statistical mechanics of polymers with excluded volume. *Proceedings of the Physical Society*, 85:613–624, 1965.
- [58] M. Daoud, J. P. Cotton, B. Farnoux, G. Jannink, G. Sarma, H. Benoit, C. Duplessix, C. Picot, and P. G. de Gennes. Solutions of flexible polymers. Neutron experiments and interpretation. *Macromolecules*, 8(6):804–818, 1975.
- [59] A. Yu. Grosberg, P. G. Khalatur, and A. R. Khokhlov. Polymeric coils with excluded volume in dilute solution: The invalidity of the model of impenetrable spheres and the influence of excluded volume on the rates of diffusion-controlled intermacromolecular reactions. *Die Makromolekulare Chemie, Rapid Communications*, 3:709–713, 1982.
- [60] P. Pincus. Excluded volume effects and stretched polymer chains. *Macromolecules*, 9(3):386–388, 1976.
- [61] Y. Jung, S. Jun, and B.-Y. Ha. Self-avoiding polymer trapped inside a cylindrical pore: Flory free energy and unexpected dynamics. *Phys. Rev. E*, 79:061912, 2009.

BIBLIOGRAPHY

- [62] J. H. Van Vliet, M. C. Luyten, and G. Ten Brinke. Scaling behavior of dilute polymer solutions confined between parallel plates. *Macromolecules*, 25(14):3802–3806, 1992.
- [63] M. P. Allen and D. J. Tildesley. *Computer Simulations of Liquids*. Clarendon Press. Oxford, 1987.
- [64] L. Verlet. Computer "experiments" on classical fluids. I. Thermodynamical properties of Lennard-Jones molecules. *Phys. Rev.*, 159:98–103, 1967.
- [65] R. Kubo. The fluctuation-dissipation theorem. *Reports on Progress in Physics*, 29(1):255, 1966.
- [66] G. S. Grest and K. Kremer. Molecular dynamics simulation for polymers in the presence of a heat bath. *Phys. Rev. A*, 33:3628–3631, 1986.
- [67] J. D. Weeks, D. Chandler, and H. C. Andersen. Role of repulsive forces in determining the equilibrium structure of simple liquids. *The Journal of Chemical Physics*, 54:5237–5247, 1971.
- [68] H.J. Limbach, A. Arnold, B.A. Mann, and C. Holm. ESPResSo an extensible simulation package for research on soft matter systems. *Computer Physics Communications*, 174:704–727, 2006.
- [69] S. Arrhenius. *Z. Phys. Chem. (Leipzig)*, 4:226, 1889.
- [70] H. A. Kramers. Brownian motion in a field of force and the diffusion model of chemical reactions. *Physica*, 7(4):284–304, 1940.
- [71] P. Haggi, P. Talkner, and M. Borkovec. Reaction-rate theory: fifty years after Kramers. *Reviews of Modern Physics*, 62(2):251–342, 1990.
- [72] C. T. A. Wong and M. Muthukumar. Scaling theory of polymer translocation into confined regions. *Biophysical Journal*, 95(8):3619 – 3627, 2008.
- [73] S. Jun, J. Bechhoefer, and B.-Y. Ha. Diffusion-limited loop formation of semiflexible polymers: Kramers theory and the intertwined time scales of chain relaxation and closing. *EPL (Europhysics Letters)*, 64(3):420, 2003.
- [74] S. Jun, J. Herrick, A. Bensimon, and J. Bechhoefer. Persistence length of chromatin determines origin spacing in *Xenopus* early-embryo DNA replication. Quantitative comparisons between theory and experiment. *Cell Cycle*, 3(2):223–229, 2004.
- [75] J. Kastner. Umbrella sampling. *Wiley Interdisciplinary Reviews: Computational Molecular Science*, 1(6):932–942, 2011.

- [76] R. J. Allen, P. B. Warren, and P. R. ten Wolde. Sampling rare switching events in biochemical networks. *Phys. Rev. Lett.*, 94:018104, 2005.
- [77] B. M. Mladek and D. Frenkel. Pair interactions between complex mesoscopic particles from widom’s particle-insertion method. *Soft Matter*, 7:1450–1455, 2011.
- [78] A. Barducci, M. Bonomi, and M. Parrinello. Metadynamics. *Wiley Interdisciplinary Reviews: Computational Molecular Science*, 1(5):826–843, 2011.
- [79] J. G. Kirkwood. Statistical mechanics of fluid mixtures. *The Journal of Chemical Physics*, 3(5):300–313, 1935.
- [80] R. J. Allen, D. Frenkel, and P. R. ten Wolde. Simulating rare events in equilibrium or nonequilibrium stochastic systems. *The Journal of Chemical Physics*, 124(2):024102, 2006.
- [81] R. J. Allen, D. Frenkel, and P. R. ten Wolde. Forward flux sampling-type schemes for simulating rare events: Efficiency analysis. *The Journal of Chemical Physics*, 124(19):194111, 2006.
- [82] C. Valeriani, R. J. Allen, M. J. Morelli, D. Frenkel, and P. Rein ten Wolde. Computing stationary distributions in equilibrium and nonequilibrium systems with forward flux sampling. *The Journal of Chemical Physics*, 127(11):114109, 2007.
- [83] D. Moroni, T. S. van Erp, and P. G. Bolhuis. Simultaneous computation of free energies and kinetics of rare events. *Phys. Rev. E*, 71:056709, 2005.
- [84] K. Kratzer, J. T. Berryman, A. Taudt, J. Zeman, and A. Arnold. The flexible rare event sampling harness system (FRESHS). *Computer Physics Communications*, 185(7):1875 – 1885, 2014.
- [85] K. Kratzer, A. Arnold, and R. J. Allen. Automatic, optimized interface placement in forward flux sampling simulations. *The Journal of Chemical Physics*, 138(16), 2013.
- [86] B. Widom. Structure of interfaces from uniformity of the chemical potential. *Journal of Statistical Physics*, 19(6):563–574, 1978.
- [87] C. N. Likos. Effective interactions in soft condensed matter physics. *Physics Reports*, 348(45):267 – 439, 2001.
- [88] V. Krakoviack, J.-P. Hansen, and A. A. Louis. Influence of solvent quality on effective pair potentials between polymers in solution. *Phys. Rev. E*, 67:041801, 2003.

BIBLIOGRAPHY

- [89] A. Narros, C. N. Likos, A. J. Moreno, and B. Capone. Multi-blob coarse graining for ring polymer solutions. *Soft Matter*, 10:9601–9614, 2014.
- [90] S. Jun, A. Arnold, and B.-Y. Ha. Confined space and effective interactions of multiple self-avoiding chains. *Phys. Rev. Lett.*, 98:128303, 2007.
- [91] A. Narros, A. J. Moreno, and C. N. Likos. Influence of topology on effective potentials: coarse-graining ring polymers. *Soft Matter*, 6:2435–2441, 2010.
- [92] E. Minina and A. Arnold. Entropic segregation of ring polymers in cylindrical confinement. *Macromolecules*, 48(14):4998–5005, 2015.
- [93] F. Brochard and P. G. de Gennes. Dynamics of confined polymer chains. *The Journal of Chemical Physics*, 67(1):52–56, 1977.
- [94] A. Arnold, B. Bozorgui, D. Frenkel, B. Y. Ha, and S. Jun. Unexpected relaxation dynamics of a self-avoiding polymer in cylindrical confinement. *Journal of Chemical Physics*, 127(16):164903, 2007.
- [95] Y. Jung, C. Jeon, M. Ha, and B.-Y. Ha. Expansion dynamics of a self-avoiding polymer in a cylindrical pore. *EPL (Europhysics Letters)*, 104(6):68003, 2013.
- [96] E. Minina and A. Arnold. Induction of entropic segregation: the first step is the hardest. *Soft Matter*, 10:5836–5841, 2014.
- [97] P. Hänggi, P. Talkner, and M. Borkovec. Reaction-rate theory: fifty years after kramers. *Rev. Mod. Phys.*, 62:251–341, 1990.
- [98] A. Arnold, O. Lenz, S. Kesselheim, R. Weeber, F. Fahrenberger, D. Roehm, P. Košován, and C. Holm. ESPResSo 3.1 — Molecular Dynamics Software for Coarse-Grained Models. In M. Griebel and M. A. Schweitzer, editors, *Meshfree Methods for Partial Differential Equations VI*, volume 89 of *Lecture Notes in Computational Science and Engineering*, pages 1–23. Springer, 2013.
- [99] J. Dorier and A. Stasiak. Modelling of crowded polymers elucidate effects of double-strand breaks in topological domains of bacterial chromosomes. *Nucleic Acids Research*, 41(14):6808–6815, 2013.
- [100] C. Jeon, J. Kim, H. Jeong, Y. Jung, and B.-Y. Ha. Chromosome-like organization of an asymmetrical ring polymer confined in a cylindrical space. *Soft Matter*, 11:8179–8193, 2015.
- [101] P. G. Bolhuis, A. A. Louis, J. P. Hansen, and E. J. Meijer. Accurate effective pair potentials for polymer solutions. *The Journal of Chemical Physics*, 114(9), 2001.